Simulation of Plasma Electrolytic Oxidation (PEO) of AM50 Mg Alloys and its Experimental Validation

Dissertation

zur Erlangung des akademischen Grades

Doktor der Ingenieurwissenschaften

(Dr.-Ing.)

der Technischen Fakultät

der Christian-Albrechts-Universität zu Kiel

Xun Ma

aus

Henan, VR China

Kiel 2018

Gutachtern der Dissertation

1. Gutachter: Prof. Dr. Mikhail Zheludkevich

2. Gutachter: Prof. Dr. rer. nat. Marcus Stiemer

3. Gutachter: Prof. Dr.-Ing. Eckhard Quandt

4. Gutachter: Prof. Dr.-Ing. Jeffrey McCord

Vorsitzender des Promotionsausschusses:

Prof. Dr.-Ing. Eckhard Quandt

Tag der mündlichen Prüfung:

25th June 2018

Erklärung

Hiermit erkläre ich, dass die beigefügte Dissertation, abgesehen von der Beratung durch die Betreuer, nach Inhalt und Form meine eigene Arbeit ist.

Die Arbeit, ganz oder zum Teil, wurde nie schon einer anderen Stelle im Rahmen eines Prüfungsverfahrens vorgelegt und ist abgesehen, von den im Anhang angegebenen Veröffentlichungen, nicht anderweitig zur Veröffentlichung vorgelegt worden.

Außerdem ist die Arbeit unter Einhaltung der Regeln guter wissenschaftlicher Praxis der Deutschen Forschungsgemeinschaft entstanden.

Geesthacht, den 22.05.2018

Abstract

The PEO process is a useful surface technology to improve wear performance and corrosion resistance on light metals such as Mg, Al and Ti and their alloys. It has been studied for several decades, but up to now, its mechanism is still not fully understood. Many models and assumptions are proposed in the literature trying to explain the phenomena happening during the PEO process and to explain its mechanism. However, most of them are restricted to phenomenological and empirical approaches. In order to improve the understanding of PEO process and get better process design for industrial application, it is worth studying numerical approaches of the PEO process.

This thesis provides a modeling and simulation approach to study the PEO process on Mg alloy AM50 under constant voltage mode. The mechanism of the PEO process includes the growth of the coating and the evolution of the discharges, which have been discussed based on the current understanding and assumptions of the PEO process. A numerical model has been built to describe the PEO process using Finite Element Method in COMSOL. Experiments are performed to provide data input for the modeling and simulation, and also to validate the correctness and usefulness of the modeling. From comparison, the simulation result of coating thickness is in good agreement with the experimental result. The simulation result of the pores generated by the discharges shows a similar tendency with the experimental result but the values are not consistent with each other. In the meantime, the simulation can also reveal the changes of the ions in the electrolyte with time. The application of the model was verified by studies investigating the influences of different voltage, a complex substrate geometry and the electrode distance on the formation of PEO coatings. After modifying the model according to the experimental conditions, the approach of the model can predict the coating thickness close to the experimental results and explain the effects of the main process parameters on the coating growth reasonably. The substrate geometry and the electrode distance are proved to be important factors which can affect the PEO coating growth by changing the current distribution and concentration of ions in the electrolyte near the surface of the substrate. Therefore, the methodology provided by the numerical model has been demonstrated to be a useful tool for predicting the coating thickness and explaining the effects of different parameters on Mg alloy under constant voltage mode.

Zusammenfassung

Die plasmaelektrolytischen Oxidation (PEO) ist eine Oberflächentechnologie zur Verbesserung der Verschleißfestigkeit und Korrosionsbeständigkeit von Leichtmetallen wie Mg, Al und Ti und deren Legierungen. Der Prozess wird seit mehreren Jahrzehnten untersucht, aber bis jetzt ist sein Mechanismus noch nicht vollständig verstanden. In der Literatur werden viele Modelle und Annahmen vorgeschlagen, die versuchen die Phänomene während des PEO-Prozesses und seinen Mechanismus zu erklären. Die meisten sind jedoch auf phänomenologische und empirische Ansätze beschränkt. Um das Verständnis des PEO-Prozesses zu verbessern und ein optimiertes Prozessdesign für industrielle Anwendungen zu erhalten, sollten numerische Ansätze untersucht werden, die den Prozess einfach beschreiben.

Die vorliegende Arbeit stellt eine Methodik zur Modellierung und Simulation zur Verfügung, um den PEO-Prozess für die Mg-Legierung AM50 im Konstantspannungsmodus zu untersuchen. Der Mechanismus des PEO-Prozesses umfasst das Wachstum der Beschichtung und die Entwicklung der Entladungen, die basierend auf dem aktuellen Verständnis und einiger Annahmen bezüglich des PEO-Prozesses diskutiert werden. Ein numerisches Modell wurde dazu erstellt, das den PEO-Prozess unter Verwendung der Finite-Elemente-Methode in COMSOL beschreibt. Experimente wurden durchgeführt, um Daten für die Modellierung und Simulation zu generieren und um die Richtigkeit und Nützlichkeit der Modellierung zu überprüfen. Der Vergleich zeigt, dass die Simulationsergebnisse bereits nahe bei den experimentellen Ergebnissen liegen. Das Simulationsergebnis der Schichtdicke stimmt gut mit dem Versuchsergebnis überein. Das Simulationsergebnis der durch die Entladungen erzeugten Poren zeigt eine ähnliche Tendenz mit dem Versuchsergebnis, aber die Werte stimmen nicht überein. Zusätzlich kann die Simulation auch die zeitlichen Veränderungen der Ionen im Elektrolyten aufzeigen. Die Anwendbarkeit des Modells wurde durch Untersuchungen der Einflüsse unterschiedlicher Spannung, einer komplexen Substratgeometrie und des Elektrodenabstandes auf die Schichtbildung verifiziert. Nach verbesserter Anpassung des Modells an die experimentellen Bedingungen kann das Model die Schichtdicke nahe an den experimentellen Ergebnissen vorhersagen und die Auswirkungen der Hauptprozessparameter auf das Schichtwachstum vernünftig vorhersagen. Die Substratgeometrie und der Elektrodenabstand erweisen sich als die wichtigen Faktoren, die das Schichtwachstum beeinflussen können, indem sie die Stromverteilung und Konzentration von Ionen im Elektrolyten nahe der Oberfläche des Substrats verändern. Somit wurde gezeigt, dass die Methode, die durch das numerische Modell bereitgestellt wird, ein nützliches Werkzeug zur

Vorhersage der Schichtdicke und zum Einfluß verschiedener Parameter bei der PEO-Behandlung im Konstantspannungsmodus ist.

Table of Contents

1. Introduction

Light metals such as aluminum, magnesium and titanium and their alloys are playing an important role in various machinery and transportation systems due to their attractive low specific weight. It is important to reduce weight and friction loss, and to increase efficiency so as to overcome the growing demands for better fuel mileage, and for enhanced environmental protection in the modern world [1]. Nevertheless, industrial application is not expanding as well as expected because the application of these light metals and alloys is limited by some shortcomings such as poor tribology and corrosion resistance. The considerable solution to make further advancements in the strength of the basic materials and alloys is the effective use of surface modification technologies.

Magnesium being the lightest engineering material of all metals remains a potential candidate material for such applications. There has been a surge, in the recent years, in the development of a variety of magnesium alloys that can exhibit high strength, good castability, good ductility and high dimensional stability [2-4]. Nevertheless, magnesium and its alloys are prone to corrosion, by virtue of magnesium being one of the most reactive metallic elements, and the oxide it forms, unlike aluminum and titanium, is less protective to the substrate. Additional protection of magnesium from corrosion is therefore imperative. Various types of protective coatings, namely organic, conversion, ion implantation and plasma electrolytic oxidation (PEO) are suggested for preventing corrosion of magnesium and its alloys [5]. Among those, PEO coatings offer several advantages over other coatings [6].

Plasma Electrolytic Oxidation (PEO) is an anodization process applied to fabricate ceramic-like coatings on many lightweight metals such as aluminum, magnesium, titanium and their alloys [7-9]. It is a surface treatment technology developed based on the conventional anodising process. It differs from conventional anodizing with respect to its high operating voltages which cause dielectric breakdown of the passive film formed on the component surface [10]. The PEO process is prominent for its ability to provide high quality coatings with enhanced corrosion protection, wear resistance, biomimetic and thermal barrier properties and good adhesion to the substrate in a relatively short processing time [11]. PEO is also a hybrid of conventional electrolysis and atmospheric plasma process. Compared to vacuum based plasma-assisted coating processes, the PEO process is preferred for its capability to provide non-line-

of-sight treatment and an atmospheric pressure processing environment [12]. However, PEO is a complex process which includes chemical, electrochemical, and plasma-chemical aspects influencing heat, mass and charge transfers [13]. It is necessary to understand the characteristic, associated phenomena and mechanisms of PEO coating formation well enough to attain adequate means of process control and improve coating quality.

1.1 PEO history

Plasma electrolytic oxidation has been a field of research for many years. Within the PEO history, the discharge phenomenon associated with electrolysis was first discovered by Sluginov [14], who looked into the behavior of metal electrodes in aqueous electrolytes under high voltages in the 1880s. Then a more detailed research in this topic was carried on in the 1930s by Günterschulze and Betz [15]. However, the first practical benefits of the spark discharge were exploited only in the 1960s, when McNiell and Nordbloom used a spark discharge method to deposit cadmiun niobate onto a cadmium anode in an niobate electrolyte [16,17]. During the 1970s, Makov et al. [18] used an arc discharge to deposit anodic oxide coatings on aluminum, and then improved the technique by increasing the voltage to achieve enough energy for producing plasma channels in the initial passive layer. He termed the spark discharge anodising as 'Micro-arc oxidation'. From 1980s, more academics studied the possibilities of utilising surface discharges in oxide deposition onto various metals in more detail in Russia and Germany [19,20], and early industrial applications were introduced [21,22]. Later in the USA and China, researchers have also become involved in this subject around the 1990s [23-26]. In 1999, Yerokhin et al. presented a review of electrolytic plasma processing as an emerging surface engineering technology [27], including various plasma electrolytic deposition methods. Owing to a lack of understanding of the process phenomenology, different names were used in many studies to describe this technique: ‘micro-plasma oxidation’, ‘anode spark electrolysis’, ‘plasma electrolytic anode treatment’. But the most commonly used term is PEO. From then on, increasing attention has been paid to the continued refinement of PEO coating properties. Thus, improved and composite PEO coatings were developed for more diverse use. Currently, developments are being made in power supplies, post-treatment and processing of a wide range of lightweight alloys [28].

1.2 PEO treatment

1.2.1 PEO treatment system

The typical treatment unit for PEO processing consists of a high voltage power supply unit and an electrolyser. The electrolyser is usually composed of an electrolytic bath which is normally water-cooled, a working electrode (anode) consisting of the electrically connected alloy component to be treated, and a counter-electrode (cathode) which is usually made of stainless steel. Aqueous solutions of salts, acids or alkali with low concentration are used in most cases as the electrolyte. The application of electrical potential is significantly greater as compared to the conventional electrolysis and leads to formation of a continuous gas envelope around either the cathode or the anode accompanied by a luminous discharge [29]. Coatings can be formed under DC, AC or bipolar electrical regimes. In modern PEO technology, AC, pulsed DC and bipolar electrical regimes offer better control over plasma chemical processes compared to DC regimes, reducing adverse effects associated with the discharge under DC conditions and producing more uniform and less porous coatings [30]. Since the investment costs of the equipment are relatively low and the electrolytes are without any pollutant compounds [31,32], PEO is considered to be one of the most cost-effective and environmentally friendly ways to provide enhanced corrosion protection, wear resistance, biomimetic and thermal barrier properties for light metals [10]. The basic layout and the electrode reactions of a typical PEO system is shown in Fig.1.1.

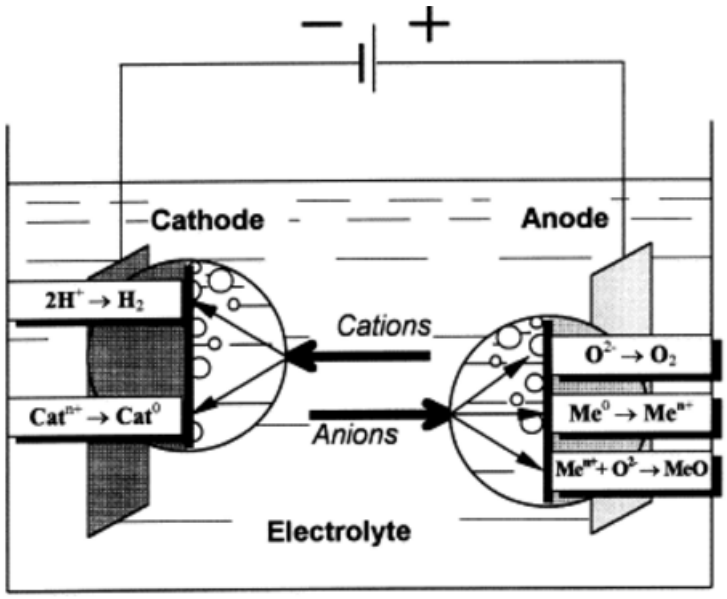

Fig.1.1 Basic layout and electrode reactions of a typical PEO system (with permission from Elsevier [27]).

The electrolysis of aqueous solutions in PEO exhibits several electrode processes. Common anode processes include oxygen evolution (Eq. 1.1) and metal oxidation (Eq. 1.2). Depending on electrolyte chemical activity, the latter could result in either surface dissolution or formation of an anodic oxide film (Eq. 1.3). Hydrogen evolution (Eq. 1.4) and/or cation reduction (Eq. 1.5) occur on the cathode surface:

$$2H_2O - 4e^- \rightarrow O_2\uparrow + 4H^+ \quad (1.1)$$

$$Me - ne^- \rightarrow Me^{n+} \quad (1.2)$$

$$xMe^{n+} + 3/2xnH_2O \rightarrow Me_xO_n\downarrow + xnH^+ \quad (1.3)$$

$$2H^+ + 2e^- \rightarrow H_2\uparrow \quad (1.4)$$

$$Cat^{n+} + ne^- \rightarrow Cat^0\downarrow. \quad (1.5)$$

1.2.2 Study of PEO process

Although PEO has been in focus of research for many years, the descriptive phenomenology of the PEO process has not changed much since 1991 [33] to recent publications. All the independent studies reveal a common observation that PEO is a technology, which requires a high voltage that can maintain the dielectric breakdown of the growing oxide film on the surface of a metal anode, and there is significant deviation from normal Faradaic electrolytic regime [34] for the calculation of gas evolution. The process is known to be complex due to the involvement of anodic oxidation, dielectric breakdown, gas evolution, cathodic breakdown and thermo-chemical driven plasma expansion and its underlying mechanisms are still not fully understood. It is important to study the formation mechanism of PEO coating aiming at understanding the procedure and optimizing the experimental conditions for obtaining the best properties. The complexity of the PEO process requires different techniques and methods to study the PEO coating growth behavior and the discharge phenomena occurring during the process. The comprehensive methods employed by various researchers to study the coating formation mechanism are schematically categorized in Fig.1.2.

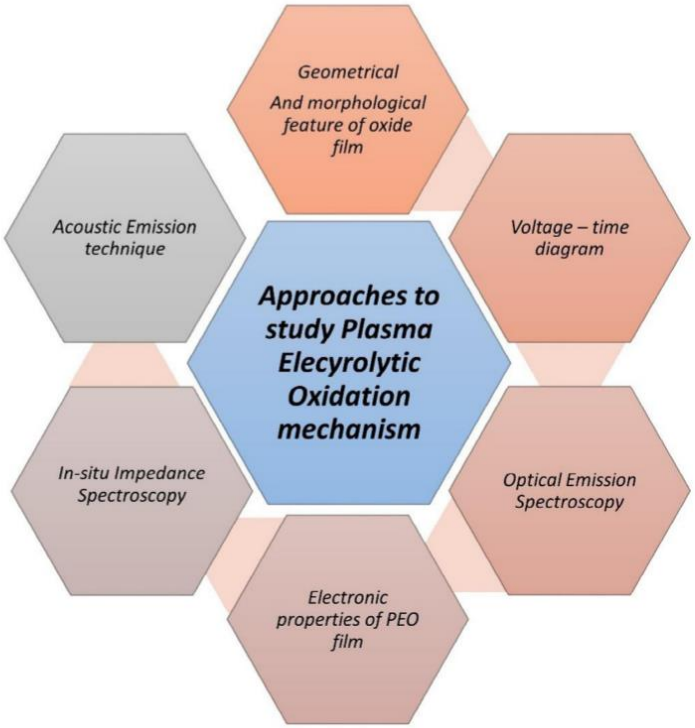

Fig.1.2 Schematic of different approaches to study plasma electrolytic oxidation mechanism (with permission from Ref. [35]).

The voltage–time response of the PEO process under constant current mode in electrochemical cells can provide readily measurable and useful information about the different stages occurring during PEO [36], as seen in Fig.1.3. Generally, a PEO process in constant current mode can be divided as four stages distinguished by the voltage–time response and their corresponding discharge characteristics. Real-time imaging techniques and optical emission spectroscopy (OES) have been utilized [37,38] to study the micro-discharge behavior during PEO treatment of various substrate materials. The real-time imaging techniques can provide information regarding duration, number and spatial distribution of discharges. Spectrum analyses may be used to gain information about temperature, density and chemical composition of plasma [14,35].

When the supplied voltage is applied, the early stage involves the rapid electrochemical formation of an initial insulating oxide film, accompanied by a rapid rise of the cell potential till the breakdown potential is obtained [38]. During this period, no sign of discharges is obtained. Then the PEO steps into the second stage when breakdown voltage is exceeded, where numerous sparks move rapidly over the whole sample surface area. The OES signal of the substrate element has a significant increase in the intensity indicating the start of the

breakdown of the oxide layer, the increase of temperature and subsequent local melting of the substrate metal in the places of discharges [14]. In the meantime, the rate of the voltage change decreases. The third stage is characterized by larger but slower moving discharges and the growing oxide layer. In stage four, less frequent discharges appear as relatively large and long lasting sparks due to the thicker coating causing more difficulty in the initiation of such discharges [36].

The phenomenon and mechanism happening in each stage during PEO and the resulting effects on the oxide layer growth behavior are different. Applied process parameters can change the duration and ratio of these stages which in turn could result in coatings with different morphology, microstructure and phase composition [39].

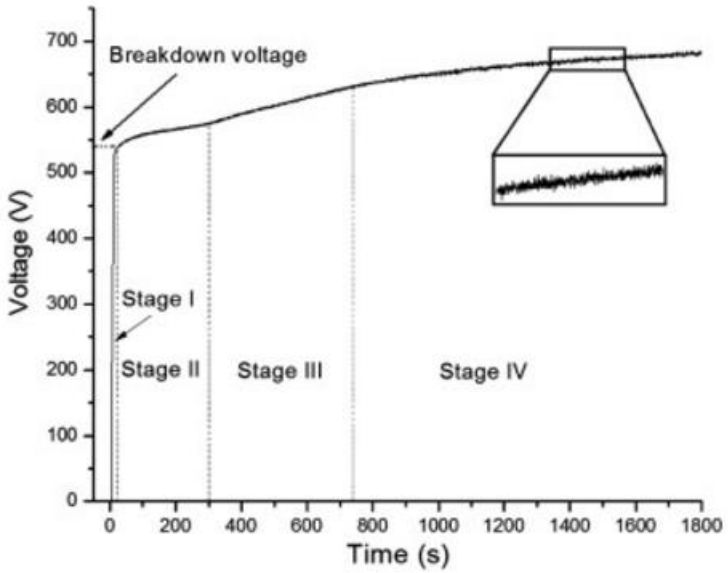

Fig. 1.3 A typical voltage –time response of a PEO coated 6061 Al alloy sample (S12–25) showing the four different stages occurring during PEO (with permission from Elsevier [36])

Side view pictures reflecting the discharging phenomena of aluminum alloy samples at different time of the PEO process [37] are shown in Fig. 1.4. The number of discharges decreases but the size of the discharges increases with time. The numerous discharges in Fig. 1.4(a) correspond to the second stage of the PEO process. The larger discharges in Fig.1.4(b) with less number indicate the third stage and the final discharges appear as relatively large stationary sparks in Fig. 1.4(c), imply the fourth stage of the PEO process.

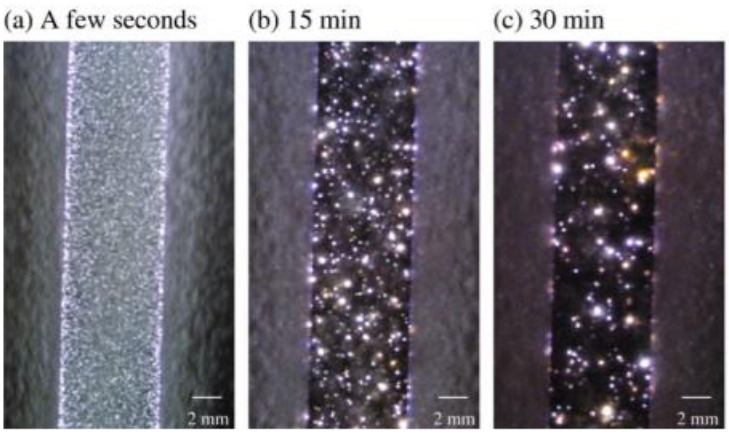

Fig. 1.4 Side view pictures of aluminium alloy samples at different time of the PEO process (with permission from Elsevier [37])

Acoustic emission technique is used to record elastic waves (between 20 kHz and 1 MHz) passing through a substance with local micro-displacements. It is employed to study physical phenomena which take place on the electrode surface during PEO process [40,41]. The acoustic energy can be tracked by AE technique to study the different stages during the PEO process as the voltage-time response. Fig. 1.5 shows the voltage and acoustic energy change during PEO process. The curves may be divided into four steps. Within the first step, voltage and acoustic energy augment linearly up to a constant value. Acoustic energy and domain are small. Then, they remain constant for 3 min at the second stage. The acoustic signals are in resonance form. Domain and energy of signals are higher than the first stage. Acoustic energy can be attributed to plasma anodizing. In the third stage, voltage and acoustic energy increase by a new level with some fluctuations. Size and energy of sparks increase in this stage and acoustic signals have higher domain and energy compared to the second stage. The acoustic energy originate from the sparking energy in this stage. At the fourth stage, the PEO process stops and voltage becomes zero. Whereas, acoustic does not reach zero but decreases. Energy and domain of signals are higher than the first stage. It is believed that signals in the fourth stage are due to release of hydrogen bubbles from surface of the oxide film [42].

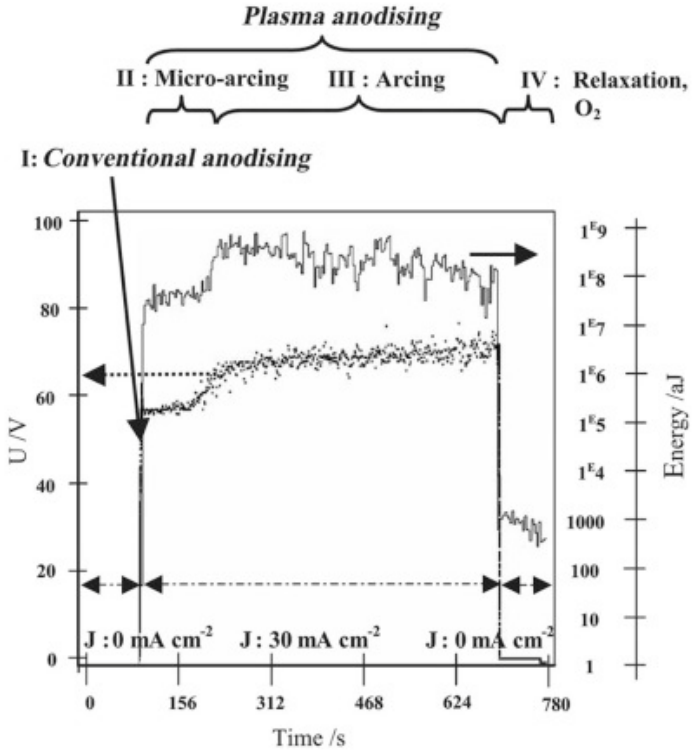

Fig. 1.5 Voltage and acoustic energy transients during PEO. (with permission from Elsevier [42])

The plasma temperature during the PEO process can be analyzed from the spectrum obtained from OES. Investigated by Dunleavy et al. [43], it is reported that plasma emitted spectrum consisted of two separate plasma regions: a central core with high temperature (16000 to 35000 K) and high electron density (5×10^{17} electron·cm^{-2}) and a marginal area which probably extends to near the electrolyte (with lower temperature and less electrons). Hussein et al. [44] managed to record temperature variations and the average temperature of the plasmas. The temperature fluctuates with time and ranges from 4000 K to 6000 K. The up and downs of plasma temperature during the PEO process may be attributed to different types of discharges happening at different stages of the process. According to Hussain et al. [14], three types of discharge may occur which are designated as type A, type B and type C. Type B discharges occur through the oxide layer due to the dielectric breakdown in a strong electric field and represent plasma reactions in substrate/coating interface. Type B discharges may lead to formation of a porous coating and harshly affect microstructure and morphology of coatings. Schematic diagram of the discharge model showing the influence of B-type discharges on surface morphology and on the cross section of the oxide coating are shown in Fig.1.6. Type A is associated with rather fine pores near the surface while type C pores are related to the

discharges in micro pores under the relatively deep surface. During the PEO processes the A, B and C types of discharge can play different roles at different times. At stage II, the mild B type of discharges are dominant since the coating thickness is still thin; the discharge initiated from the substrate/coating interface is not very strong. In stages III and IV, the probabilities of A and C type discharges are higher than that of the type B discharge, although the intensity of the B type discharge is higher. The discharge behavior within the PEO coating and on the coating surface was responsible for coating surface morphologies.

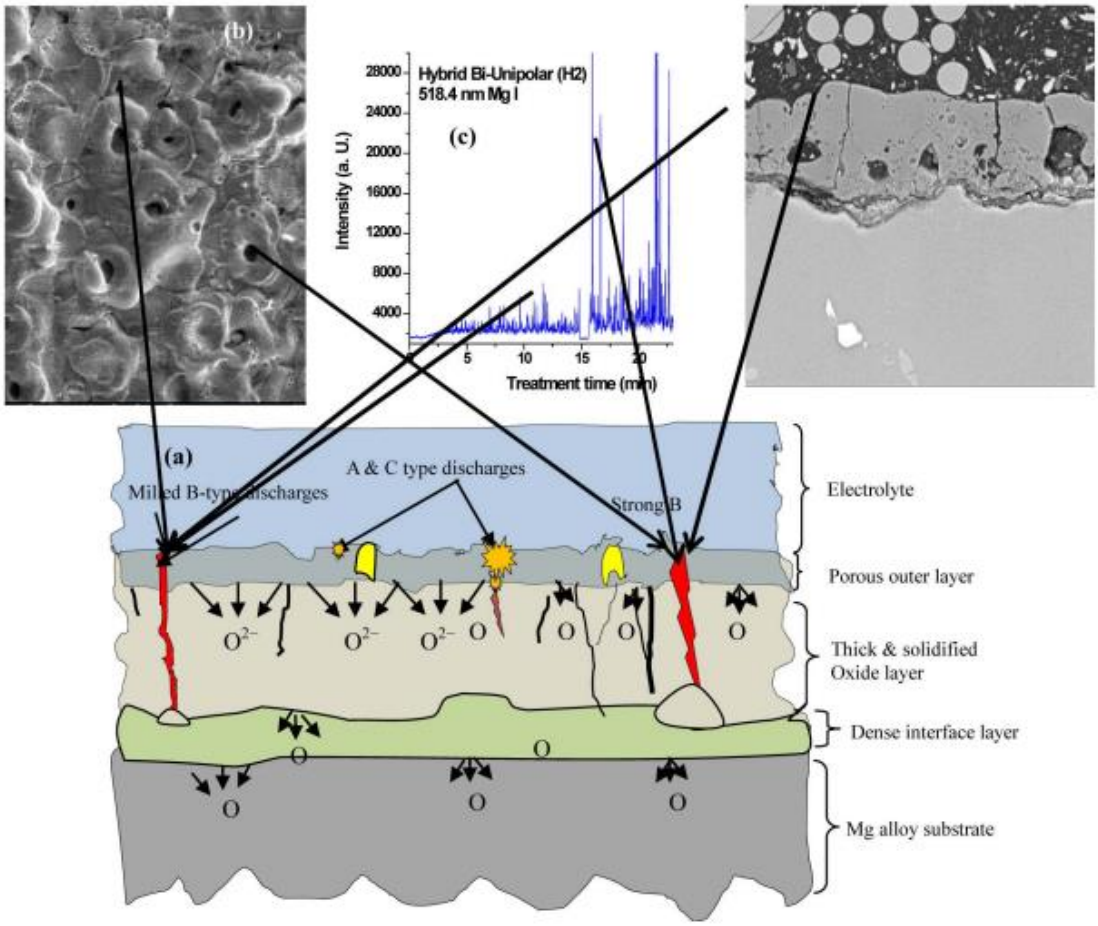

Fig. 1.6 Schematic diagram of the discharge model showing the influence of B-type discharges on surface morphology and on the cross section of the oxide coating. (with permission from Ref. [45]).

During PEO process, it is believed that electrochemical and plasma chemical reactions as well as oxygen thermal diffusion occur simultaneously around the plasma discharges [35]. For magnesium alloys, PEO is normally performed in silicate, phosphate and/or aluminate-containing alkaline electrolytes. The anode dissolution reaction in PEO processes occurs under a strong electric field producing magnesium ions:

$$Mg \rightarrow Mg^{2+} + 2e^{-} \quad (1.6)$$

Then due to outward diffusion of magnesium ions and inward diffusion of anions such as SiO_3^{2-}, OH^- and F^- in different electrolytes under high potentials, formation of oxide films on magnesium would occur once concentrations of these ions in electrode/electrolyte interface reach a critical value. The high input energies processed by the discharges cause fusion of considerable parts of the oxide film and substrate. Finally, molten substrates flow out toward the surface and form large ceramic particles while they reach the cold electrolyte. The phases formed in the coatings depend on the substrate and the species in the electrolyte. According to the following equations, the common phases Mg_2SiO_4, $MgSiO_3$, MgF_2, $Mg_3(PO_4)_2$, $Mg(OH)_2$ and MgO in the PEO coatings on magnesium alloys based on different electrolytes are produced [35]:

$$2Mg^{2+} + SiO_3^{2-} + OH^- \rightarrow Mg_2SiO_4 + H_2O \quad (1.7)$$

$$Mg^{2+} + SiO_3^{2-} \rightarrow MgSiO_3 \quad (1.8)$$

$$Mg + 2F^- \rightarrow MgF_2 \quad (1.9)$$

$$3Mg^{2+} + 2PO_4^{3-} \rightarrow Mg_3(PO_4)_2 \quad (1.10)$$

$$Mg^{2+} + 2OH^- \rightarrow Mg(OH)_2 \quad (1.11)$$

$$Mg(OH)_2 \rightarrow MgO + H_2O \quad (1.12)$$

The PEO coatings composed of different phases show an identical microstructure of porous surface morphology and a two/three-layer cross section. The typical morphologies of the cross-section and the free surface of a PEO coating are presented in Fig.1.7(a) and (b). Two distinct features can be seen from the surface morphology: micro-pores and the oxide ceramics. The micropores are considered to be the result of the plasma discharge channels and the ceramics are formed due to the sintered deposits on the coating surface caused by the electrochemical and plasma reactions between the substrate and the electrolyte. Depending on the process parameters, the pore diameter usually ranges from 0.5 μm to 50 μm [35]. The amount of pores is a function of discharge density as well as process time. Sometimes, there are cracks in the coating resulting from the residual stress between the ceramics. The cross-sectional morphology of the PEO coating is usually considered to have a two/three -layer structure with a characteristic thin barrier layer at the substrate/coating interface and a porous, thick outer

layer, and sometimes an intermediate dense layer [46] between the former two layers. The schematics of the different layers of PEO coating is shown in Fig.1.7(c). The barrier layer is normally compact and considered to provide resistance to corrosion. The outer layer is porous and constitutes most of the coating thickness. It is also reported that pore bands [47] can be formed between the inner layer and the outer layer of PEO coating on magnesium alloy using DC mode. Fig. 1.8 shows the SEM images of surface morphology, its corresponding cross section and the schematic representation of the cross section for a PEO coating formed on AM50 magnesium alloy under DC mode.

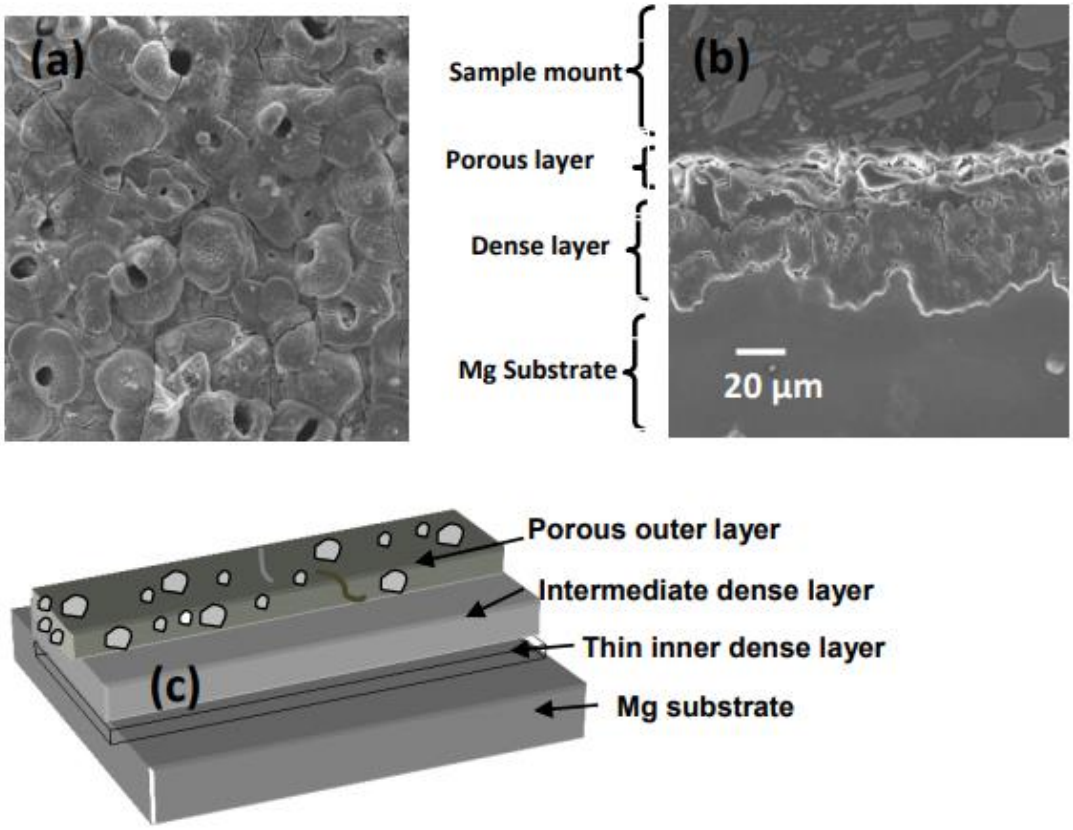

Fig. 1.7 The morphologies of the surface (a) and the cross-section (b) of a PEO coating formed on AM50 magnesium alloy and the schematic (c) of layer structure (with permission from Ref. [46]) .

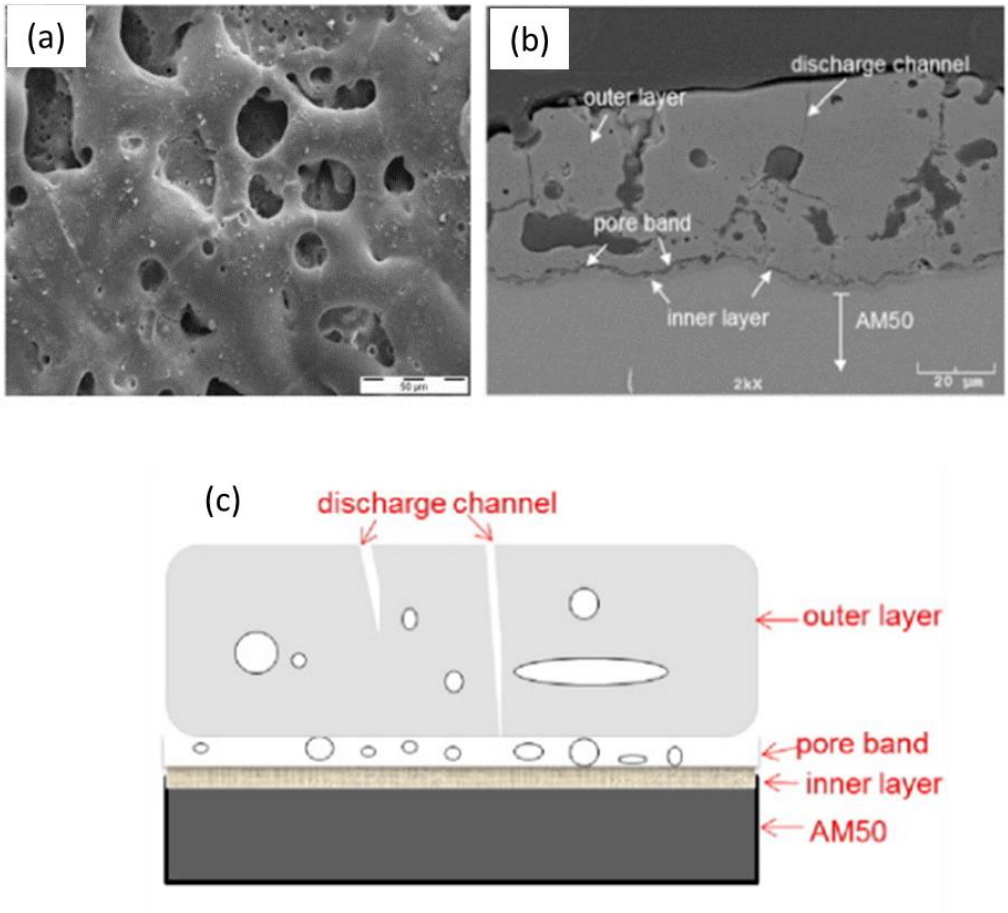

Fig. 1.8 The morphologies of the surface (a) and the cross-section (b) of a PEO coating formed on AM50 magnesium alloy under DC mode and the schematic (c) of the cross section (with permission from Ref. [47]) .

It is a common observation in PEO treatments that the total thickness of PEO coatings increases linearly with increasing treatment time under constant current mode, as can be seen in Fig. 1.9. In the PEO process, the observed linear deposition kinetics can be simply related to Faraday's law of electrolysis [39]. The observation that the coating thickness increases with the rising of the current density, exhibiting a linear behavior as a function of current density (Fig. 1.10) [48], also proves the application of Faraday's law of electrolysis in explaining the ceramic coating growth.

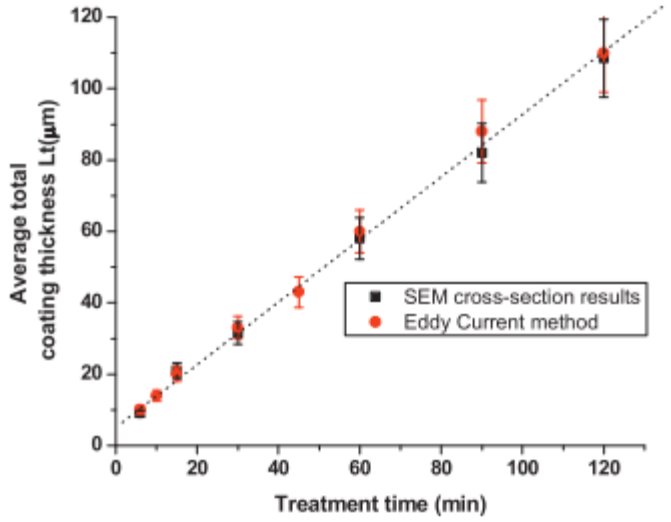

Fig. 1.9 Average coating thickness variation with PEO processing time (with permission from Ref. [44])

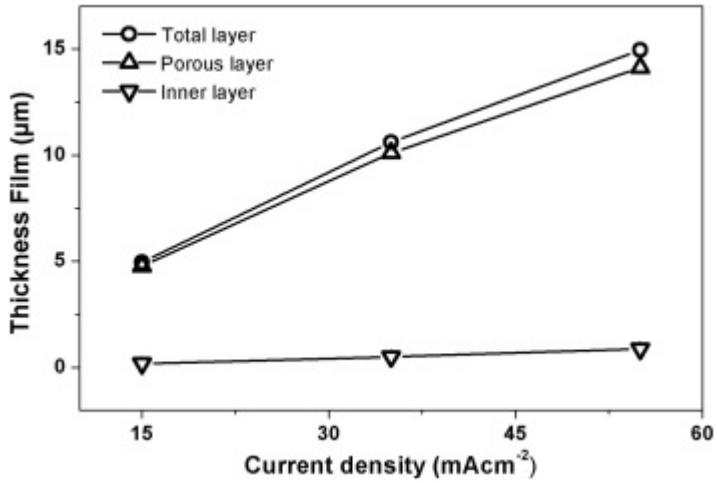

Fig. 1.10 Variation of the coating thickness for different current density values evaluated during anodizing of Ti at galvanostatic mode (with permission from Ref. [48]).

However, a remarkable characteristic of the PEO phenomenon is the strong deviation of the chemical yield at the anode from that expected on the basis of Faraday's law for the gas evolution. Large deviation has been noted at Pt anode with a voltage of 440 V during PEO process in aqueous electrolyte of K_2SO_4 in Fig. 1.11, which liberate gas with volumes two or three times the Faraday law value [34]. Because the mechanism includes not only the break up of two water molecules by normal electrolytic charge transfer to produce one O_2, but also the

break up of several liquid water molecules into H and OH radicals by ionization and activation of $H_2O_{gas}^+$ ion with sufficient energies, which will lead to formation of extra oxygen [34].

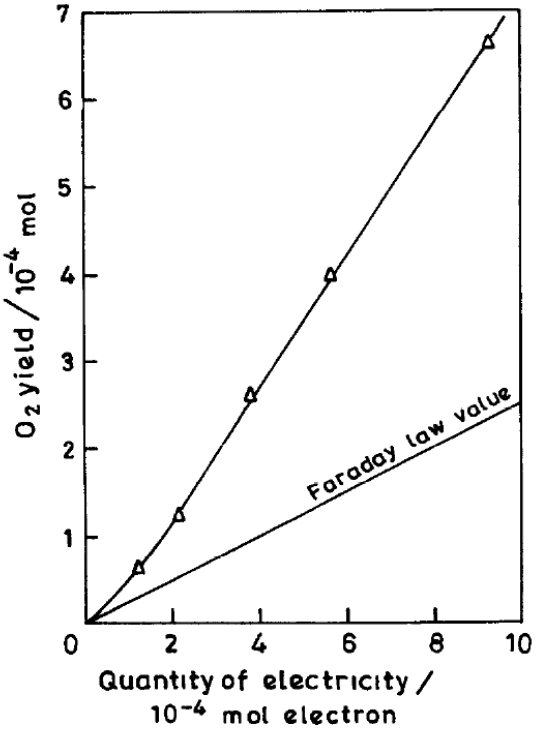

Fig. 1.11 Variation of O_2 yield with quantity of electricity during anodic PEO process under 420 V in 0.05 M K_2SO_4 (with permission from Ref. [34]).

1.3 Features of PEO processing

Ceramic coatings produced by PEO treatment offer several advantages that are of particular interest for researchers and industry including [7]:

a) PEO processing exhibits advantages of high throwing power, environmentally-friendly electrolytes, little or no requirement for pre-treatment [49]];
b) the technological procedure of PEO treatment is easy to operate as the process is carried out under atmospheric pressure;
c) PEO coatings are formed directly by oxidation of the metal and therefore are bound tightly with the substrate without any debonding [50,51];
d) PEO process is capable of non-line-of-sight treatment, which means one can form coatings on multiple sides of samples or even on substrates with complex geometry;
e) PEO treatment provides high coating growth rates and the typical treatment times are less than 60 minutes. The thickness of the coating can easily achieve 50–100 μm, with an average growth rate of 1–5 μm min^{-1} [30];

f) The ceramic coatings produced by PEO treatment are porous. By selecting proper treatment parameters, such as composition of electrolyte and treatment regime, the porosity and pores size can be controlled;

g) PEO treatment provides excellent coating properties, including high surface hardness, corrosion and wear resistance.

The porosity of the PEO coating can be either beneficial or detrimental according to different applications. The efficiency of PEO ceramic coatings to improve corrosion resistance has been investigated in many studies. In some cases, corrosion current densities of PEO coated alloys were reported to be 100 times or more lower than uncoated ones [52-55]. The main factors that influence the quality of the formed PEO coating and thus the corrosion resistance are the processing parameters, such as the applied potential, the applied current density, the reaction time, the substrate properties, electrode geometry, nature and additives of the electrolyte [41], which can be seen in Fig. 1.12. The porosity affect the corrosion resistance of the PEO coating greatly. Post-treatment to seal the pores is an effect way to improve its corrosion resistance. On the other hand, this property can also be desirable, e.g. in biomaterial applications of PEO coated titanium and magnesium, as a pre-treatment for organic based coatings [56].

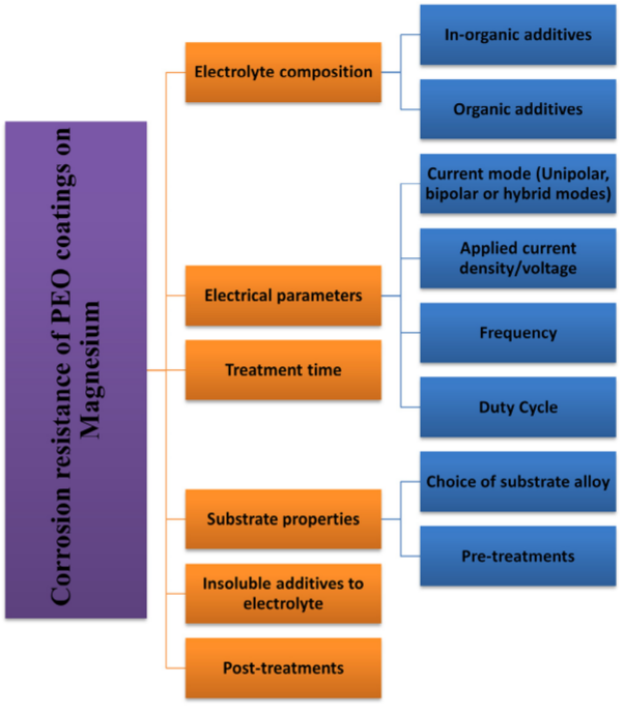

Fig. 1.12 Effective parameters in corrosion resistance of PEO coatings (with permission from Ref. [35]).

Besides, the disadvantages of PEO coatings are their brittleness and their electric isolation, which makes the method inappropriate for further processing via electric deposition [56].

1.4 PEO application

Due to the characteristics of the PEO process and the resulting coatings such as economic efficiency, ecological friendliness, corrosion resistance, high hardness, good wear resistance, and excellent bonding strength with the substrate, the PEO treatment method is likely to be more widely applied. PEO coated products and related technologies are now developed in several companies and countries e.g. Keronite in UK, Tagnite and CeraFuse in USA, Machaon in Russia, and Magoxid-Coat in Germany [7]. Some of the applications are listed below:

1. Aerospace and automotive applications

Light metals provide good properties such as low density, high specific strength, and electromagnetic shielding. The ceramic coatings made by PEO on light metal alloys exhibit excellent adhesion, corrosion resistance and low conductivity characteristics, and they are quite stable at high temperature and resistant to thermal shock [57-60]. Therefore, PEO coatings are employed to withstand mechanical stress, corrosion, and high temperature in aerospace and automotive industries. PEO coated Mg alloys can be applied in different areas as brackets, cylinder blocks, piston and gearbox [61]. For example, black anodized Mg-Li alloys have been used for thermal loaded internal parts of space vehicles [62]. PEO coatings are also proved to be useful as thermal barrier layers and can be used for high-power electronics and LED lighting systems.

2. Application for textile industry and fashion accessories

PEO coating can be used in machine building, high speed machine structural parts of textile machine, frames of ultra light weight racing and mountain bikes. Increasing interest is also seen for surface protection of fashion accessories, such as wrist watches, sun glasses, mobile phone and computer cases [63].

3. Biomedical applications

Surface modification of Mg and Ti implants by deposition of bio-compatible coatings has been of interest to the bio-medical industry. The PEO process usually uses nontoxic electrolyte and produces low pollution. The porous morphology created on metal implants by PEO and hydroxyapatite (HA) coating have been proved to help tissue growth [64,65]. In the past

decades, PEO treatment of magnesium has become popular in biomaterial applications as ligature wires, vessel anastomosis connectors, aneurysm treatment wires, artificial joints, etc.[66] because of good coating corrosion resistance and mechanical properties. The composite coatings made of PEO coating together with polymer-based or Ca–P based coatings are becoming more attractive as advanced coatings for biomedical application [67,68].

4. Catalysis

PEO coatings generally exhibit improved surface performances in terms of porous structure, strong adherence and good corrosion resistance, which show considerable potential for application as a carriers and a catalytically active structures in catalysis [69]. PEO treated aluminum foil was investigated as catalysts for diesel exhaust gases clean-up, and the bus converters equipped with these catalysts showed high and stable performance during the field tests [70]. Rudnev et al. [71] conducted an investigation on the use of PEO coatings as catalysts in CO oxidation and found that the PEO technique is a promising novel process for forming catalytic layers. Using PEO structures as a substrate for subsequent deposition of the catalytically active components by methods of impregnation, extraction, and sol-gel synthesis allows one to form the developed surfaces with nanowires, nanospheres, hedgehog-like structures [72]. Therefore, PEO technique is of particular importance in terms of the development of catalysts and methodologies for obtaining catalytic active layers on the microstructured channels [72].

1.5 Models of PEO process

Abundant literature was devoted to understanding the complex mechanisms involved in the PEO processing of metals. Many studies provide qualitative models describing the phenomena of coating growth and discharge evolution. According to [73], there are four different kinds of models developed to describe the PEO process, namely phenomenological models, theoretical models in oxide layer, equivalent circuit models and empirical models of operational characteristics.

Phenomenological models describe the PEO process based on the relationship among processes during plasma electrolysis, evolution of microdischarges in oxide pores and evolution of microdischarges and crystallization of oxides. The references [33-45] mentioned before describing the PEO process belong to the group of phenomenological models. In Ref. [12], the relationship between the principal physical–chemical processes occurring in plasma

electrolysis and the basic electrode processes of classic electrolysis in the techniques of plasma electrolytic processing is discussed. Four stages of the process, characterized by different mechanisms of anodic reactions were revealed. Stage I corresponds to anodic oxidation of Al with approximately 100% current efficiency. In stages II and III, the oxide growth rate is substantially reduced due to the prevailing processes of anodic dissolution and phase recrystallization of the oxide film. In stage IV, plasma chemical reactions at the anode–electrolyte interface govern the film growth. The study provided a better understanding of the physical and chemical background of the plasma phenomena occurring on the electrode during electrolysis. Microdischarge evolution in the pores of oxide layers and the kinetics of ceramic coating formation during PEO processes have been discussed based on experimental observations [73-75]. According to [76], model concepts on the mechanism of PEO related to coating growth location and rate, current density in discharge channel, et al. are developed based on a critical analysis of literature data. The authors assumed that the coating grows mainly in microdischarge channels and neighboring coating areas and the coating growth rate on the surface of any conducting material is a function of the energy liberated in the microdischarge channel and the surface density of microdischarges. Besides, they believed that the decrease in the current during a MAO (micro-arc oxidation) process carried out at a stabilized anodic voltage does not automatically result in a decrease in energy liberated in a discharge channel, but due to the even more pronounced decrease in the density of microplasma discharges in certain intervals of this process. The correctness of these model concepts is confirmed empirically by experimental results on the average growth rate of oxide-ceramic coatings for different duration of the PEO process on several alloys.

Equivalent circuit models involve resistive model circuits, resistive and capacitive model circuits and nonlinear circuits. In [76], the authors developed simplified equivalent circuits of the PEO process for samples and parts of "simple" and "intricate" (Fig.1.13) geometric shapes. Their use allows choosing the optimal electric modes and technological procedures aimed at applying coating uniformly in both thickness and performance. Mamaev et al. [77] proposed a parametric model, which interrelates current density, applied voltage, time, specific active resistance, and specific capacitance of electric layers at a metal/solution interface during the formation of oxide coatings under micro-arc oxidizing conditions. It can be used for modeling the operation of industrial equipment, calculating and designing power sources, and determining the controlled variables of micro-arc systems. Based on the parametric model and variables proposed, as well as the type of the polarizing voltage and the area treated, one can

calculate the total, active, and capacitive current values as functions of the process duration. Parfenov et al. [78] developed a methodology for obtaining the frequency response of the plasma electrolytic process on aluminium. The frequency response was evaluated as a complex impedance of the electrolyser during the PEO. It was found that the impedance magnitude decreases from 10^3–10^4 to 10–10^2 Ω with frequency growth from 0.2 kHz to 20 kHz and the phase angle decreases from 0 to − 70 − 80°. Evolution of the frequency response during PEO was consistent with that of the surface state; therefore, it can be used for process diagnostics and control. The circuits formed by resistive elements [79] are mainly used for DC modes, whereas those made by resistive and capacitive elements [78, 80] can be used for pulsed PEO and the nonlinear circuits [76] which apply to AC PEO conditions.

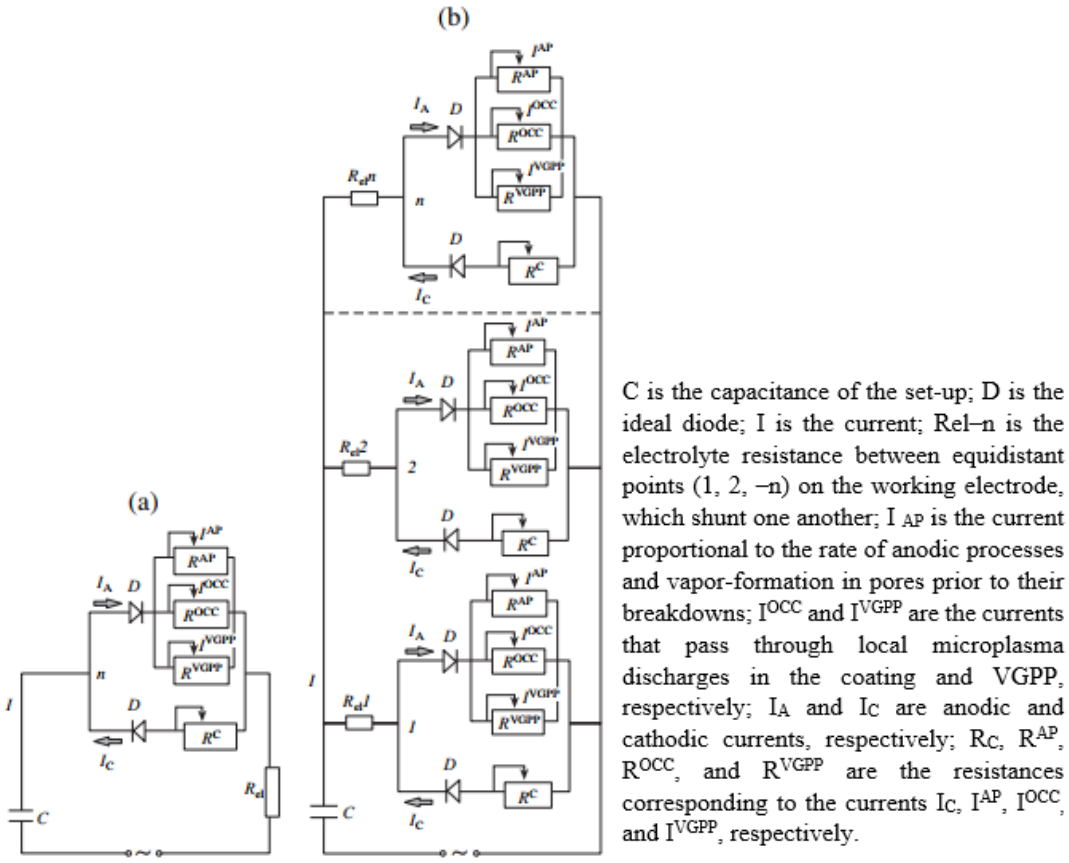

Fig. 1.13 Equivalent circuits of PEO on samples of (a) “simple” and (b) “complicated” geometric shapes (with permission from Ref. [35]).

The third group consists of theoretical models of processes in oxide layer focuses on metal-dielectric-electrolyte system [80]. This group is tightly connected with equivalent circuit models which can be obtained from the impedance spectra and current–voltage characteristics. According to Mamaev et al. [77], the dependences of the specific active resistance and

capacitance of the metal/solution interface on the duration of the PEO process can be described by polynomial equations. But electrochemical measurements are necessary to be performed to determine the corresponding coefficients. Gordienko et al. [81] proposed a method of formation of oxide coatings on anodically polarized electrodes under galvanostatic mode with computer-controlled measuring, processing, and calculation of electric parameters. Voltammetric characteristics of these processes are considered using a variable reactive resistance. It is shown that a thermal breakdown is preceded by an electric breakdown of potential barriers formed in the metal–oxide–electrolyte system. Ikonopisov [82] proposed a theoretical model of breakdown caused by an avalanche of electrons injections at the electrolyte/oxide interface. In this model, equations describing the dependence of the breakdown voltage upon the electrolyte resistivity, field and temperature were proposed. The equations interpreted the empirical relation between the breakdown voltage and the nature of the anodized metal and the electrolyte composition. Many other factors like the current density, the surface topography of the electrode, the history of the film formation, do not affect the breakdown voltage noticeably.

Empirical models help to estimate dependencies between the process parameters (voltage, current density, electrolyte etc.) and the microstructural features, for example, coating thickness and roughness [82,83]. According to Albella et al. [83], a model describing the avalanche-breakdown during the growth of anodic tantalum oxide was built based on the empirical relations between the breakdown voltage and anodization parameters. They assumed that the oxide thickness increases linearly with the voltage under constant current mode. The thickness of coating can be estimated by the coating-forming voltage and the breakdown voltage under constant current mode and the results are interpreted assuming that the injected current has its origin in the electrolyte anions incorporated into the oxide during the anodization process. Mamaev et al. [84] proposed a model of formation of nanostructural inorganic coatings based on a physical-chemical assumption of a microplasma process for the case where high-energy flows are localized in nanolayers of the metal-electrolyte interface. A basic equation for the mass of the material of the resulting inorganic nonmetallic coating for the collective microplasma process was derived:

$$m(x,y) = -0.5zFD^{0.5}(C_0 - C_s)\mathrm{erfc}\left[\frac{x}{2\sqrt{Dt}}\right]_{x=0}\frac{\tau}{N} \qquad (1.1)$$

The equation showed that the local mass of the material of the resulting inorganic nonmetallic coating is dependent on many factors. It is an intercorrelation between the number of

microplasma discharges N, microplasma process time t, the single pulse duration τ, mass of the resulting coating material *m*, charge number *z*, the diffusion coefficient *D*, volume concentration C_0, surface concentration C_s and coating thickness growth rate. Unfortunately, there are no experiments available that can confirm the correctness of this model.

These four types of models mentioned above are dependent on each other. Phenomenological models rely heavily on experimental data and thus provide fundamental understanding towards the mechanisms of PEO process and help establish correct information and strategies for other kinds of models. Equivalent circuit models are often used in combination with theoretical and empirical models. Commonly, most studies combine more than one kind of model to describe the PEO process. Among all those models, the most developed models for PEO process are phenomenological and empirical models. However, empirical models provide an insufficient level of generality and the issue related to phenomenological models lies in a lack of means to formalize the behavior observed in specific experimental studies [73]. The descriptive phenomenology of PEO process has not changed much since 1991 [75] to recent publications, but up to now few papers provide complete modeling for describing the whole PEO process numerically. Only Caire et al. [85] developed a model to simulate the PEO of magnesium and aluminum in direct current galvanostatic mode. In this model, they assumed that dielectric breakdown is due to the increase in the electric field at the barrier layer situated at the bottom of pores and simulated the growth of the coating by use of an equivalent resistive network. The results presented the evolution of current density, electric field and coating thickness during PEO process. The model reproduced the experimental results reasonably well at the beginning of anodization, but it is not yet able to provide a fair quantitative prediction of all the PEO effects because it is not calibrated with experiment.

Although a range of partial PEO models has been developed, none of them covers all the varieties of processing conditions due to the complexity of PEO process. It is still a major challenge to describe the PEO process theoretically. The model concepts put forward by Rakoch [76] requires detailed research into a wide range of parameters. The locations, duration, number and responsible energies of plasma discharges are still needed to be characterized precisely. Parfenov [73] overviewed the present methodological approaches to process modelling and proposed a generalized phenomenological model structure, which can be seen in Fig.1.14. The model describes the ‘power supply–electrolyser–treated surface’ as a system with parameters which characterize integral properties of the surface layer and integral

parameters of the process. A further progression of the modelling needs to consider the proposed phenomena in the structure as complete as possible and contribute to the dynamic simulation instead of static models for process control. In the future, combining this phenomenological model structure with plasma physics, materials science, electrochemistry, electrical engineering, computer mathematics and computer science ultimately would contribute to the development of PEO technology and addressing key challenges of modern manufacturing.

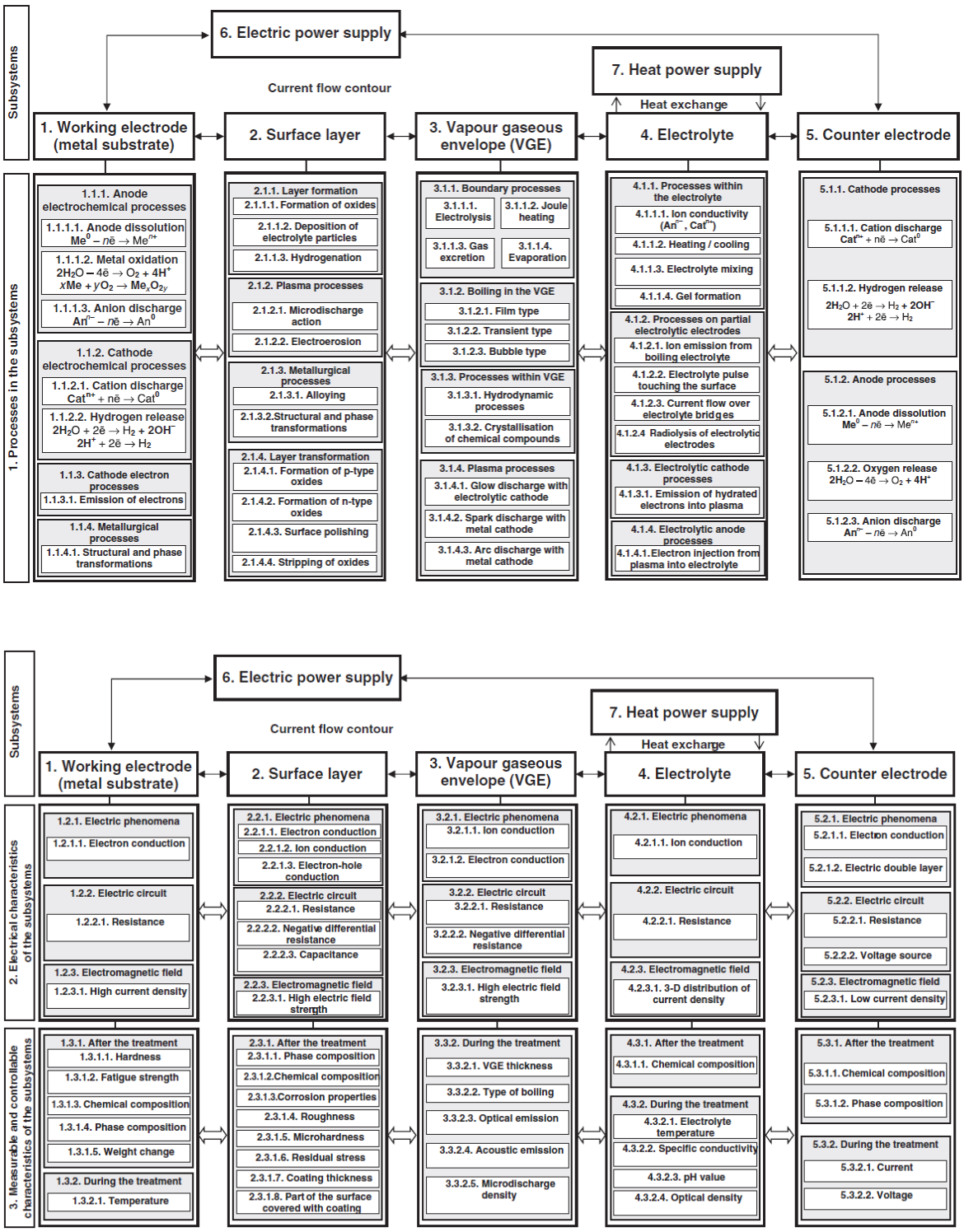

Fig. 1. 14 Generalised phenomenological model structure (with permission from Ref. [73]).

2. Motivation and objectives

PEO process is used in particular to improve surface hardness, abrasion resistance, heat and electric insulation and corrosion resistance. It is very attractive from an industrial point of view. In the meantime, PEO is a complex process combining concurrent partial processes of metal dissolution, anodic oxide film formation and dielectric breakdown. The dominance of the partial processes depends on the nature of both the metal and electrolyte, as well as on the current regime employed [8]. PEO is also known as microarc oxidation, anodic spark electrolysis and microplasma oxidation because of the different understandings of researchers to the mechanism of this process [76]. Even though PEO has attracted a lot of attention and has been intensively studied since it was discovered in the 1880s, the underlying mechanisms of plasma generation and coating formation are still not fully understood.

Many studies provide qualitative models describing the mechanism of coating growth and discharge evolution [44,73-75,84-91] including phenomenological and empirical approaches. However, empirical models provide an insufficient level of generality and another issue related to phenomenological models lies in a lack of means to formalize the behaviors observed in specific experimental studies [73]. Up to now only a few papers provide mathematical models for describing the PEO process. On the other hand, the PEO process is affected by many factors such as current regime, the properties of the substrate, the composition of the electrolyte, treatment duration, and geometry of the electrolyser. Most literature rely only on experiments to investigate the effects of different parameters on the PEO process, which is insufficient to have an integral understanding of the PEO process and inconvenient for industrial application to study PEO coatings when some parameters are changed.

Simulations have become an effective way to target operational concepts and to evaluate the behavior of complex systems, offering the opportunity to examine the complexities of the experimental environment in a non-intrusive and cost-effective way. They offer the means to evaluate, assess, and fine-tune equipment selections and operational factors. Also, they are able to estimate the impact of new equipment, and/or procedures within operational parameters, making a significant difference when ready to operate [92].

Therefore, the general objectives of this work are to build a precise numerical model for describing the PEO process under potentiostatic mode for magnesium-based substrates and then verify the model through several different experiments to make sure it can be applied in

different occasions of PEO process. Using such a model one can design the process and adjust its parameters in order to obtain PEO coatings with certain defined properties. The thesis includes three main subtopics:

1. Modelling and simulation of PEO coating growth on AM50 Mg alloy under constant voltage mode.
2. Application of modelling and simulation in investigation of electrode distance impact on PEO coating formation.
3. Application of modelling and simulation in investigation of substrate geometry impact on PEO coating formation.

The details of the objectives are listed as follow:

- Providing reasonable assumptions and mechanisms for the coating growth and discharge evolution based on the current understanding of the PEO process.
- Studying the effect of the treatment time on the evolution of coating morphologies, composition, and thickness values experimentally to provide necessary data input for the modeling and simulation.
- Building a model describing the PEO coating growth and the discharge evolution by, and comparing the simulation results with the experimental results to verify the correctness of the assumptions and the mechanisms of the PEO process in the modeling.
- Studying the influence of the substrate geometry on the PEO coating formation and uniformity at different locations experimentally and explain the effect by a model of the PEO process.
- Investigating the influence of the electrode distance on the PEO coating morphologies, composition, and thickness values experimentally and explain the effect by modeling and simulation complementary.
- Providing a routine model for coating thickness prediction under various input parameters.

3. Experimental methods

This chapter gives information in detail regarding the experimental methods used in the present study.

3.1 Coating preparation

3.1.1 Experimental set-up

In the present study, the PEO process was carried out using a DC power supply under constant voltage. The set-up of the experimental system unit is shown in Fig.3.1. Fig.3.2 demonstrates the schematic of the experimental PEO set-up.

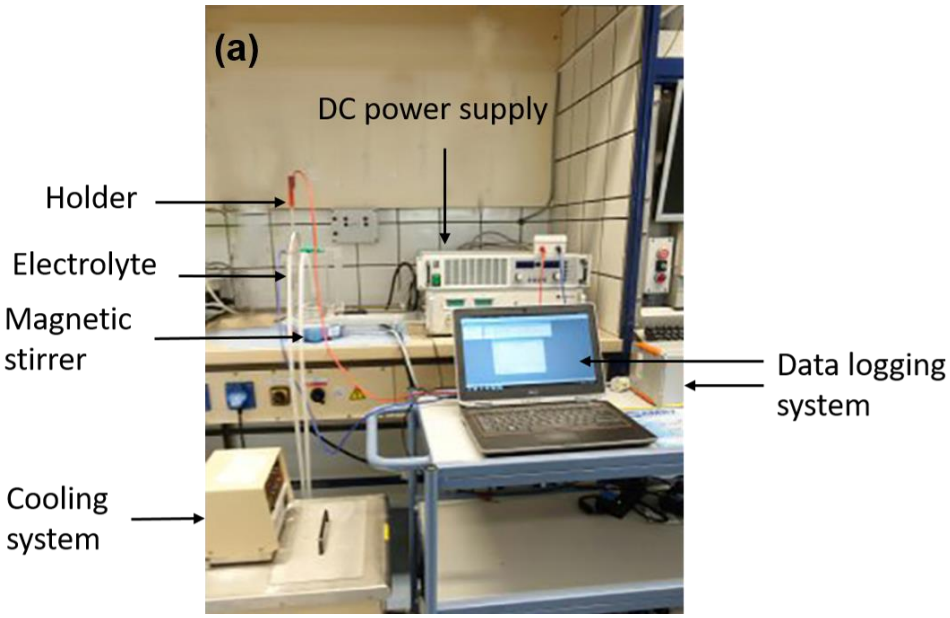

Fig. 3.1 Experimental set-up of the PEO system

The substrate and a stainless steel electrode with dimensions of 50 mm × 50 mm × 4 mm serving as the anode and cathode respectively were located face to face and connected to a DC power supply (EA Elektro-Automatik, EA-PS 8720-15 2U RS). The samples were immersed in the bath at a depth of 30 to 50 mm beneath the electrolyte surface. A metal rod with a PTFE jacket is typically used as a holder to connect the anode to the power supply. A water cooling system was used to control the temperature of the electrolyte. A magnetic stirrer ensured uniform the distribution of the ions in the electrolyte during PEO processing. After cooling and mixing of the electrolyte, the working voltage could be applied to the electrolyser terminal and

adjusted at the power supply in accordance with the constant voltage regime. The evolution of the voltage/current during PEO processing was recorded by a data logging system.

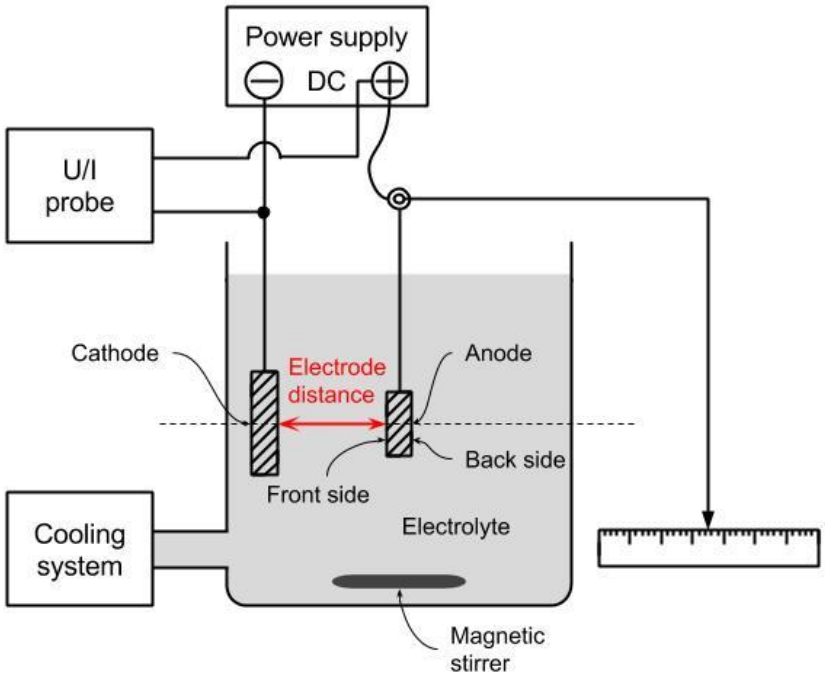

Fig. 3.2 Schematic representation of the experimental set-up.

3.1.2 Preparation of substrate samples

Specimens of AM50 magnesium alloy were cut into dimensions of 15 mm × 15 mm × 4 mm from gravity cast ingot material. By using Arc Spark OES (Spark analyser M9, Spectro Ametek, Germany), the nominal composition (wt %) of AM50 alloy was determined as 4.74 wt. % Al, 0.383 wt. % Mn, 0.065 wt. % Zn, 0.063 wt. % Si, 0.002 wt. % Fe, 0.002 wt. % Cu and Mg balance. Prior to PEO processing, the substrates were firstly ground successively by 320, 500, 800, 1200 grit emery sheets, degreased in ethanol, rinsed in distilled water and finally air-dried.

3.1.3 Preparation of electrolyte

The electrolyte was prepared by adding KOH (1 gL^{-1}) and Na_3PO_4 (10 gL^{-1}) to deionized water and the volume of the electrolyte used in the experiment was 2 L. Additionally, a cooling system maintained the electrolyte temperature at 10 ± 1 °C. After the reagents were totally dissolved, the pH value of the electrolyte was 13 and the electrolyte conductivity was 1.5 S/m at the present temperature.

3.1.4 Fabrication of PEO coatings with different treatment times

Specimens with dimensions of 15 mm × 15 mm × 4 mm were cut from an AM50 magnesium alloy ingot. The electrode distance between anode and cathode was 80 mm with an accuracy of ± 1 mm. The PEO process was carried out under a constant voltage of 350 V with different treatment times of 10 s, 30 s, 1 min, 2 min, 4 min, 6 min, 8 min and 10 min respectively. The process were carried out under constant voltage of 350 V with an initial current of 15 A. The current response was recorded by a data acquisition system.

3.1.5 Fabrication of PEO coatings with different electrode distances

A schematic of the experimental system unit is shown in Fig. 3.2. The electrode distance was adjusted with an accuracy of ± 1 mm and the current evolution during PEO process was recorded. The anode surface facing the cathode was defined as the front side, and its opposite side was defined as the back side. PEO process was carried out under a constant voltage of 350 V for 10 min with a pre-set current of 15 A. Coatings were produced at distances of 10 mm, 20 mm, 40 mm, 60 mm, 80 mm, 100 mm, 120 mm and 240 mm respectively.

3.1.6 Fabrication of PEO coatings with different geometries

Holes with different diameter were drilled in the center of standard samples (25 mm × 25 mm × 4 mm). The diameters of the holes were 0.5 mm, 1 mm, 2 mm, 3 mm, 4 mm and 6 mm respectively. For each sample, the inner round area around the hole was defined as the round surface, and the outer flat surface was defined as the flat surface. The anode surface facing the cathode was defined as the front side and the opposite surface was defined as the back side. The distance between anode and cathode was adjusted to 80 mm with an accuracy of ± 1 mm. PEO process was carried out under a constant voltage of 350 V for 10 min.

The schematic diagram of the experimental set-up is shown in Fig. 3.3. A line near the top of the hole (marked in blue in Fig. 3.3) from the front side to the back side was selected to determine the thickness distribution by cross-sectional SEM micrographs of the round coating for each sample.

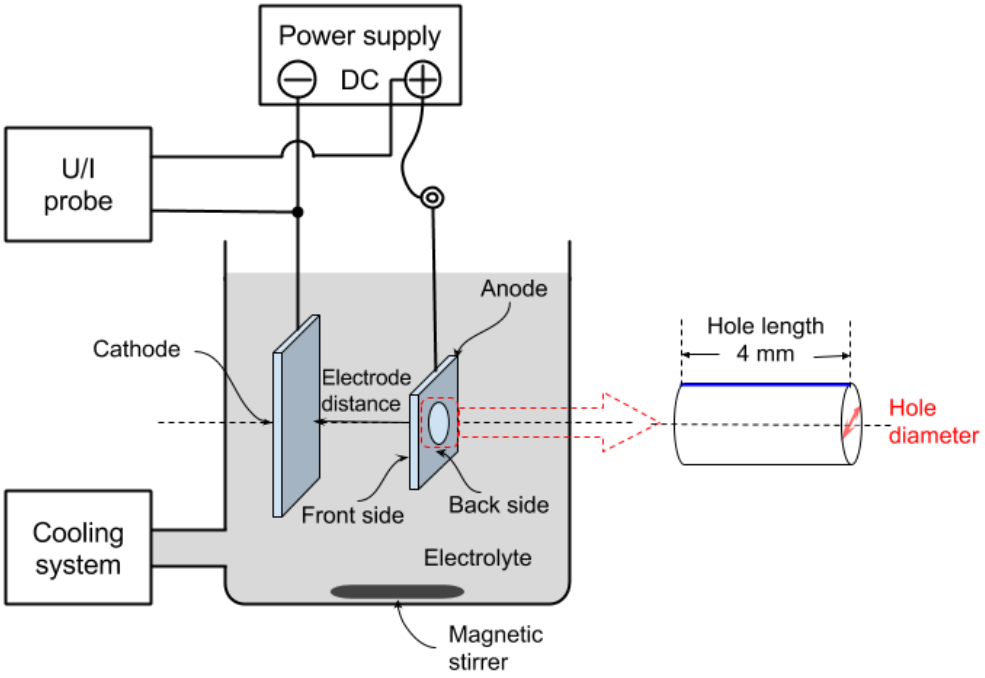

Fig. 3.3 Schematic diagram of the experimental set-up. The predefined diameters of holes in the center of AM50 anode range from 0.5 mm to 6 mm.

3.2 Coating characterization

3.2.1 Scanning electron microscopy

A scanning electron microscopy (SEM), TESCAN Vega3 SB, was used to study the sample morphology and topography in both surface plane and cross-section of PEO coatings in both secondary electron and backscattered electron modes. An energy dispersive X-ray spectroscopy (EDS) detector from EumeX (IXRFsystems) attached to the SEM instrument was used to quantify the coating composition. The function of EDS linescan and mapping are used to study the distribution of elements on both surface and cross-sectional images. Prior to characterization, PEO coated samples were sputter-coated with Au in order to prevent surface charging for the low-conducting ceramic coatings. To avoid the influence of Au, sputtering was only used for SEM investigations and not for EDS analysis. SEM was operated at 15 to 20 kV. For observing the cross-sectional morphology, the coatings were embedded into resin and then prepared by polishing successively using 500, 800, 1200, 2500, and 4000 grit emery sheets, following by disc polishing using colloidal silica suspension.

3.2.2 X-ray diffraction analysis

The phase composition of the PEO coated sample was determined by X-ray diffraction measurement (XRD) with Cu-Kα radiation using a Bruker D8 advanced in GI parallel beam mode with 3° incident angle. The measurements were performed at 40 kV voltage and 40 mA current, with a step size of 0.02 degree and 1 s for each step. Quantitative analysis of the crystalline phases of the PEO coatings via Rietveld analySIS was conducted using the software X'Pert HighScore Plus software package, version 2.2e.

3.2.3 Measurement of coating thickness

Two different methods were utilised to test the coating thickness. The first method was using an eddy-current gauge (MiniTest 2100, Electrophysik, Germany) to determine the thickness: the meter was set to zero-position for the uncoated substrate and then the ceramic coating thickness was measured after the sample was coated. The resolution is about 0.1 µm with measurement ability in the range of 1 to 200 µm. The second method to estimate the coating thickness was to measure the thickness from the cross-sectional SEM micrographs by using Image analysis software analySIS pro 5.0. For each treatment condition, the average coating thickness was estimated from at least five locations on the respective coating selected randomly for statistical reasons.

3.2.4 Measurement of surface porosity

By Image analysis software analySIS pro 5.0, surface porosity was measured based on scanning electron microscopy incorporating digital image processing. The backscattered electrons (BSE) are used to detect contrast between areas on the sample surface with different chemical compositions. The signals of the secondary electrons gives information on the surface topography. In PEO coatings, ceramic phases with high atomic number elements backscatter electrons more strongly than pores with low atomic number elements, resulting in contrast between them. Then the digital porosity measurements are performed based on the contrast which seperates the porosity voids from the rest of the objects in the image [93]. The dimension, shape and the number of pores can be inspected. For each treatment condition, the surface porosity was estimated from ten different locations of the respective coating selected randomly for statistical reasons.

3.2.5 Measurement of surface roughness

Surface roughness measurements were carried out by a Hommel profilometer (HOMMEL TESTER T1000). A non-contact 3D surface measurement system (U-surf, NANOFOCUS) was also used for topographical observation of the PEO-coated samples. Surface roughness was commonly characterized by arithmetic mean roughness (Ra) and root mean square roughness (Rq). In this study, the arithmetic mean roughness (Ra) was used to characterize the roughness of the PEO surfaces. For each sample, at least 3 tests were performed at different locations of the sample for statistical reasons.

3.3 Corrosion resistance

Electrochemical measurements were performed on the coated samples, using the same electrolyte that employed for the PEO process in order to evaluate the coating resistance in the electrolyte. The impedance of the PEO process was studied on the samples with the predetermined coating thickness.

An ACM Grill AC computer controlled electrochemical workstation was used for the measurements. A PVC cell (333 mL) was employed with a three electrode configuration consisted of a platinum plate as the counter electrode, a Ag/AgCl reference electrode and the coated specimen as working electrode.

The exposed area of the coating surface for electrochemical test was 0.5 cm^2. Before the EIS study, the evaluation of the open circuit potential (OCP) is needed. The OCP is defined as the potential at which no current occurred. Usually the OCP study takes a considerable amount of time after the initial immersion of the sample, which is about 10 min in this work. After the steady state is established, EIS can be carried out by applying a sinusoidal potential perturbation of 5 mV RMS (for bare alloys) or 10 mV RMS (for coated alloys) around this potential, with the frequency swept from 100000 to 0.1 Hz. After the data acquisition, Zview software was used to fit Bode plots with designed equivalent circuits.

4. COMSOL Mutiphysics modelling

During PEO process, the current density and the distribution of anode current in the whole surface of the specimen play an important role in the formation of ceramic coatings. Since experiments do not offer direct access to the current distribution, especially at the sample surface, one approach to gain a better understanding of this issue can be accomplished numerically by using modelling and simulation tools. COMSOL Multiphysics software is a finite element analysis and solver software package for various physics and engineering applications, especially coupled phenomena or multiphysics. Therefore, it is a suitable and powerful tool to study the complexity of the PEO system.

4.1 Introduction of COMSOL Multiphysics

COMSOL Multiphysics is a general-purpose software platform, based originally on the MATLAB programming language and integrated development environment, for modelling and simulating physics-based problems. It includes a complete environment for modeling any physical phenomenon that can be described using ordinary differential equations (ODEs) or partial differential equations (PDEs). In several sections of industrial developement, COMSOL has now become the industry standard for multiphysical modeling, research, design, and development [94]. With COMSOL Multiphysics, coupled or multiphysics phenomena can be simulated.

One of the advantages of COMSOL is that it is a flexible platform that allows users to model all relevant physical aspects of their designs without an in-depth knowledge of mathematics or numerical analysis. Expert users can go deeper and use their knowledge to develop customized solutions, applicable to their unique circumstances. Many predefined multiphysics interfaces provide easy-to-use entry points for common multiphysics applications.

Another noticeable trait of the COMSOL platform is adaptability. If any physical effect is in need, or one of the inputs to the model requires a formula, it can be just entered. Using tools like parameterized geometry, interactive meshing and custom solver sequences, one can quickly adapt to the ebbs and flows of specific requirements. Parameter sweeps and target functions can be executed directly in the user interface. Using these physics interfaces, various types of studies can be performed including: Stationary and time-dependent (transient) studies, linear and nonlinear studies, and frequency response studies.

4.2 Finite element method

In the add-on modules of COMSOL Multiphysics, several different methods are used, including finite element analysis, the finite volume method, the boundary element method, and particle tracing methods, but the emphasis is on the finite element method (FEM) because it is the most commonly used in COMSOL and the only method used in the current work. The finite element method is a numerical method for solving problems of engineering and mathematical physics based on breaking down a complicated object into smaller parts which are easy to control [95]. The analytical solution of these problems generally requires the solution to boundary value problems for partial differential equations. To be able to break down a strong PDE-based formulation to a collection of geometrically simple subdomains, the strong form must be transferred into a so called weak form because the field variables are required to be continuous and have continuous partial derivatives up to the order of the equation. The weak forms have the same but relatively weaker constraint conditions, which are discontinuous and integrable. The finite element method formulation of the problem results in a system of algebraic equations. The method yields approximate values of the unknowns at a finite number of discrete points over the domain [96]. To solve the problem, it subdivides the complicated object into new formations such as triangles, tetrahedrons and hexahedra, which are called finite elements to create a mesh. The simple equations that model these finite elements are then assembled into a larger system of equations that models the entire problem. FEM uses variational methods from the calculus of variations to approximate a solution by minimizing an associated error function. Typical problem areas of interest include structural analysis, heat transfer, fluid flow, mass transport, and electromagnetic potential. Figure 4.1 shows an example of the finite element mesh for a circle.

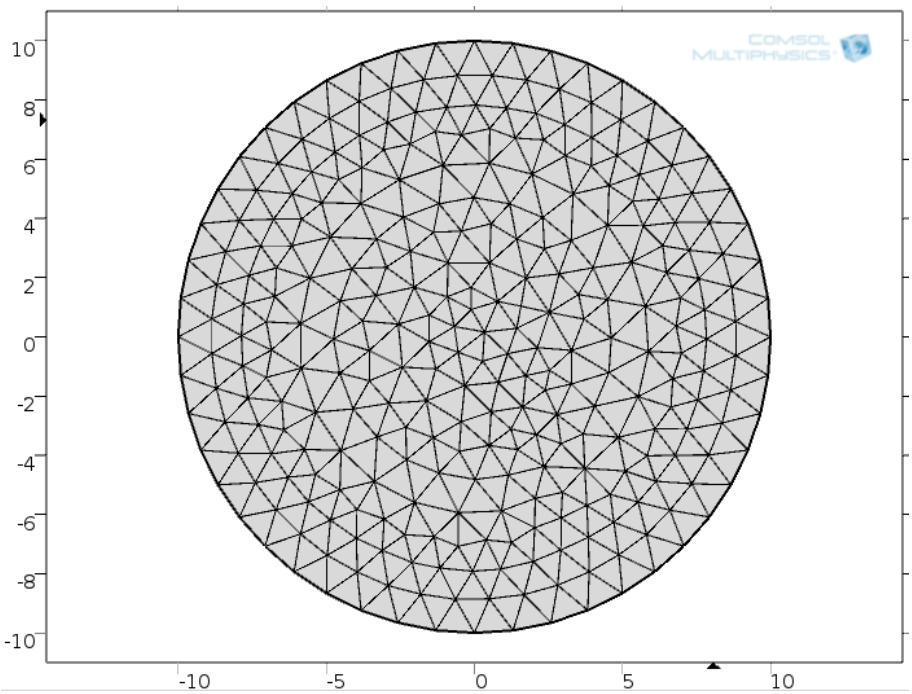

Fig. 4.1 Complete mesh for circle object (consist of 546 domain elements and 48 boundary elements)

4.3 The solvers and convergence

When solving the models, the software runs the finite element analysis together with adaptive meshing (if selected) and error control using a variety of numerical solvers.

In COMSOL, there are two fundamental classes of algorithms that are used to solve the linear equations, direct and iterative methods. The direct solvers used by COMSOL are the MUMPS, PARDISO, and SPOOLES solvers. All those solvers use the matrix form of Gaussian elimination to get the same solutions for the same linear equations. The solvers differ primarily in their relative speed. PARDISO tends to be the fastest and SPOOLES the slowest, but SPOOLES tends to use the least memory of all of the direct solvers. From the point of view of the solution, it is irrelevant which one of the direct solvers is chosen, as they will return the same solution for all well-conditioned finite element problems.

The iterative solvers in COMSOL encompass a variety of approaches, such as conjugate gradient method, generalized minimal residual method and biconjugate gradient stabilized method. Contrary to direct solvers, iterative methods approach the solution gradually, rather than in one large computational step. They are available to solve linear and non-linear

equations. For example, when solving the equation below trying to find x such that $f(x)=0$ in the range of $(0, \pi)$,

$$f(x) = \sin x - x^2 \tag{4.1}$$

COMSOL will automatically use its non-linear solver and the COMSOL nonlinear solver uses a Newton-Raphson iteration method. An initial guess for the dependent variable $x_0 = \pi$, and an evaluation of the function, $f(x_0)$, as well as its derivative, $f'(x_0)$ are required.

$$f'(x) = \cos x - 2x \tag{4.2}$$

This gets us to the next point x_1.

$$x_i = x_{i-1} - f(x_{i-1})/f'(x_{i-1}) \tag{4.3}$$

If this would be a linear problem, this algorithm converges in one iteration, regardless of x_0. However, for this nonlinear function, x_1 is not an exact solution but it can be seen as the starting point for the next solution. When nonlinear problems are in question, the convergence criteria for the iterative Newton process also must be considered. A typical approach would be to compute the change of the residual for each step:

$$r_i = f(x_{i-1}) - f(x_i) \tag{4.4}$$

Then Newton-Raphson iterations are performed and terminated when it is within some desired tolerance. From the results in Table 4.1, it can be seen that after seven Newton-Raphson iterations starting from $x_0 = \pi$, the solution has converged to within a tolerance of 2.5e-9. Therefore, when solving nonlinear functions, the tolerance determines how close the residual gets to 0. Usually the default for the tolerance is 0.001. The Newton-Raphson method also works well for large systems of non-linear equations.

Table 4.1 The results of the function, its derivative and the relative error after different iterations

i	x_i	$f(x_i)$	$f'(x_i)$	$f(x_i)- f(x_{i-1})$
0	3.1415926	-9.869604	-7.28319	
1	1.786470666	-2.2146451	-3.78695	7.65495887
2	1.201660573	-0.5113486	-2.04251	1.70329653
3	0.951307719	-0.0908109	-1.322	0.42053772
4	0.882615491	-0.0066074	-1.1301	0.08420349
5	0.87676874	-4.737E-05	-1.1139	0.00656004
6	0.876726218	-2.503E-09	-1.11378	4.7363E-05
7	0.876726215	0	-1.11378	2.5031E-09

Much of the presented simulation work involves solving nonlinear models, and the convergence of these models is one of the main challenges. When using the Newton iterative method to solve these problems, considerable effort is required to provide the best possible initial guess. It is suggested that at least an order of magnitude guess is generally required. When it is not possible to estimate an initial guess that is close enough, it may help to run the simulation several times, each time incrementally approaching the desired state.

5. Modelling and simulation of PEO coating growth on AM50 Mg alloy under constant voltage mode

The main objective of the present chapter is to simulate the PEO process under potentiostatic mode for AM50 magnesium alloy using a combination of a phenomenological approach and a numerical model. In order to achieve that, it is necessary to provide reasonable assumptions and mechanisms for the coating growth and discharge evolution based on the current understanding of the PEO process. Therefore, we study the effect of the treatment time on the evolution of coating morphologies, composition, and thickness values experimentally to provide necessary data input for the modeling and simulation. The PEO process is described by a simplified equivalent electric circuit [76] which will be shown in the modelling and simulation part later. A typical problem in this research is the mechanism of fast proceeding microplasma processes and the kinetics of ceramic coating formation. By combining the equivalent circuit of PEO process with the modified point defect model of Pyun et al. [97], the processes of micro plasma discharges and coating growth are described in detail in section 5.2. By comparing the simulation output with the experimental results, the growth model of PEO coating on AM50 is verified.

5.1 Data input from experiment for time-dependent model

In order to simulate the PEO process, it is necessary to have a basic understanding of the PEO coating such as the kinetics of the process and the composition of the PEO layers of the PEO coating. Hence, PEO coatings were fabricated on AM50 magnesium alloys under constant voltage with different treatment times to provide the basic information as input data for the modelling. Effects of treatment time on the morphology, composition, thickness and resistance of the resulting coatings are investigated respectively.

5.1.1 Current density evolution

The current density evolution upon the treatment time during the potentiostatic PEO processing is shown in Fig.5.1. During the process, voltage ramps fast and is maintained constant at 350 V, and the instantaneous variation of current density is recorded every second. As the treatment starts, the voltage increases in 1 s to 280 V which is a little bit higher than the breakdown voltage (240 V) of the oxide film on AM50 alloy according to the experiments. Therefore, the first second of the treatment is believed to be conventional anodic oxidation. Then the voltage

increases to 350 V in the next second and is maintained constant until the end, so the PEO process actually begins from the first second. The current density drops down rapidly from 1.6 A/cm^2 to 0.05 A/cm^2 in the following 20 s. Afterwards, the decrease rate of current density is very low and the current density is less than 0.01 A/cm^2 at the end of the process. The transient current density *j(t)* decay could be fitted in order to find the relationship between current density and treatment time:

$$j(t) = 2.997 - \frac{2.99 \times t^{1.1}}{0.8 + t^{1.1}} \qquad (5.1)$$

The fitted curve is in a good agreement with experimental values as shown in Fig.5.1 and can be used as modelling input data.

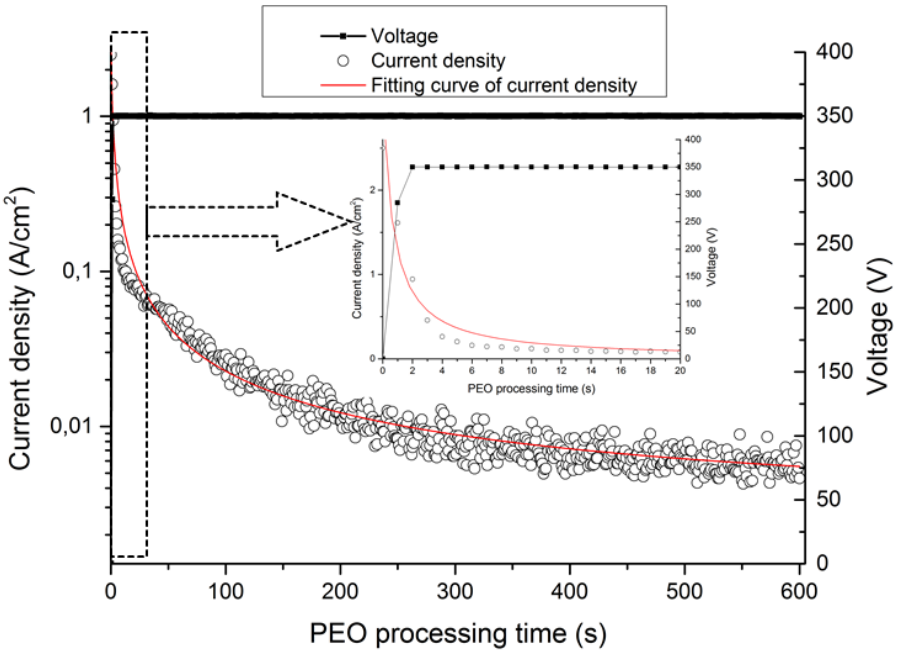

Fig. 5.1 Voltage and current density decay transient measured during 10 min PEO processing of an AM50 specimen at an applied anodic potential of 350V. The solid squares and open circles are experimental data for voltage and current density respectively, and the red solid line is the exponential fitting curve for current density.

5.1.2 Phase composition

XRD patterns of the untreated substrate alloy AM50 and the various PEO coatings formed at different treatment times are shown in Fig.5.2. The Mg peaks of the substrate are visible for all coatings. The diffraction intensities of Mg peaks decrease due to the coverage by the thin PEO film. An amorphous phase can be seen clearly at the early processing times (10-60 s). After 30

s, peaks of MgO appear firstly, and then after 60 s, peaks of $Mg_3(PO_4)_2$ show up clearly. With longer treatment times, the intensity of $Mg_3(PO_4)_2$ and MgO peaks is increasing. The diffraction intensities of the two phases increase while the peak intensity of the substrate decreases due to increasing coating thickness. A quantitative phase analysis of the PEO coated samples is performed by Rietveld analysis as shown in Table 5.1. The relative content of $Mg_3(PO_4)_2$ increases while the contents of Mg and MgO decrease as the treatment time increases, which could be attributed to the increasing thickness of the coating. The increasing ratio of $Mg_3(PO_4)_2$/MgO with longer treatment time indicates that the main composition of the outer layer is $Mg_3(PO_4)_2$, and the relative smaller contents of MgO at longer treatment times indicates that MgO might be formed mainly in a short period of treatment time at the beginning and is located close to the substrate interface. Based on XRD patterns and quantitative phase analysis of the coatings, it could be deduced that the crystalline composition of the PEO coatings are $Mg_3(PO_4)_2$ and a small amount of MgO, and MgO is mainly formed in the early stage.

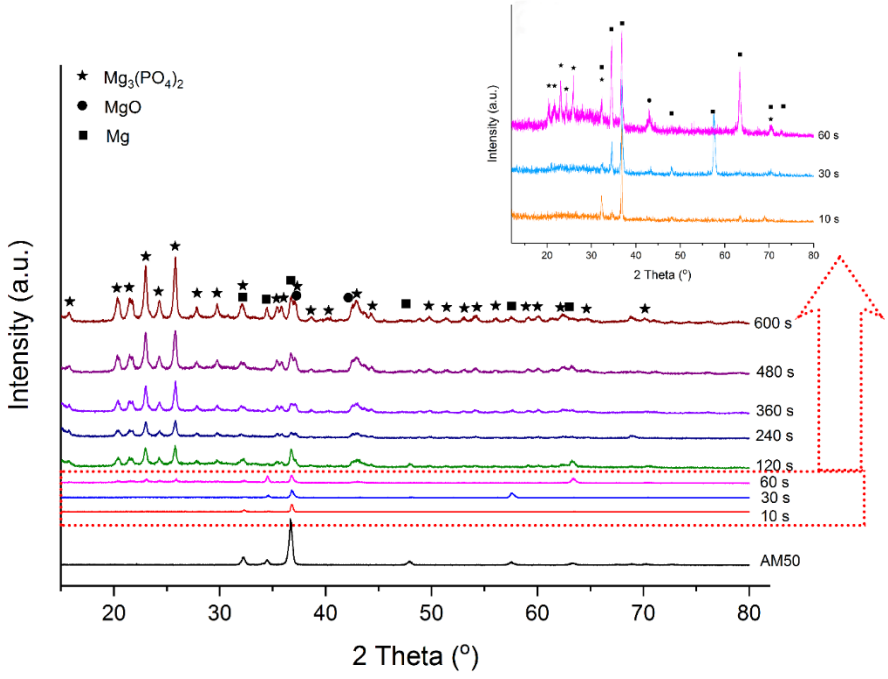

Fig.5.2 XRD diffraction patterns (GI at 3°) obtained from AM50 alloy and coated samples with different PEO treating times.

Table 5.1 Quantitative analysis of the crystal phases of PEO coated samples on AM50 alloy by XRD

PEO treatment time (s)	$Mg_3(PO_4)_2$ (wt.%)	MgO (wt.%)	Mg (wt.%)	Ratio $Mg_3(PO_4)_2$ /MgO
30	25.5	18.4	56.1	1.39
60	47.1	13.3	39.6	3.54
120	71.5	9.4	19.1	7.61
240	74.6	8.6	16.8	8.67
360	78.6	6.9	14.5	11.39
480	82.7	5.7	11.6	14.51
600	86.7	4.8	8.5	18.06

5.1.3 Element contents

For each treatment time, the elemental composition (at. %) of PEO coating was determined by EDS at 20 kV on an exposed surface with an area of 1.5 mm^2 (Fig. 5.3). The coatings, or at least the outer layer of the coatings are mainly composed by Mg, O, P and a small amount of Na, Al and K. Mg and Al are derived from the alloy. P, Na, and K are captured from the electrolyte. O comes from both the electrolyte and oxygen in the air. Even though the content of O is a bit fluctuating, the contents of the other elements are almost the same for the different treatment times, especially for Mg. The ratio of Mg: O: P is approx. 1: 2: 0.6, suggesting the possible formation of amorphous phases in the PEO coatings. There are references [98,99] showing the existence of amorphous phases in the PEO coating produced within the phosphate containing electrolyte.

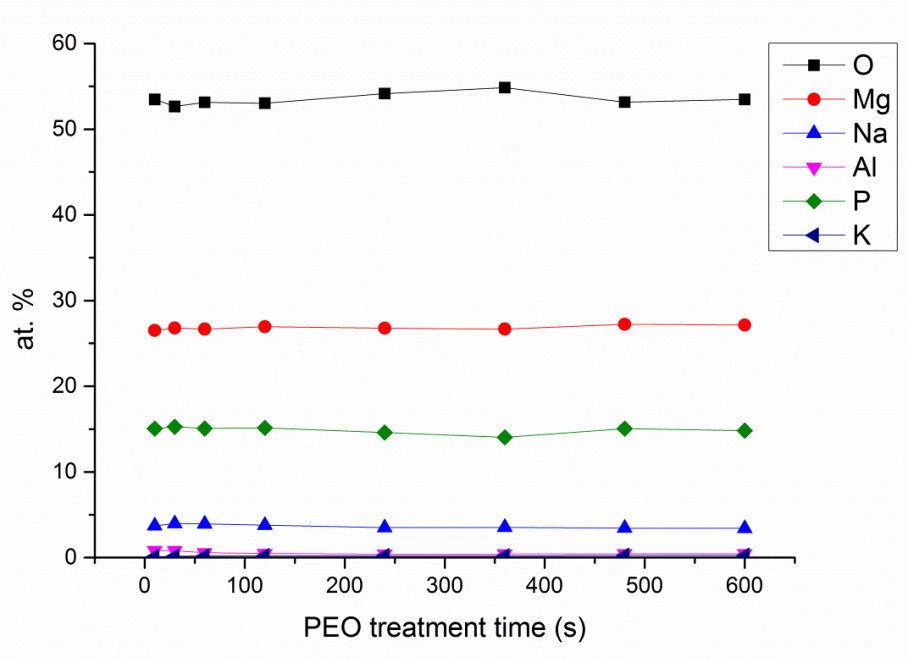

Fig. 5.3 Element composition on the surfaces of PEO coatings detected by EDS on an analyzed area of 1.5 mm^2 for different treatment times.

Cross-sectional EDS linescan of the PEO coating after 10 min treatment is shown in Fig.5.4. The distribution of the main elements Mg, O, P across the thickness of the coating from the metal/coating interface to the coating/resin interface are displayed. In the range from 0 to 2 µm, which corresponds to the barrier layer, the content of Mg decreases gradually whereas the contents of O and P increase step by step with increasing thickness. The amount of Mg element is much higher than that of P in the barrier layer. Then in the region of 2 to 14 µm, which corresponds to the outer layer, the content of each element is stable. Combined with the XRD results, it is indicated that MgO is mainly forming the barrier layer, compared with $Mg_3(PO_4)_2$ forming the outer layer. A similar conclusion is also given in Ref. [88]. Therefore, according to the experimental results, we may come to an ultimate conclusion that the coating growth during PEO process under constant potential mode includes the growth of the barrier layer from conventional anodic oxidation in the first second and the growth of the outer porous layer from the start of the breakdown discharges until the end, and the crystalline composition of the barrier layer and outer layer is mainly MgO and $Mg_3(PO_4)_2$ respectively.

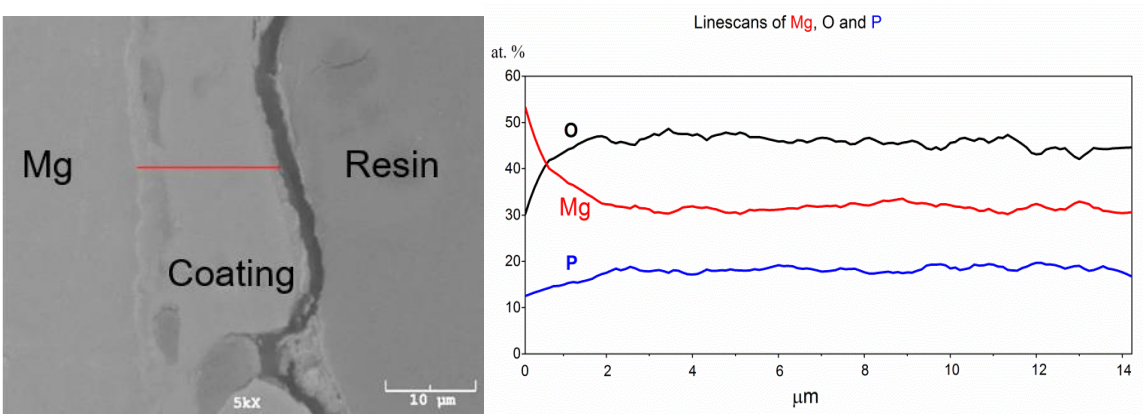

Fig. 5.4 EDS linescans of PEO coating after 10 min processing and elements distribution of the coating cross section.

5.1.4 Coating morphology

Fig. 5.5 (a-h) show the surface morphologies of PEO coatings produced on AM50 after different treatment times. Typical PEO coatings with micro pores and micro cracks were observed for all the coated samples. After 10 s treatment time, a porous film with relatively uniformly distributed micro pores is formed. Then the number of the micro pores decreases apparently but the average size of the micro pores increases over treatment time. Moreover, with longer time, most of the big pores are filled internally due to the essential of PEO process that the defects and thinner coating areas in the film always give birth to new micro-discharges [100]. Using image analysis software, the pores are distinguished as a different phase from the coatings due to their different greyscale, and the area and diameter of each hole are calculated. The number and coverage ratio of pores on the coating surfaces produced at the different times are shown in Table 5.2. Obviously, the highest pore coverage ratio is about 5% when the treatment time is the shortest. Then the absolute number of the pores and the pore coverage ratio decrease with the increasing treatment time. The absolute number of the pores decreases with increasing treatment time from 258 ± 52 at 10 s to 27 ± 11 at 600 s, and the pore coverage ratio decreases from 5.36% at 10 s to 0.44% at 600s. The diameter distribution of pores on the coating surfaces produced at the different times are shown in Fig. 5.6. The distribution range of pore diameter is becoming wider with increasing treatment time, which means that larger pores are produced with longer time. But the number of larger pores are quite small, and most of the pores are in the range of 1 to 5 µm. On the other hand, the diameter of the largest number of pores at each coating surface increases slightly from 1.5 µm at 10 s to approx. 4 µm at 600 s.

Fig.5.7 displays the cross-sectional morphologies of the PEO coatings after different treatment times. All the coatings comprise a dense inner barrier layer, a pore band and a relatively compact outer layer. The inner layers adjacent to the substrates are very thin and the thickness of the inner layers seems to remain almost the same for each treatment time. Between the two layers a pore band is visible as a clear separation line. The outer layers contain irregular pores and discharge channels, and their distribution is inhomogeneous. The interfaces of both barrier layer and porous layer display wavy-jagged appearance. Such behavior may result from the dissolution of the intermetallics [101] of the substrate at the alpha-Mg grain boundaries, which usually consists of $Mg_{17}Al_{12}$ for AM50 alloy [102]. The PEO coating treated for 10 s, is considerably more uniform and has a total thickness of about 5 μm. With increasing treatment time, the thickness of the outer layer increases while the thickness of the barrier layer shows no significant variation.

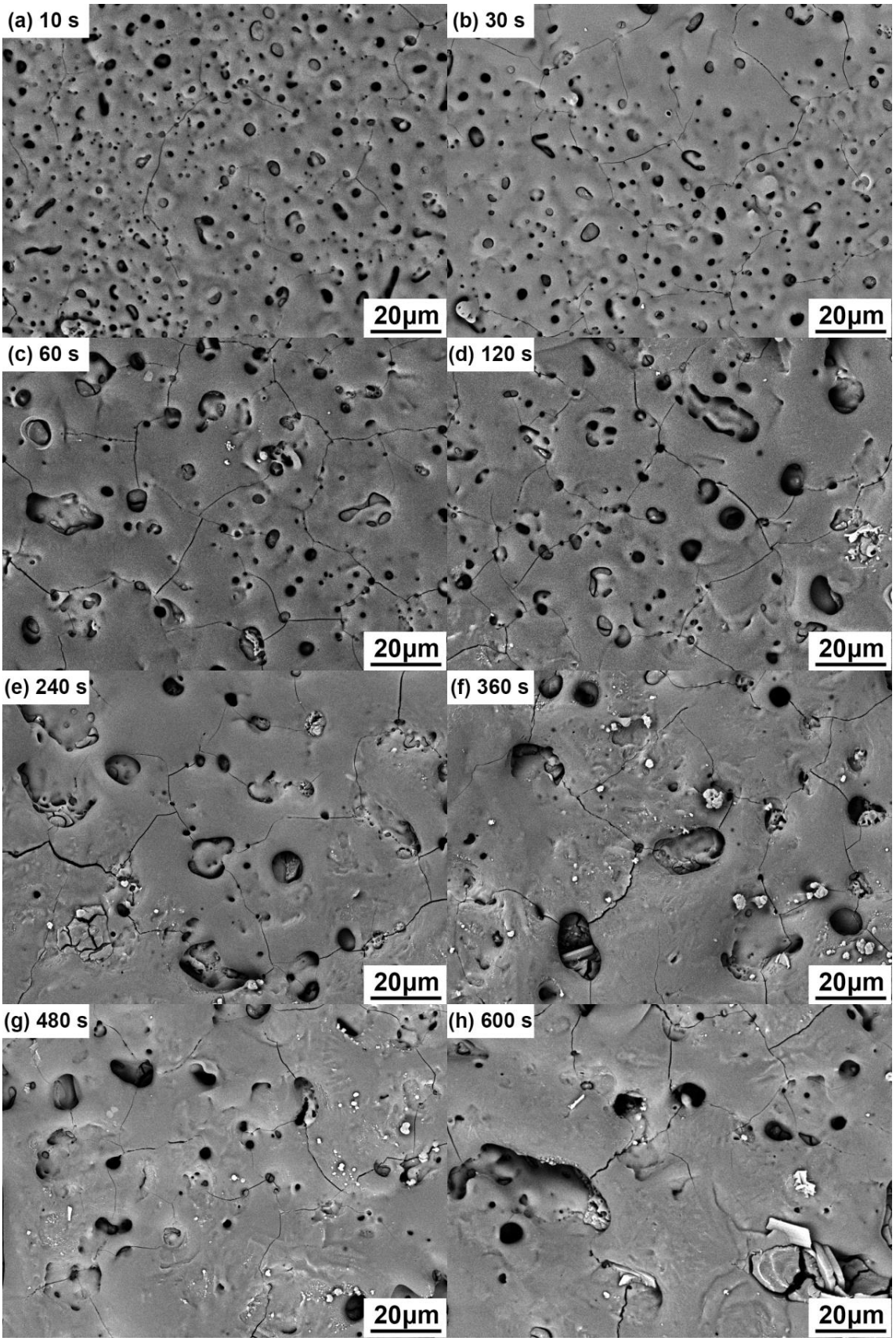

Fig. 5.5 SEM morphologies showing free surfaces of PEO coatings produced on AM50 with different treatment times.

Table 5.2 The number of pores and pore coverage ratios on the surfaces with an area of 1.2×10^4 μm^2 of PEO coatings produced at different treatment times

PEO time (s)	Pore number	Pore coverage (%)
10	258 ± 52	5.36 ± 0.55
30	181 ± 39	3.25 ± 0.52
60	108 ± 34	2.15 ± 0.39
120	89 ± 29	1.62 ± 0.43
240	66 ± 18	1.28 ± 0.49
360	55 ± 17	0.88 ± 0.45
480	42 ± 15	0.71 ± 0.56
600	27 ± 11	0.44 ± 0.42

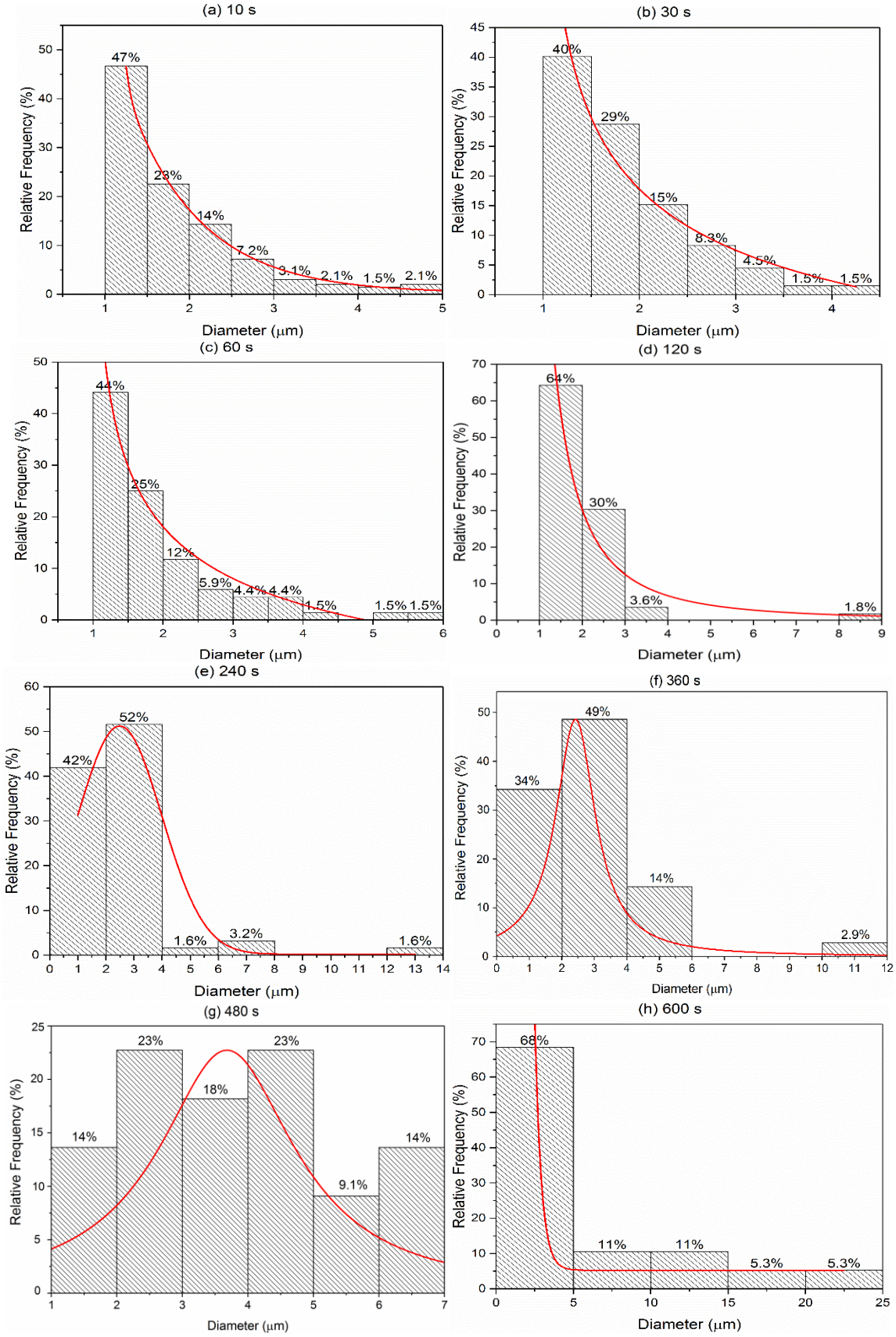

Fig. 5.6 Diameter distribution of the pores on PEO coating surfaces produced on AM50 with different treatment times.

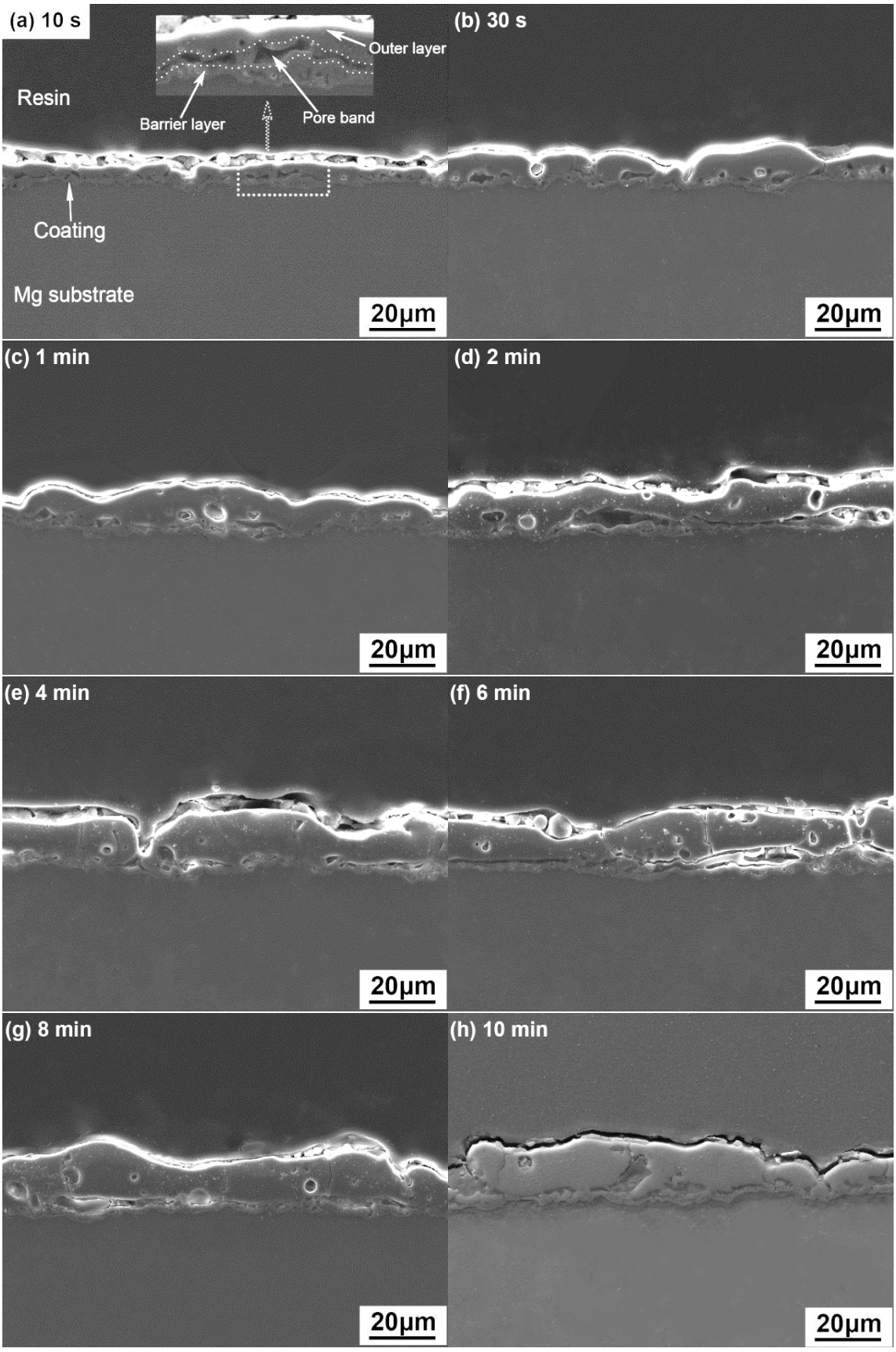

Fig. 5.7 SEM morphologies of the polished cross-sections of PEO coatings on AM50 for different treatment times.

5.1.5 Coating thickness

The changes of the average thickness of the whole coatings and barrier layers with PEO processing time measured from the cross-sections is shown in Fig.5.8. The total coating thickness, composed of a barrier layer, a pore band and an outer porous layer, increases with PEO processing time, especially in the initial stage up to 60 s when the fastest growth is observed. The coating growth rate decreases gradually over the whole PEO processing time, which is consistent with the decay of current density. On the other hand, it can be seen that after 10 s, the barrier layer has already been formed and its thickness reaches approximate 2 μm. At the same time, the total coating thickness is about 5 μm indicating that the barrier layer forms in a relatively short period of time and then the thickness of the barrier layer seems to be constant during the remaining PEO processing.

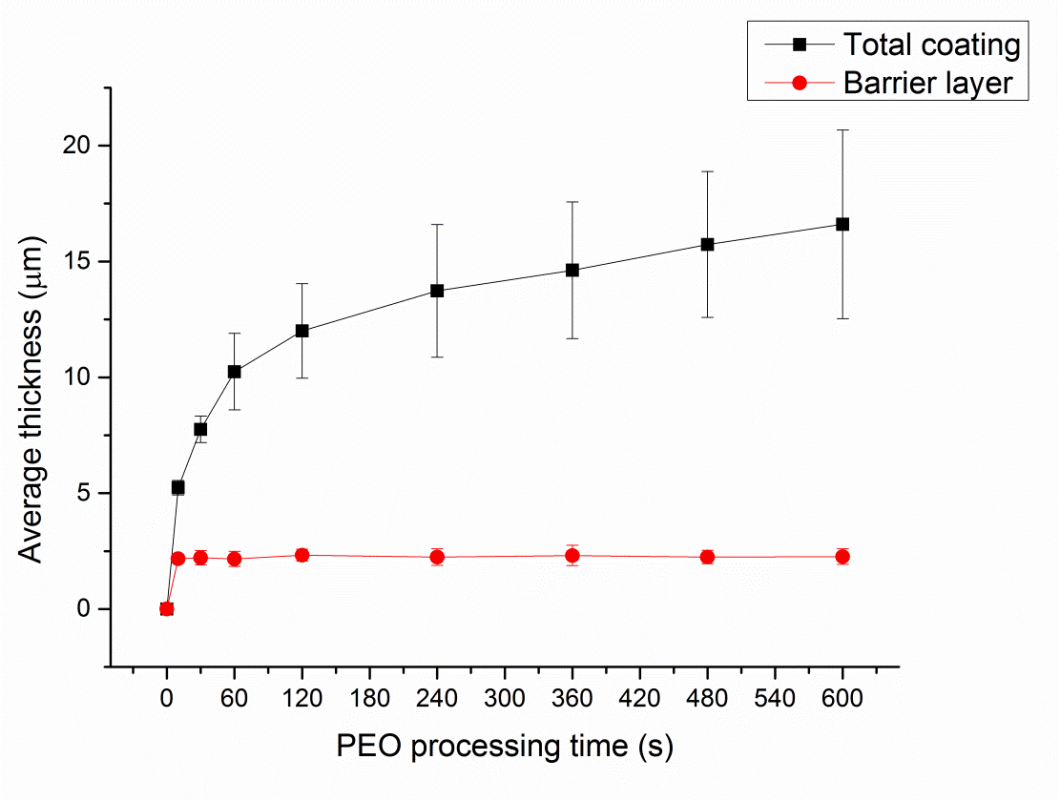

Fig. 5.8 Evolution of average thicknesses of total PEO coating and barrier layer with treatment time in 10 min with the error bars showing standard deviations.

5.1.6 Coating impedance

To get information on the resistance of the PEO coating to the electrolyte, EIS spectra were recorded during immersion in the same electrolyte that is used for the PEO process at the temperature of 10 °C for 30 min. Fig. 5.9 shows the electrochemical impedance spectra of the

PEO coatings after different treatment times. The symbols are the experimental data and the solid lines are fitting data. Some plots have only one time constant and some have two time constants. Therefore, two different equivalent circuit models used to fit the EIS of the PEO coated samples are shown in Fig. 5.10. In the circuits, R_s is the solution resistance, R_{f1} and CPE_{f1} represent the resistance and capacitance of the inner layer, and R_{f2} and CPE_{f2} stand for the resistance and capacitance of the outer layer. The resistance of the outer layer and the inner layer can be shown through the impedance with high frequency and the impedance with low frequency respectively. The inner layer provides higher resistance compared to the outer one. However, in order to assess the corrosion performance of the coating for different treatment times, the impedance at the lowest frequency (0.1 Hz) can be easily used to represent the total resistance of each coating [103]. Later on in the modelling, a parameter of the coating conductivity is needed to calculate the coating resistance. Even though the conductivity of the outer layer is different from the inner layer due to the different porosity in them, an effective conductivity of the total coating can be used considering all the contribution from both layers for comparison of different coatings. The effective conductivity of the coating can be calculated from the coating thickness and the coating resistance based on the equation below.

$$\sigma_{eff} = \frac{L}{R_f} \tag{5.2}$$

in which σ_{eff} is the effective conductivity, R_f is the low-frequency resistance measured form EIS, L is the coating thickness. The coating resistance, thickness, porosity and effective conductivity of the PEO-coated specimens after different treatment times are shown in Table 5.3. The results show that the coating resistance is enhanced by increasing treatment time and coating thickness, and the effective conductivity decreases with increasing time and thickness. The calculated effective conductivity of the PEO coating ranges from7e-8 S/m to 9e-7 S/m.

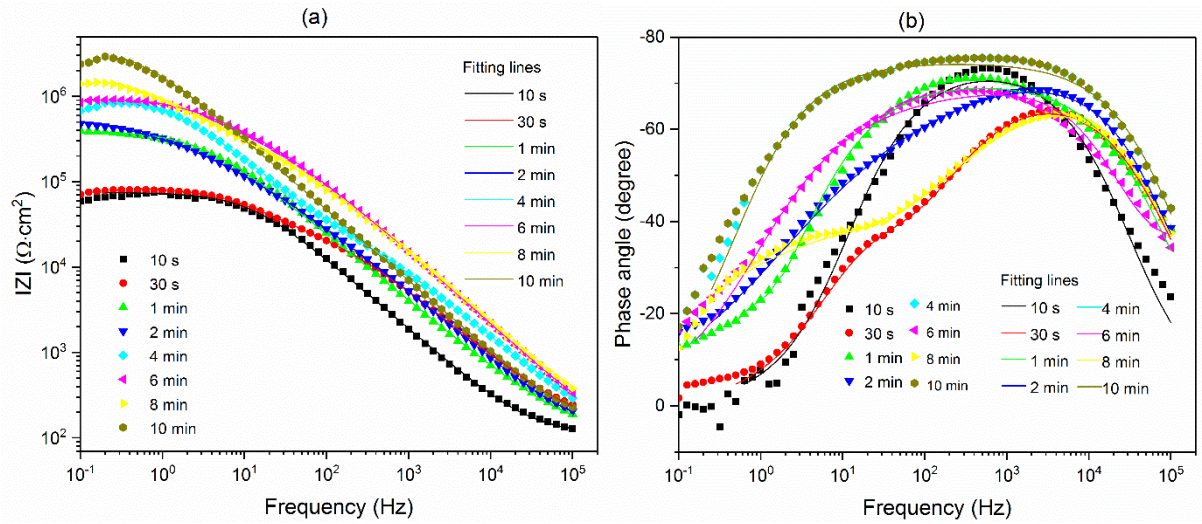

Fig. 5.9 Electrochemical impedance behavior of the coated substrates with different treatment times.

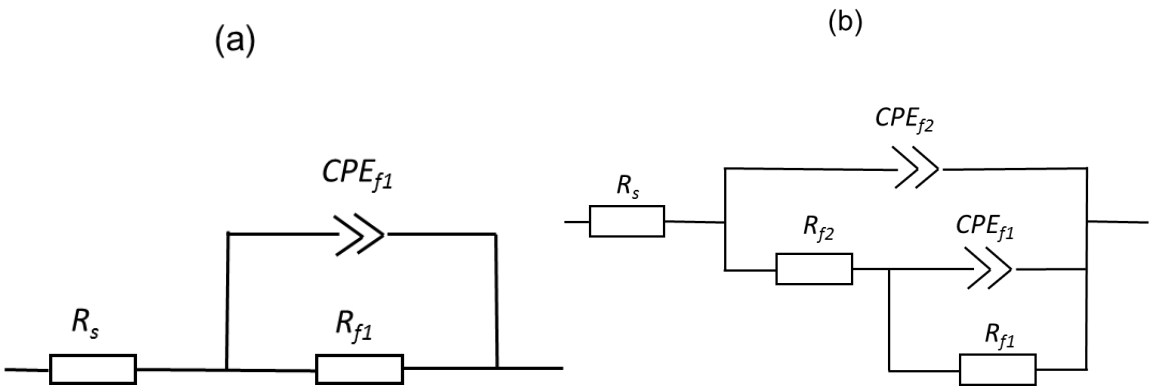

Fig. 5.10 Equivalent circuit models used for numerical fitting of PEO coatings treated for different times.

Table 5.3 Coating thickness, resistance and effective conductivity of the PEO-coated specimen after different treatment time.

Treatment time	Front coating thickness (μm)	Resistance ($\Omega \cdot cm^2$)	Effective conductivity (S/m)
10 s	5.23	6.1e4	9e−7
30 s	7.65	8.3e4	9e-7
1 min	10.24	3.9e5	3e-7
2 min	12	4.8e5	2.5e-7
4 min	13.73	6.8e5	2e-7
6 min	14.62	8.4e5	1.7e-7
8 min	15.73	1.4e6	1.1e-7
10 min	16.5	2.3e6	7e−8

5.2 Modelling and simulation of PEO coating growth

The PEO process is very complex due to its chemical, electrochemical, and plasma-chemical aspects that influence heat, mass and charge transfers. COMSOL is a modelling software that can solve multi-physics problems, which makes it an appropriate method to model complicated mechanisms underlying the PEO process. Based on the analysis of the time-dependent experimental results above, a mathematical model is developed to simulate PEO coating growth. This model describes a 2D transient finite element approach including necessary physical system parameters in mathematically coupled conditions. Electrochemistry module, chemical species transport module, and mathematics module in COMSOL were used to model the distribution of current density and growth of coating thickness under different experimental conditions, which may improve the understanding of the impacts of different parameters on PEO coatings.

The schematic representation of the experimental set-up was already shown in Fig. 3.2. In this study, the simulation model is simplified to a 2D model, as shown in Fig. 5.11(a). The 2D model considers only the X-Y plane, which is sufficient for describing the behavior of species and providing current distribution.

Even though the PEO process is complex, the growth of PEO films mainly follows electric field-assisted mechanisms [104]. According to Ref. [105], it is possible to consider a schematic of current distribution through the metal/oxide/electrolyte system during PEO treatment, as shown in Fig. 5.11(b). During the PEO processing, there are several processes consuming the total current. Due to the high resistance of the oxides, the anodizing current passing across the film is very low. Therefore, most of the current is mainly passing through the discharge channels. In the discharge channels, there are a component of the current I_c which contributes to the oxide layer formation and another component of current I_e which leads to the secondary processes in discharges and production of gases. An assumption for the coating formation is that the thickness can be calculated via Faraday's law and current efficiency [106]. The reported current efficiency applied to coating formation on Mg alloy is in the range of 30 % to 40 % [105] of the total current. According to the simplified equivalent circuit of PEO process for simple geometric shape proposed by Rakoch et al. [76], the electrochemical system under consideration is reduced to a simple model situation as shown in Fig. 5.11(c).

During PEO processing, three different types of plasma discharges have been proposed: metal/oxide interface discharge type (B) and oxide/electrolyte interface discharge types within the coating upper layer (A) and at the coating top layer (C) [107]. B type discharge is responsible for the ejection of molten alloys from the coating/substrate interface into the coating surface, while type A and C discharges are believed to excite the species from both substrate and electrolyte to react under conditions of high temperature and pressure which modify the coating morphology. When the electrolyte is sufficient, the growth of PEO coatings results only from molten Mg which is oxidized when flowing out through B type discharge [44]. On the other hand, in the study of discharges from Dunleavy et al [108], it is suggested that all PEO discharges develop according to the same physical mechanisms and the characteristics and duration of discharges show no significant influence on the coating thickness. Therefore, it is possible to assume one type of discharge in the model. Complementary, the basic assumptions for the modelling are as follows:

1. The energy loss from heat absorption by the environment is negligible.
2. The potential drops in the anode and the cathode were assumed to be negligible due to the good electrical conductive properties of magnesium alloy and stainless steel.
3. Only crystalline phases of MgO and $Mg_3(PO_4)_2$ are considered as the composition of the PEO coating.

4. Only B type discharge is considered in the modelling. The plasma discharges are assumed to be generated at the bottom of the pores and the length of the discharge channel is identical with the coating thickness. The current passing mainly through the discharge channels, and the decrease of the current over time results from the reduced discharge numbers.
5. At each time, the discharges break down at the weak points of the coating from the bottom and leave the discharge channels as the open pores inside the coating. The ceramic oxides formed later around the discharge channels will seal most of the open pores.
6. There are two parallel processes that consume the total current I: the current I_c contributes to the formation of the ceramic coating and the current I_e generates oxygen.
7. I_e does not contribute to the coating growth, but the heat generated by the plasma is high enough to convert the precipitation formed by Mg^{2+} and the anions in the electrolyte into ceramic phases in the coating.

To explain the current decrease, it is assumed that the current density j_p in a discharge channel stays constant, but the density of microplasma discharges decreases pronouncedly with time during a PEO treatment at a constant voltage [76].

$$I = j_p \cdot S_p \tag{5.3}$$

where S_p is the total surface area covered by discharge channels.

PEO coatings are known to be porous. The porosity of a PEO coating is assumed to result from the discharge channels. However, S_p is an on-changing variable because of the decreasing number of discharge channels with time, so the porosity can be described by the surface coverage of discharge channels at each moment instead of the bulk porosity. The coverage ratio can be calculated at any instant of time t by:

$$P = \frac{S_p}{S} \times 100\% \tag{5.4}$$

where S is the total anode surface area.

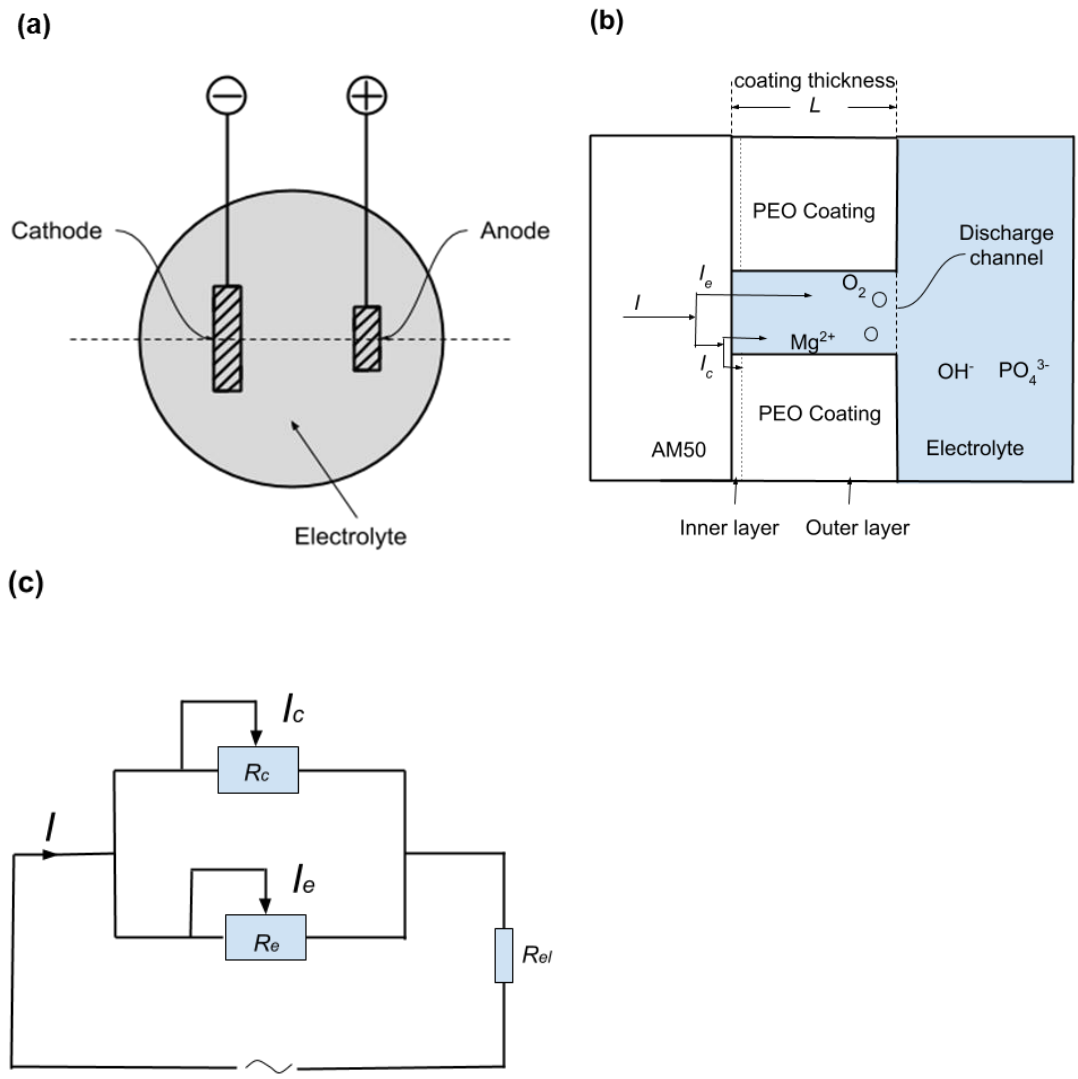

Fig. 5.11 (a) Model geometry used for computations; (b) Schematic diagram of current distribution during PEO treatment; (c) Equivalent circuit of PEO process: *Rel* is the resistance of electrolyte: *I* is the total current; *Ic* is the current contributing to coating formation; *Ie* is the current responsible for oxygen evolution; *Rc* and *Re* are the resistances corresponding to *Ic* and *Ie* respectively.

At the anode surface, in order to calculate the products formed during the PEO process in this model, it is necessary to know the reactions taking place at the substrate, as well as their kinetics. In the present study, the main reactions occurring on a Mg alloy surface in a phosphate-containing electrolyte during the PEO process are generally as follows:

- at the alloy/electrolyte interface

$$Mg \rightarrow Mg^{2+} + 2e^- \quad (5.5)$$

- in the discharge channel

$$4OH^- \rightarrow O_2\uparrow + 2H_2O + 4e^- \quad (5.6)$$

- at the coating/electrolyte interface

$$3Mg^{2+} + 2PO_4^{3-} \rightarrow Mg_3(PO_4)_2 \quad (5.7)$$

$$Mg^{2+} + 2OH^- \rightarrow MgO + H_2O \quad (5.8)$$

Eqs. (5.5) and (5.6) represent the electrochemical reactions during PEO process. Eq. (5.5) describes the dissolution of magnesium alloy and Eq. (5.6) describes the oxygen release under the effect of the electric field. I_c represents the current of magnesium oxidation, which corresponds to the electrode kinetics of Eq. (5.5), and I_e is the current responsible for oxygen evolution, which describes the electrode kinetics of Eq. (5.6). Eqs. (5.7) and (5.8) are considered as chemical reactions which contribute to the phase formation of PEO coating on AM50 surfaces. The process of PEO coating formation can be simplified as a two-step process. The first step is formation of Mg^{2+} and then the outward migration of Mg^{2+} and inward migration of PO_4^{3-} and OH^- under the effect of a high potential, and the second step is film formation taking place at the coating/electrolyte interface when the concentrations of those ions reach the solubility limit [104]. Therefore, this model setup is based on those two steps. Firstly, it intends to describe the electrochemical reactions taking place under an electrical field at the interfaces of the anode and electrolyte by secondary current distribution and transport of diluted species according to Eqs. (5.5) - (5.6). The second step tries to simulate the formation of coating phases and coating growths by surface reaction according to Eqs. (5.7) - (5.8).

At any instant of time t, according to the assumption, the whole current I at the anode can be described by:

$$I = I_c + I_e = j_c \cdot S_c + j_e \cdot S_p \quad (5.9)$$

The anode surface area can also be divided into two terms:

$$S = S_c + S_p \quad (5.10)$$

where S_c is the effective surface area of defect free coating. The area of gas formation is equal to the discharge area S_p.

A model developed by Pyun and Hong [97] can be applied to describe the evolution of current density j_c with coating thickness at each second during PEO processing. They developed a modified point defect model which involves formation, diffusion and transport of metal and oxygen vacancies to describe the growth kinetics of passive film prepared under potentiostatic

conditions, and the calculated relationship between the film thickness and time for films on iron and nickel were in accordance with those values obtained experimentally. Derived from this model, a theoretical equation which introduces a relationship between the current density j_c contributing to the substrate dissolution and the film thickness L is expressed by the equation below:

$$j_c = \frac{A(e^{vKL} - B \cdot e^{-vKL})}{e^{vKL} - 1} \tag{5.11}$$

It is assumed that the current density j_c contributing to the coating formation equals to 35% of total current density j. Here, v is the charge number of Mg^{2+}, and A, B and K are constants for a certain experiment and are determined by the polynomial least-squares procedure with 35% of the current density evolution examined experimentally in Fig. 5.1.

For each species i in the electrolyte, the general material balance takes into account diffusion, migration, and convection and can be described by Eq. (5.12):

$$\frac{\delta c_i}{\delta t} + \nabla(-D_i \nabla c_i - z_i \mu_i F c_i \nabla \varphi_i) + \mathbf{u} \nabla c_i = R_i \tag{5.12}$$

where F is Faraday constant, c_i is the concentration, D_i is the diffusion coefficient, z_i is the charge number of the ionic species, φ_i denotes the electric potential, R_i is the chemical reaction rate, and $\mathbf{u}$ is the fluid flow vector. According to the Einstein relation, μ_i is related to the diffusivity:

$$\mu_i = \frac{D_i}{R_{gas} T} \tag{5.13}$$

where R_{gas} is the universal gas constant, T is ambient temperature. The values for diffusion coefficients [109-111], initial concentrations C_o and charge numbers of the species involved in the electrolyte for simulation are shown in Table 5.4.

The concentration of the electrolyte at the anode boundary is equal to the bulk concentration because of the assumption of a supporting electrolyte with negligible concentration gradients:

$$c_i = c_{b,i} \tag{5.14}$$

According to Faraday's law, the reaction rate at the electrode surface for species in Eqs. (5.5)-(5.6) is calculated by:

$$R_i = \frac{v_i \cdot j_{c/e}}{F \cdot n_i} \tag{5.15}$$

here v_i is the stoichiometric coefficient and n_i is the number of electrons exchanged in the formation reaction.

Table 5.4. Diffusion coefficients (D), initial concentrations (C_o) and charge numbers (z) of the species involved in the electrolyte for simulation

Species	D (e-9 m^2/s)	C_0 (mol/m^3)	z	Reference
Mg^{2+}	0.71	0	2	109
PO_4^{3-}	0.37	183	-3	110
OH^-	5.3	29.2	-1	109
H^+	9.3	1e-10	1	109
Na^+	1.3	61	1	109
K^+	2.1	17.8	1	111
O_2	2.4	0.233	0	109

In the electrolyte, the model considers self-dissociation of water according to the reaction:

$$H_2O \rightleftarrows H^+ + OH^- \tag{5.16}$$

According to [99], the pH value of the electrolyte is calculated according to the concentration of H^+ (mol/m3):

$$\mathrm{pH} = -\log(10^{-3} \cdot c_{\mathrm{H}^+}) \tag{5.17}$$

The average current density j measured experimentally and shown in Fig. 5.1 is expressed by Eq. (5.1). The electric current in an electrolyte is equivalent to the transport of ionic species, so the current density j can be described by Faraday's law:

$$j = F \sum z_i N_i \tag{5.18}$$

For the net ionic charge transport, the assumption for this model is electroneutrality and a supporting electrolyte with negligible concentration gradients, so the convection term and diffusion term can be neglected and migration is dominating:

$$N_i = -z_i \mu_i F c_i \nabla \varphi_i \tag{5.19}$$

The conservation of electric charge is obtained through the divergence of the current density:

$$\nabla \cdot \mathrm{j} = 0 \tag{5.20}$$

The boundary condition at the anode is expressed by the electric potential:

$$\varphi_s = U \tag{5.21}$$

and for the cathode the electrolyte potential is:

$$\varphi_l = 0 \tag{5.22}$$

For all the insulation walls, there is no current flow. The boundary condition can be expressed as:

$$-\mathbf{n} \cdot \mathbf{j} = 0 \tag{5.23}$$

For the surface reaction, we assume that all the magnesium ions participate in the formation of PEO coating. Here only a one-dimensional growth of PEO coating in the perpendicular direction of the surface is considered. The PEO coating includes the growth of barrier layer in the first second and the growth of the outer layer from then to the end. The main phase of the barrier layer is MgO, so in the first second, the reaction rate and the growth rate of MgO are as follows:

$$R_{\mathrm{MgO}} = R_{\mathrm{Mg^{2+}}} \tag{5.24}$$

$$v_{\mathrm{MgO}} = \frac{R_{\mathrm{MgO}} \cdot M_{\mathrm{MgO}}}{\rho_{\mathrm{MgO}}} \tag{5.25}$$

where M_{MgO} is the molar mass and ρ_{MgO} is the density of MgO phase in the coating.

From 1 s to 600 s, the reaction rate of the main phase $Mg_3(PO_4)_2$ is calculated by:

$$R_{\mathrm{MgP}} = \frac{R_{\mathrm{Mg^{2+}}}}{3} \tag{5.26}$$

Accordingly, the growth rate v_{MgP} for the outer layer is determined by the $Mg_3(PO_4)_2$ phase and the porosity:

$$v_{\mathrm{MgP}} = \frac{R_{\mathrm{Mg3(PO4)2}} \cdot M_{\mathrm{Mg3(PO4)2}}}{(1-P) \cdot \rho_{\mathrm{Mg3(PO4)2}}} \tag{5.27}$$

where $\mathrm{M_{Mg3(PO4)2}}$ is the molar mass and $\rho_{\mathrm{Mg3(PO4)2}}$ is the density of $Mg_3(PO_4)_2$ phase in the coating.

The pH value of the electrolyte is in the passive region of AM50 magnesium alloy, so a natural passive film would be formed when the magnesium electrode is immersed in the electrolyte.

In this manner, it is assumed that the substrate has a thin magnesium oxide layer L_0, and the total coating thickness L can be calculated by:

$$L = L_0 + \int_0^1 v_{\mathrm{MgO}}\, \mathrm{d}t + \int_1^t v_{\mathrm{MgP}}\, \mathrm{d}t \tag{5.28}$$

The efficiency of coating formation E_{ff} is evaluated from the coating formation charge and the total anodic charge:

$$E_{ff} = \frac{\int_0^t j_c \cdot S_c \ \mathrm{d}t}{\int_0^t j \cdot S \ \mathrm{d}t} \tag{5.29}$$

The coating resistance to the solution during EIS test can be calculated by the coating thickness and the effective conductivity measured form experiments:

$$R_f = \frac{L}{\sigma_{eff} \cdot S} \tag{5.30}$$

where L is the coating thickness, σ_{eff} is the effective conductivity.

Table 5.5 and Table 5.6 summarizes the most important parameters being used for the computation. Combining all the parameters in Table 5.4, Table 5.5 and Table 5.6, with the respective boundary conditions, the model is solved numerically via finite element method for time-dependent study in 10 min with a time stepping of 1 s using the commercial software COMSOL Multiphysics (version 4.4).

Table 5.5. Physical input parameters measured from experiments for numerical simulation

Physical parameter	Value	Unit
T	283.15	K
U	350	V
S	6.3	cm^2
σ_{el}	1.4	S/m
σ_{eff}	7e-9 or 8e-7	S/m
A	1.6e-3	A/cm^2
B	122	-
K	7.5e4	1/m

Table 5.6 Physical input parameters used for numerical simulation

$M_{Mg3(PO4)2}$	262.9	g/mol
$\rho_{Mg3(PO4)2}$	2.2	g/cm^3
M_{MgO}	40.3	g/mol
ρ_{MgO}	3.58	g/cm^3
j_p	3.0	A/cm^2
L_0	1e-6	m

5.3 Simulation results and discussion

The modelling can output values about current density, pore coverage ratio, the changes of electrolyte, coating thickness, and coating formation efficiency. Based on the coating thickness, pore coverage ratio and the effective conductivity of the electrolyte in the pores, the coating resistance can also be revealed. Fig. 5.12 shows the evolution of total current density and current density directly contributing to the coating growth and their corresponding fitting curves calculated from the model for a period of 10 min. At potentiostatic condition, the total current density on the anode decreases rapidly within several seconds after the voltage is applied. It is already reduced to 10% of its initial value in 10 s, which is caused by the PEO coating formation and its relatively high ohmic film resistance. Afterwards, the current density decreases slowly over the remaining PEO treatment time. The current density contributing to coating formation, has a similar decay transient compared to the total anode current density, which indicates the correctness of applying the model of Pyun and Hong [97] to describe the kinetics of coating formation. The current density contributing to coating formation remains lower than that of the total anode current density. The difference between total anode current density and coating formation current density contributes to plasma discharges according to the assumption above.

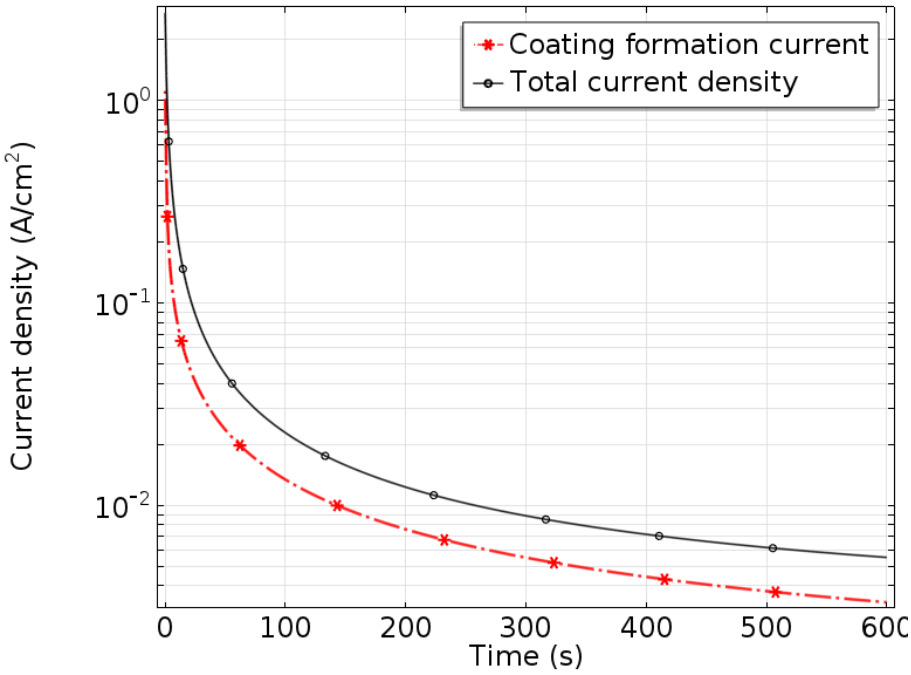

Fig.5.12 The evolution of total anode current density and the average current density contributing to the coating growth vs time calculated from the model over 10 min.

In Fig. 5.13, the experimental and simulation results of coverage ratio of discharge channels on the PEO coating surface as a function of time are shown. The simulation results are calculated according to Eq. (5.4). The experimental results show a decreasing pore coverage ratio over the treatment time. The highest pore coverage ratio is about 5% when the treatment time is 10 s, while the minimum value is 0.44% at 600 s. However, these results can not represent the porosity of the coating since it is only surface-connected. The porosity calculated based on coating density was determined to be less than 5% [57] demonstrating that porosity is only a small fraction in PEO coating. Still, the results of coverage ratio of discharge channels can reflect the trend of discharges over time during PEO process. The simulation results show that the coverage ratio is obviously high at the early stage of the PEO process, corresponding to the sparks flashing all over the specimen surface. As expected, the coverage ratio then drops down with PEO treatment time, indicating that the number of discharges gets less. In [112], a decreasing number of sparks over time can also be observed experimentally by a video camera. Compared with the experimental results of pore coverage ratio, the simulation results of coverage ratio of discharge channels are smaller than the experimental results. On one hand, the pores generated from the discharge channels can not be sealed completely at once. With longer treatment time, the pores left on the surface may result from discharge channels during a long period. On the other hand, the imprecise assumption of constant current density in the

discharge channels in the modelling and the deviation in measuring the pores from experimental images in the software can also lead to the difference between simulation results and experimental results of pores.

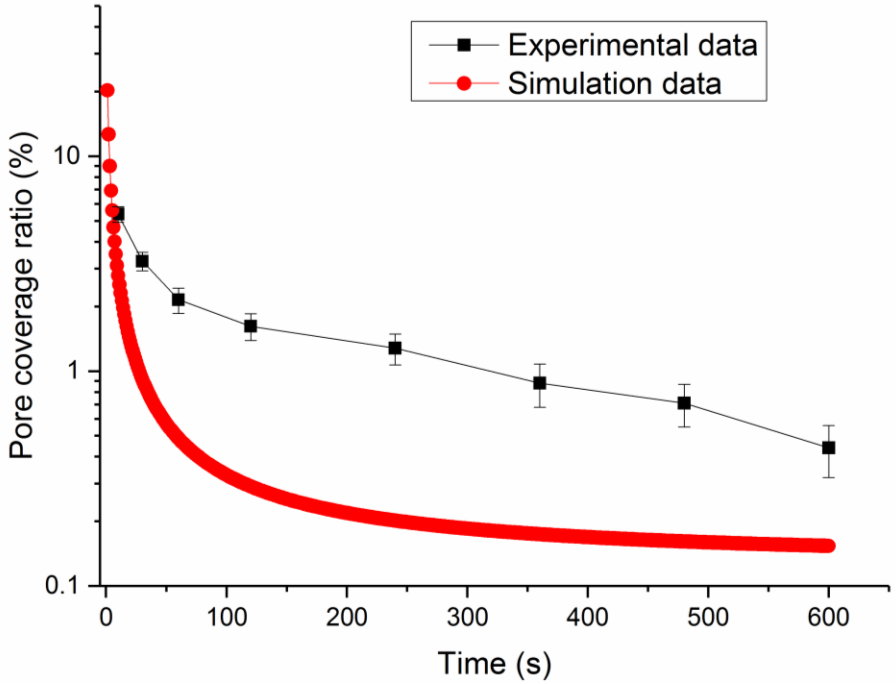

Fig.5.13 Simulation and experimental results of pore coverage ratio on PEO coating surface as a function of time.

Changes of the concentration of each species including Mg^{2+}, PO_4^{3-}, OH^- and O_2 at the interface during the treatment time are presented in Fig. 5.14. Here Mg^{2+} concentration is only for calculation purpose, which represents the amount of Mg^{2+} after electrochemical reaction of Eq. (5.4) rather than the final amount of concentration in the electrolyte. Mg^{2+} concentration increases due to the sustaining dissolution of magnesium substrate. The decrease of PO_4^{3-} concentration is a result of the formation of $Mg_3(PO_4)_2$ phase in the coating. OH^- is consumed by both oxygen release and the formation of MgO in the coating. It is clear that the changes of PO_4^{3-} and OH^- in the electrolyte are inconspicuous, so the electrolyte can be reutilized which demonstrates the economic efficiency and the environmentally friendly properties of the PEO processing. However, a higher amount of oxygen is formed during PEO process as can be seen by experimental observations [75,112]. The amount of OH^- can be determined by pH values measurement in the electrolyte.

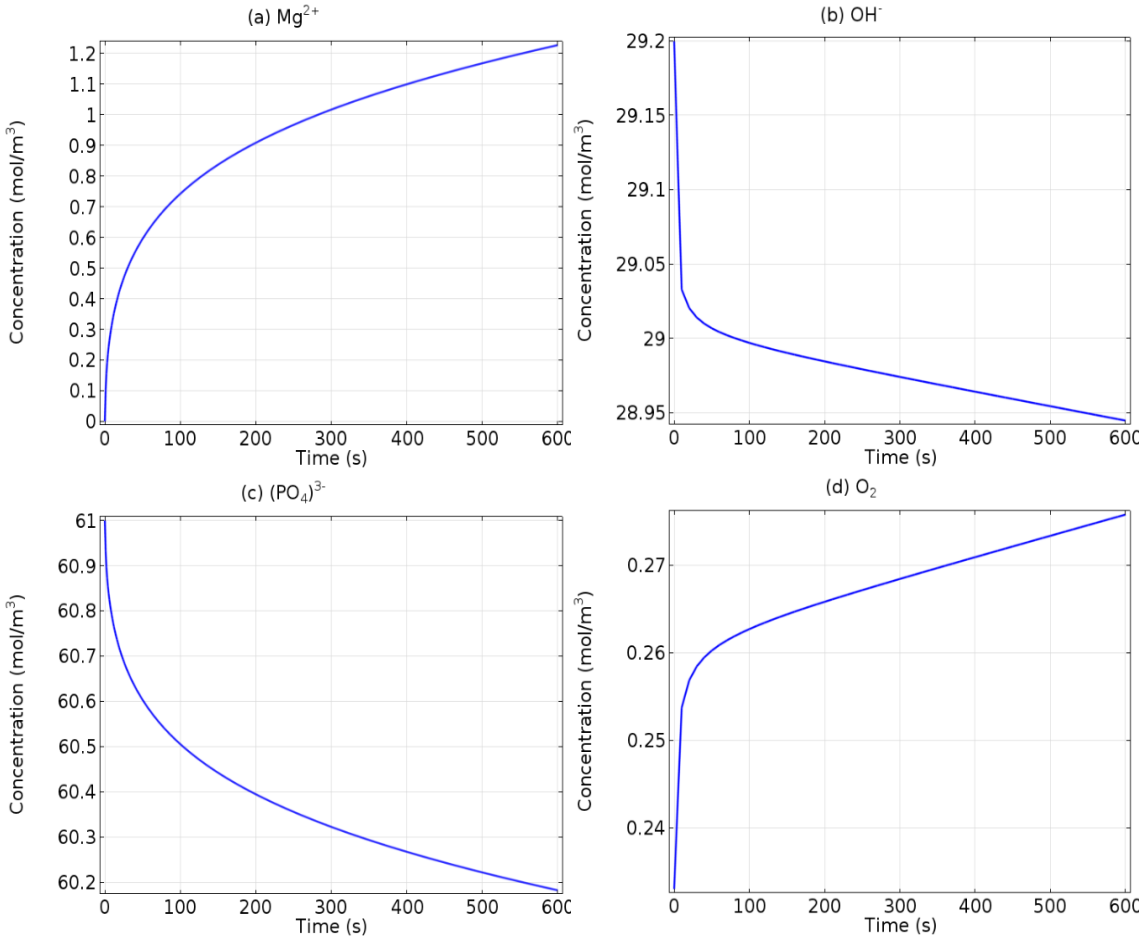

Fig. 5.14 Simulation result of changes of concentration of each species in electrolyte over time.

In Fig. 5.15, the calculated pH value in 10 min of PEO processing decreases by 0.007 only, but the value measured experimentally in the electrolyte decreases from 12.98 to 12.93 in 10 min. The inaccurate simulation results of OH^- and O_2 arise from the incomplete mechanisms of oxygen liberation and electrolyte acidification which are much more complicated and do not apply to Faraday's law. According to Ref. [113], Eq. (5.5) is valid only for pure electrochemical process which is not accompanied by a plasma discharge, and for the processes with discharge, anomalous oxygen liberation is caused exclusively by the discharge which initiates non-electrochemical processes. Therefore, the calculation for OH^- and O_2 concentrations are much less than those measured in the experiments.

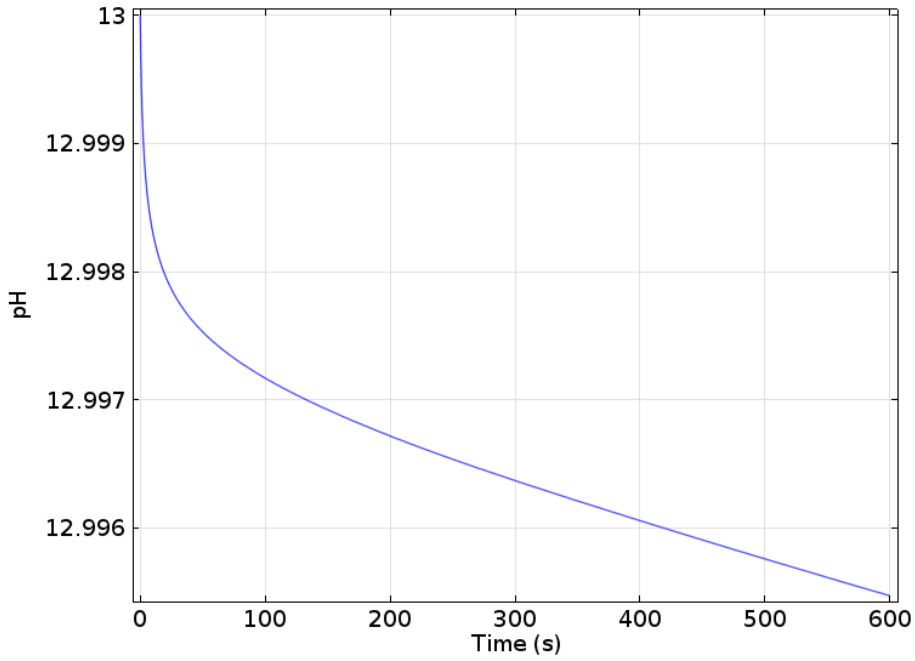

Fig. 5.15 The simulation results of changes of pH values of the electrolyte over time.

Fig. 5.16 shows the changes of average coating thickness vs. time calculated from modelling and experiments, assuming that all the Mg^{2+} ions contribute to the formation of PEO coating phases. In general, the coating thickness is determined by the charges passed through the coating, the phase formation and the porosity of the coating. It is found that the coating formation speed decreases over the whole treatment time mainly due to the decrease of current density under potentiostatic condition. In contrast, the porosity plays a minor role in affecting the coating growth rate. It is also revealed that the coating thickness increases rapidly within the very first seconds because of the high current density during the same period of time as seen in Fig.5.10, and then increases gradually corresponding to the low residual current density at longer treatment times. Finally, the values of the PEO coating thickness calculated by simulation are in good agreement with the experimental data considering the error bars.

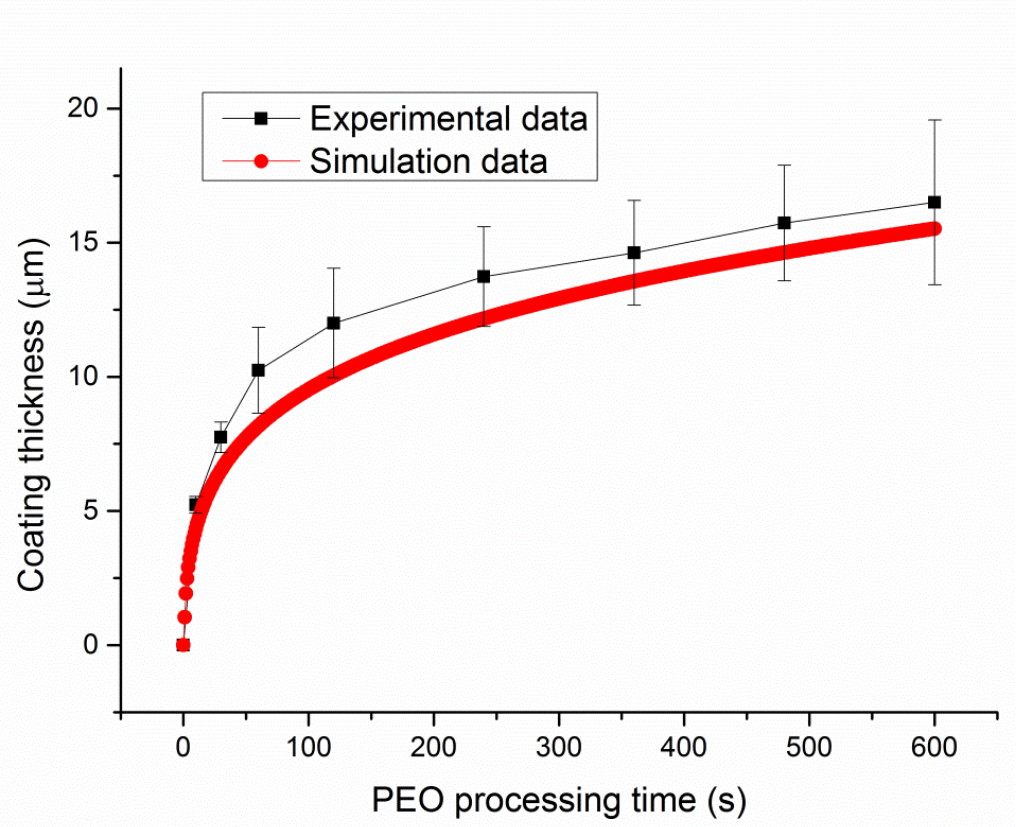

Fig.5. 16 Changes of average coating thickness with time calculated from modelling and experimental figures respectively in 10 min.

Evolution of anodic charge, coating formation charge (a) and coating formation efficiency (b) during PEO treatment for 10 min is depicted in Fig. 5.17. The anodic and coating formation charges increase quickly during the first 30 s and then slow down to the end. The difference between these two kinds of charges results from the charge consumed in discharge channels to create plasmas. The efficiency of coating formation is evaluated from the coating formation charge and the total anodic charge at each time. From 0 s to 10 min, the efficiency of PEO coating formation on AM50 alloy is in the range of 23% to 42%. At the beginning the efficiency is low and then increases gradually with time. This is related to the discharge behavior. In the beginning of the PEO processing, numerous discharges are produced and most energy is consumed by them so the coating formation efficiency is low. Then with increasing time, PEO coating thickens and fewer discharges were generated, so large amount of current contributes to coating formation and leads to increase of coating formation efficiency. In Ref. [30], the values of coating formation efficiency are also in accordance with the presented calculation result.

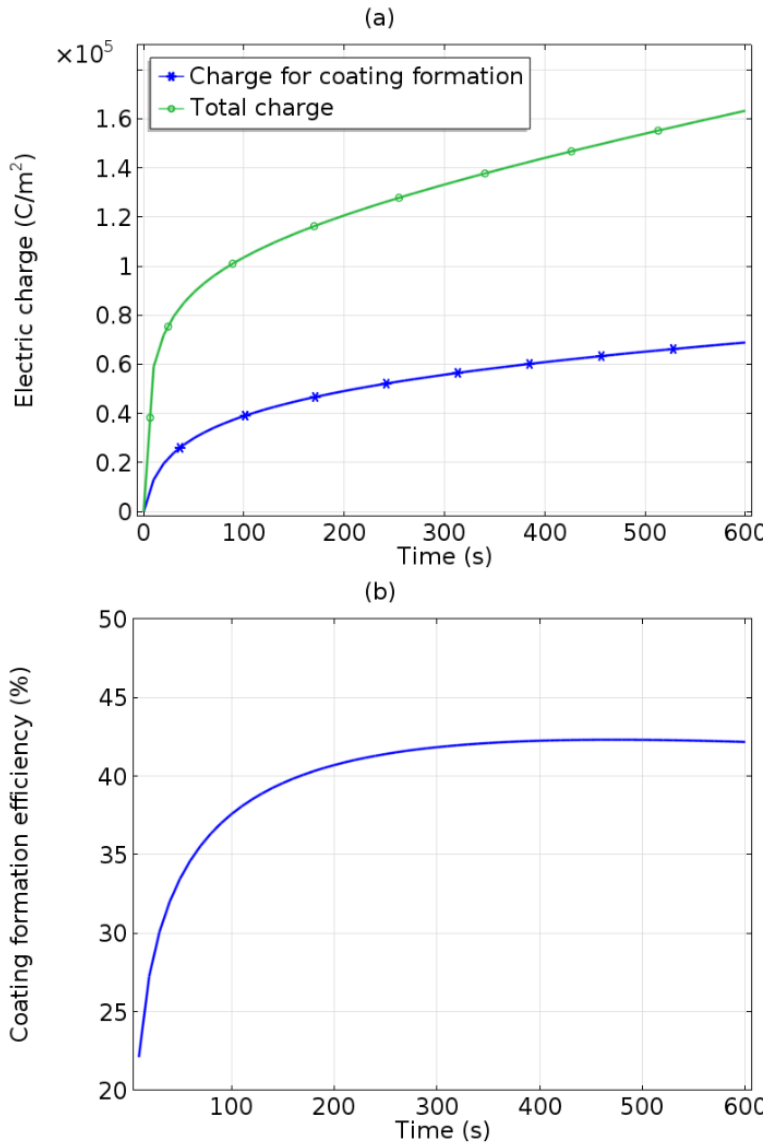

Fig. 5.17 Time dependence of anodic charge and coating formation charge (a) and coating formation efficiency (b) during PEO treatment in 10min.

In Fig. 5.18, the dependence of coating resistance during EIS measurement on time was revealed by the simulation results and the experimental values are shown at different times. The measured effective conductivity values of the PEO coatings at different time intervals are not consistent, but for the numerical calculation, a specific value has to be chosen. Therefore, the highest and lowest effective conductivities (9e-7 S/m and 7e-8 S/m) from the experiments were used respectively to show the difference between the final simulated coating resistances. The simulated coating resistances increase with time, and the experimental values are in between the simulated coating resistance with the high effective conductivity and the simulated resistances with the low effective conductivity. With the high effective conductivity, the coating resistance are in good agreement with the experimental values with treatment times

less than 4 min, but after 6 min, the simulated results are lower, compared to the experimental results. With the low effective conductivity, the simulated coating resistances are higher, compared to that with high effective conductivity and the simulated result is only close to the experimental results at 10 min. Because the effective conductivity is dependent on time and coating thickness, so it would be more accurate to calculate the resistance with the effective conductivity at different time.

Nevertheless, it is worth mention that the effective conductivity measured by EIS is not the same with that during PEO process because of different applied voltage. The effective conductivity of the coating can be much higher compared to that during EIS measurement due to the plasma discharges. Therefore, the simulated results here can only evaluate the resistance under electrochemical test rather than the coating resistance during PEO process.

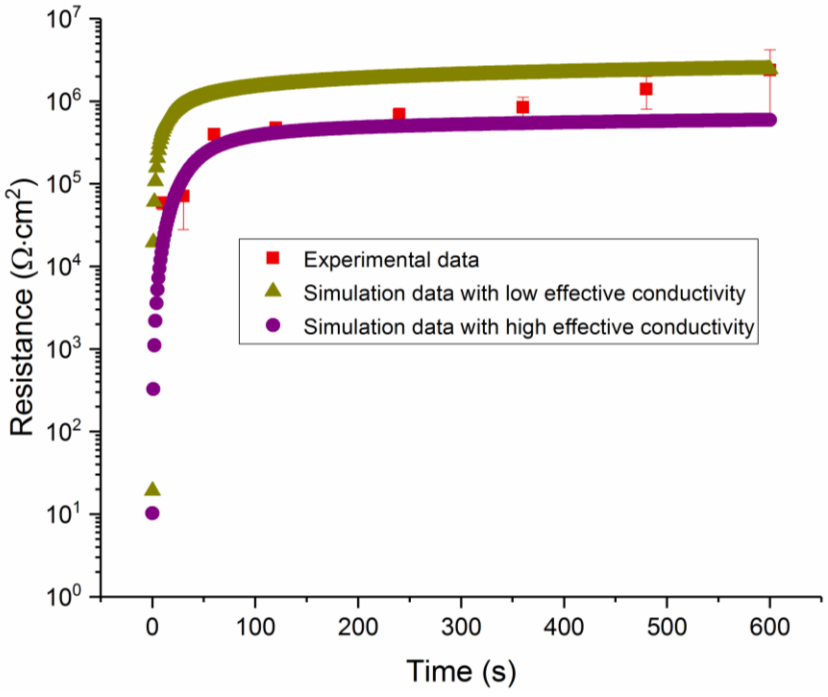

Fig. 5.18 The experimental and simulation results of the average resistance of PEO coatings vs. time.

5.4 Validation of the coating growth model under different voltages

It is also necessary to verify the PEO coating growth model when the power supply provides different voltage levels. When the voltage is lower than 240 V, there are no plasma discharges generated on the surface of the AM50 alloy. When the voltage exceeds 360V, the surface of the

AM50 alloy will be destroyed by permanent and stationary arcing. Therefore, the experimental study of the PEO coating under the voltages of 250 V and 300 V were performed in the same electrolyte for 10 min.

In Fig.5.19, the evolution of the current densities under constant voltages of 250 V and 300 V and their corresponding fitting curves are displayed. The current densities under voltage of 300 V are higher than that under voltage of 250 V. The fitting curves reveal the dependence of current density on PEO treatment time, and they can be expressed by the equations below separately:

For current densities under 250 V:

$$j(t) = 2.6344 - \frac{2.6339 \times t^{0.9}}{0.074 + t^{0.9}} \tag{5.31}$$

For current densities under 300 V:

$$j(t) = 2.9245 - \frac{2.9235 \times t^{0.92}}{0.12 + t^{0.92}} \tag{5.32}$$

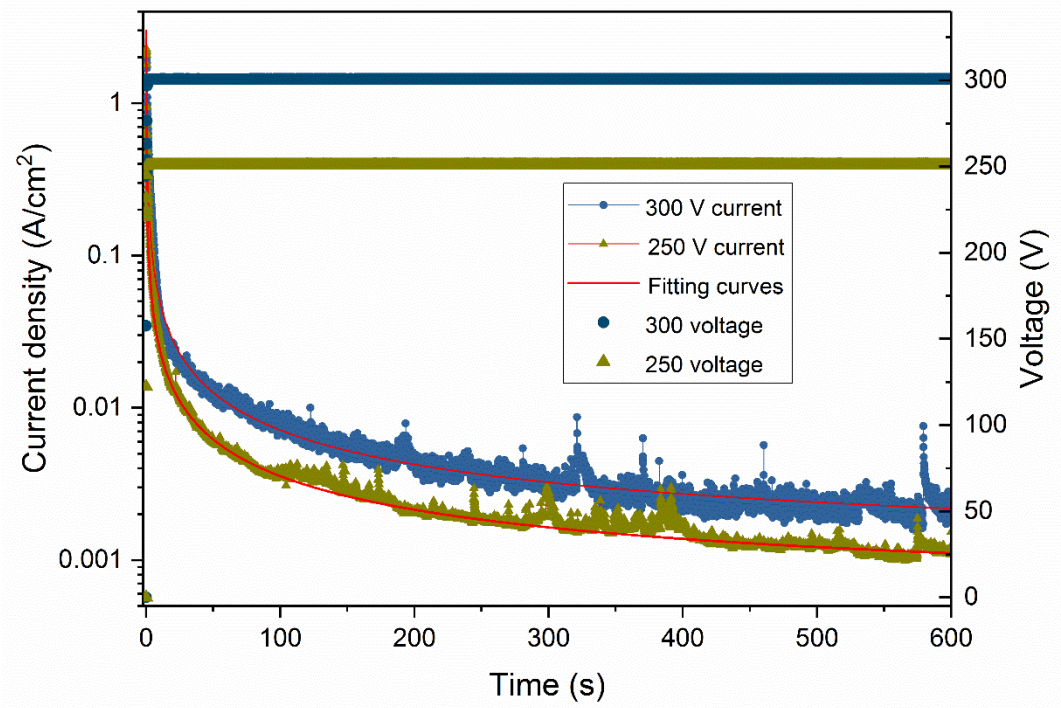

Fig. 5.19 The evolution of the current densities under constant voltages of 250 V and 300 V separately. The fitting curves in red are in good agreement with the experimental values of the current density.

After PEO treatment under different voltages for 10 min, the SEM morphologies of the coating surfaces are presented in Fig. 5.20. The coatings differ from each other tremendously. Under 250 V, the surface of the coating is covered by numerous tiny pores whose size of diameters are almost identical and smaller than 1 μm. Under 300 V, the pores are much bigger compared 250 V, and the size of the pores ranges from around 1 μm to more than 10 μm. Therefore, the higher the voltage, the larger the pores on the PEO coating surface.

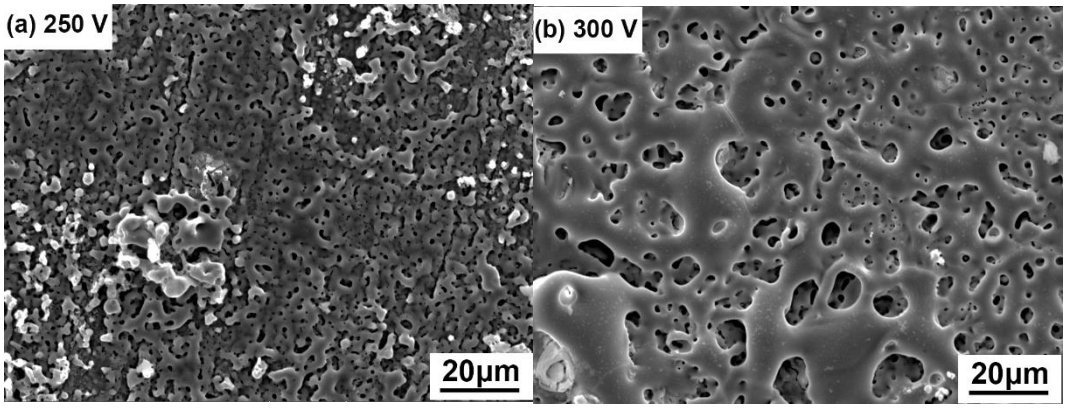

Fig. 5.20 SEM morphologies of PEO coatings on the flat surfaces of AM50 substrates under different voltages: (a) 250 V; (b) 300 V.

The corresponding cross-sections of the PEO coatings under different voltages are shown in Fig. 5.21. The cross-section under 250 V is very thin and pores are barely can be seen. The thickness of the coating under 250 V is approx. 1.8 μm. The cross-section under 300 V is thicker than that under 250 V and its thickness is around 4.5 μm. The general features of the three-layer structure, namely the barrier layer, the pore band and the porous layer can also be seen in the SEM morphology of the cross-section under 300 V.

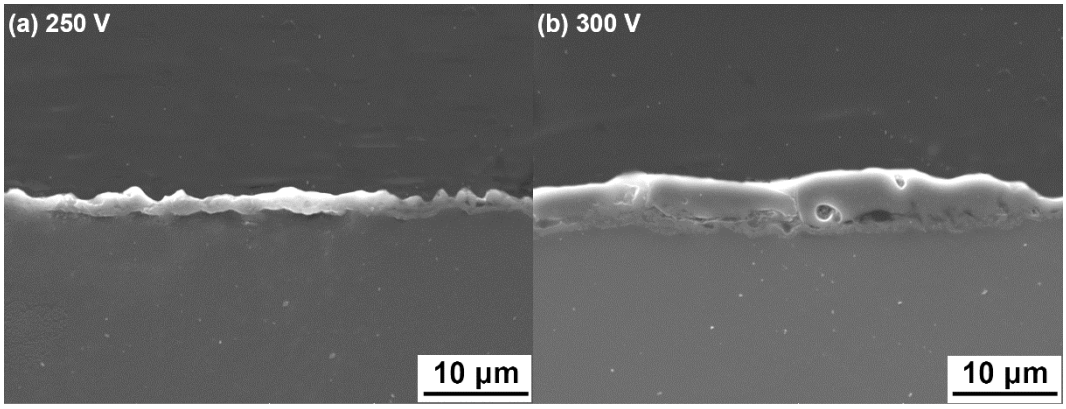

Fig. 5.21 SEM morphologies of the polished cross-sections of PEO coating under different voltages: (a) 250 V; (b) 300 V.

According to the modelling process in section 5.2, the coating thickness under different voltages can be calculated with their corresponding current density input by the same routine. The different values of some parameters used for each voltage are listed in Table 5.7. A, B, K values for each condition can be obtained by fitting Eq. (5.9) with 35% of the corresponding current density values.

The final simulation results of the coating thickness evolution under different voltages are shown in Fig. 5.22 and compared with the experimental values of coating thicknesses at 10 min. With higher voltage of 300 V, the coating thickness increases quicker than that with the lower voltage of 250 V. The simulated coating thicknesses at 10 min are 2.1 μm and 4.3 μm for 250 V and 300 V separately. Compared with the experimental results of coating thickness at 10 min, the simulation results are within the range of the errors, which demonstrates the correctness of the modelling.

Table 5.7 Parameters used in the numerical simulation under different applied voltages

U	A (A/cm^2)	B	K(1/m)
250 V	5.8e-4	246	5e5
300 V	5.9e-4	292	1.43e5

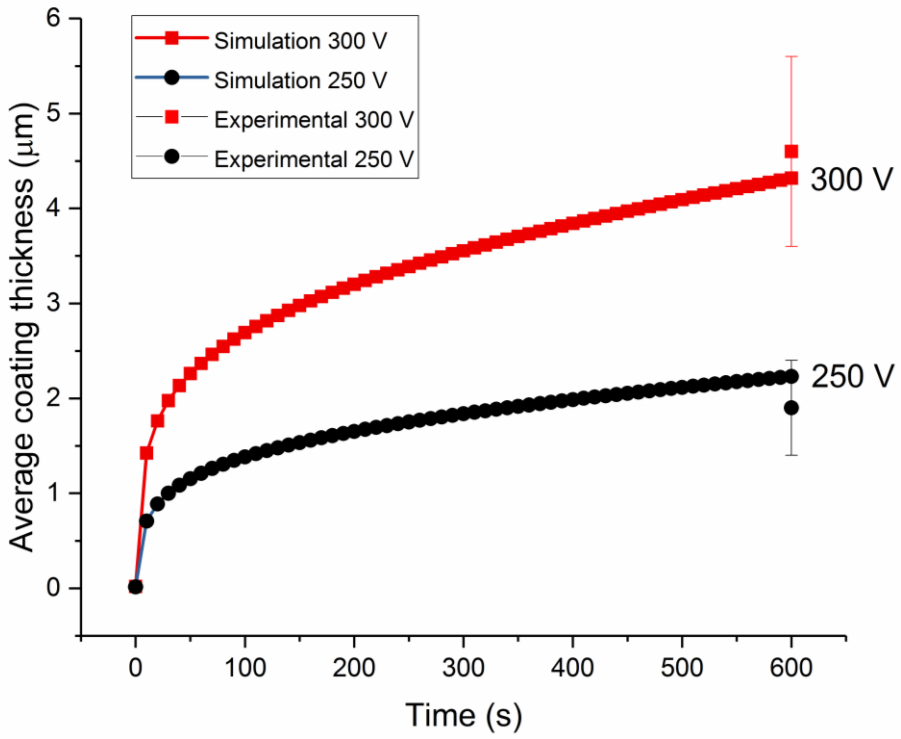

Fig.5.22 Changes of average coating thickness with time calculated from modelling in 10 min and the experimental values of coating thicknesses at 10 min under different voltages.

5.5 Summary

In summary, we have studied experimentally the time dependent evolution of composition, morphology, and thickness of PEO coatings obtained on the surface of AM50 alloy under constant DC voltage mode, and based on those data, a model has been developed to simulate the PEO process. Comparing the simulation results with the experimental results, the following conclusions can be drawn:

1. The growth of PEO coating is revealed by the evolution of composition, morphology and thickness of PEO coating with time from 10 s to 10 min experimentally. The PEO coatings are composed of crystalline MgO and $Mg_3(PO_4)_2$. MgO is formed in the initial stage and $Mg_3(PO_4)_2$ is mainly formed in the later stage of the PEO process. The number of pores formed by the discharges on the coating surface decreases with time and the coating thickness increases with the treatment time. Also, the experimental study provides important information and useful data input for the time dependent modeling and simulation of the PEO process.

2. A model is successfully built based on the current mechanisms and assumptions of the PEO process proposed in the literature. The mechanism of PEO includes the growth of the coating and the evolution of the discharges. Anodic current density is divided into coating formation current density and discharge current density to describe the kinetics respectively. The current density contributing to coating formation j_c is described by the modified point defect model and the discharge current density j_p is assumed to be constant. Faraday' law is used to calculate the coating thickness, while the current density generating the discharges does not contribute to the coating thickness.
3. According to the modelling, the average coating thickness is a function of coating formation current density, phase composition and coating porosity. Among them, coating formation current density is the most important factor when the phase composition is known to be MgO and $Mg_3(PO_4)_2$. The simulation result of the average coating thickness evolution over time is in good agreement with experimental values, which confirms the validity of applying Faraday' law and the modified point defect model in describing the coating growth kinetics for PEO process in spite of the presence of discharges.

4. The current efficiency calculated from modelling ranges from 23% to 42% during a PEO processing time of 10 min. It is changing over time, and with longer time, the current efficiency may increase because less current is consumed by discharges.
5. The simulated pore coverage ratio on the surface of the PEO coating can be correlated and estimated by the number and area of pores on the coating surface. Even though the simulated results are lower than the experimental data, the same evolution tendency may indicate the correctness of the model concept. The coating resistance can be calculated from the coating thickness, pore coverage and effectivity conductivity in the pores. The simulation results are quite close to the experimental values except that with longer treatment time. However, more effect are still needed in order to predict the pores and thus the resistance of the PEO coatings for further study.
6. The PEO coating growth modelling is also verified by applying different voltages of 250 V and 300 V. The simulated coating thicknesses are in good agreement with the experimental values.
7. The drawback of this model is that it cannot predict the results of pore coverage ratio, oxygen release and pH values of the electrolyte close to the experimental result because the kinetics for non-electrochemical reaction induced by discharges in PEO process is still not clear.

Summarizing, the simulations reproduce this simple potentiostatic PEO process on AM50 reasonably well and provide useful information on calculating coating thickness and explaining physical phenomena of discharges. The simulation results are in good agreement with experimental results, especially for predicted coating thicknesses. Although the model has a drawback in describing the oxygen release and hydroxyl ion concentration due to an empirical kinetic description, it may still be a useful tool in explaining and predicting PEO coating growth on magnesium alloy under constant DC voltage.

6. Investigation of electrode distance impact on PEO coating formation assisted by simulation

For decades, various researchers have investigated the formation mechanisms and parameters influencing the PEO process to optimize the treatment parameters for the purpose of improving the coating properties [114-124]. Parameters such as electrolyte compositions, substrate materials, the electric parameters (mainly voltage mode, current mode and current density), and process time were studied as well as their impact on coating morphologies and properties. Among all the parameters, current density was considered as the principal parameter [123,124], but the electrode distance between anode and cathode was deemed negligible and only a few papers studied its influence. Melhem et al. [125] suggested that distance can play a role, depending on the process conditions, and should nonetheless be taken into account. Also, Wei et al. [126] demonstrated that the distance between anode and cathode affected the anodic current and the oxidation efficiency. Therefore, the distance effect has to be considered.

Since experiments do not offer direct access to the current distribution, especially at the sample surface, the task can be accomplished numerically by modeling and simulation. The complexity of the nonuniform electrical field strength in the electrolyte can be studied by finite element analysis provided by COMSOL Multiphysics software through both stationary model and time-dependent model. Thus, PEO coatings will be produced with different electrode distances ranging from 10 mm to 240 mm under a constant voltage mode. The coating features including phase compositions, surface and cross-section morphologies and coating thicknesses will be determined as a function of the electrode distance. Combined with the complementary result of current density distribution and coating thickness simulated via the numerical models, the effect of electrode distance on anode current and PEO coating formation on AM50 magnesium alloy will be discussed.

6.1 Experimental results

6.1.1 Current density

For the whole PEO process, the experimental evaluation of current density is depicted in Fig. 6.1. The current increased rapidly in 1 second after the voltage was turned on, and then decreased during the rest of the processing time while the voltage was kept constant. As can be seen, there is not much influence of electrode distance on the current density evolution with

time except in the first 20 s. The current density reaches the maximum at the very first and then decreases dynamically within 10 s followed by a relatively slow decline. The current density is recorded every one second, so the current density at the first second is considered as the initial current, which gets lower when the electrode distance is increasing. By the end of the processing time, the current density value drops to approx. 0.02 A for all the coatings. Evidently, the influence of electrode distance on the anode current density can be seen only in the initial stage of treatment ($\leq$ 20 s). Afterwards, the influence becomes weaker.

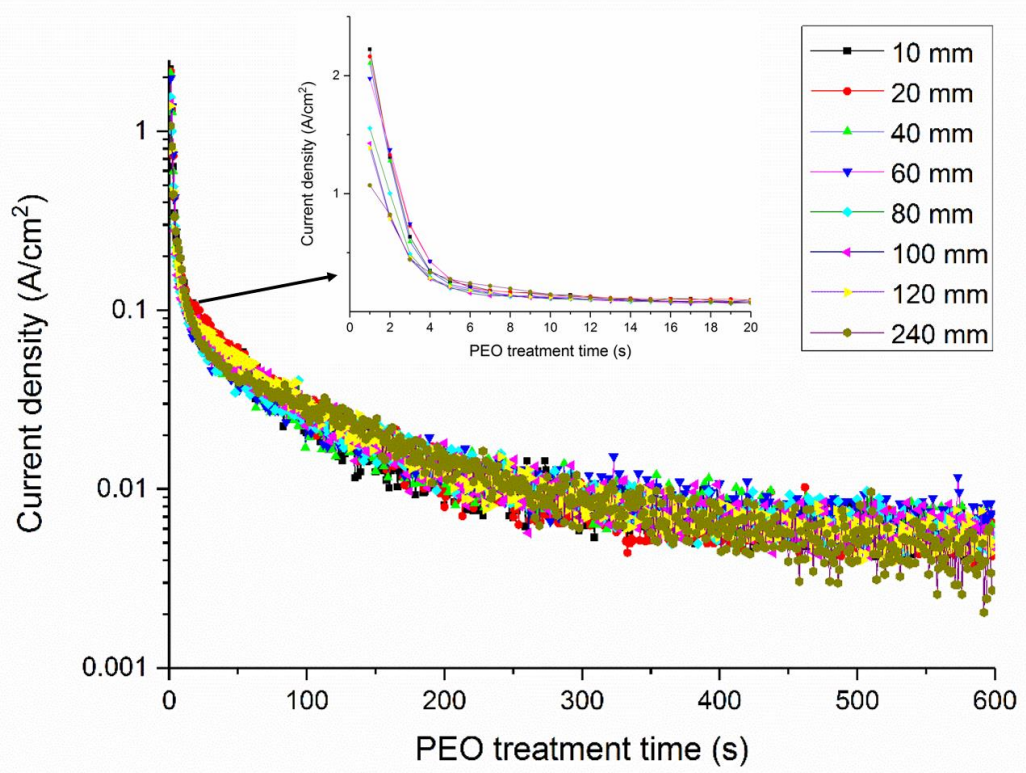

Fig. 6.1 Evolution of current vs. treatment time during the PEO process using constant voltage mode for various electrode distances

6.1.2 Elemental and phase composition

The elemental compositions of the eight coatings determined by EDS in an area of 1 mm^2 of each coating surface are shown in Table 6.1. Mg, O, P are the main elements in all the coatings while the contents of Na, Al, K are small. The contents of Mg and Al decrease with increased electrode distance. The concentration of O, Na, K and P fluctuate with the increasing electrode distance.

Table 6.1 Surface compositions of the eight coatings determined by EDS analysis of a large surface area (1 mm^2)

Concentration (wt.%)	10 mm	20 mm	40 mm	60 mm	80 mm	100 mm	120 mm	240 mm
Mg	34	33	32	31	31	30	31	31
O	34	35	39	42	33	38	40	40
P	27	27	23	21	30	27	23	24
Na	1.8	1.9	3	3.8	4.5	4	4.9	4.2
Al	2.9	2.7	2.4	1.6	1.1	0.6	0.5	0.5
K	0.3	0.4	0.6	0.6	0.4	0.4	0.6	0.3

The XRD pattern obtained from the eight coatings in Fig. 6.2 shows little difference. Combined with the elemental analysis, XRD results indicate that all the coatings exhibit an identical phase composition of magnesium phosphate and magnesium oxide. Considering the same electrolyte components and stirring effect, the electrode distance has no effect on the chemical reaction mechanism of coating formation. Some papers [127,128] claimed that changing the current mode, like using pulsed bipolar current mode, can change the coating composition. Furthermore it is reported that duration and ratio of different stages during PEO process can be altered by the applied electrical process parameters [110], and as a result, they influence the number, intensity and energy of the micro-discharges [129] which can determine the thermal and chemical conditions during PEO process, and thus change the phase composition of the coating. Current density is the main source to provide energy for micro-discharge. In this research, the current density values of the initial stage are altered by the increasing electrode distances, but according to Fig. 6.1, this stage lasts obviously too short to change the phase composition. The appearance of Mg peaks is due to the X-ray beam which penetrates entirely the PEO coating and reaches the magnesium substrate. Differences of the ratio of α-Mg peak intensities are related to crystallographic texture effects. The intensity of α-Mg peaks for coating produced at 10 mm distance is the lowest, indicating that the PEO coating produced at 10 mm distance is the thickest.

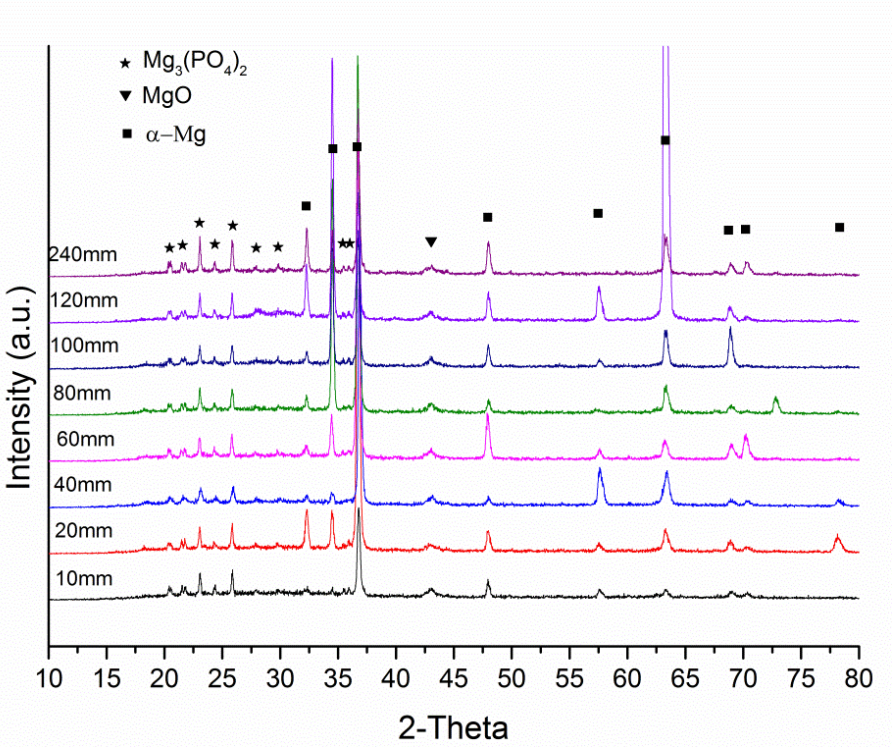

Fig. 6.2 XRD diffraction pattern obtained from the eight coatings with different electrode distances

6.1.3 Coating morphology

For the front sides of PEO coatings obtained from PEO process with different electrode distances, the surface morphology is displayed in Fig. 6.3 (a-h). The coating produced with a distance of 10 mm presents a rough surface covered by a large portion of thicker deposits. The ratio of the thicker deposit fraction decreases with the increase of electrode distance. The distances in the middle range (60 – 80 mm) show nearly perfect and uniform coating surfaces. For distances too remote non-uniform coating growth appears again, but the appearance has changed. The thicker regions appear to be loose and not perfectly sintered, maybe due to less current in the discharges. The polished cross-sections from the front sides of PEO coatings are shown in Fig.6.4 (a-h). Typically, PEO coating produced from phosphate-based electrolytes comprises up to three sub-layers [129], including a dense inner barrier layer, a region with accumulated pores in a form of a pore band and a more compact outer layer penetrated by discharge channels. The inner layers adjacent to the substrates are very thin and displaying wavy-jagged appearance. The outer layers contain irregular pores and discharge channels. Between the two layers elongated pore bands which are orientated parallel to the surface and normally observed when using phosphate based electrolyte and applying a DC mode on magnesium alloy substrates [129,130]. The same appearance is observed for the present

specimen. However, the volume fraction of pores accumulated in the pore band seems to decrease with electrode distance.

For the back sides of PEO coatings, the surface morphologies are showing the same trend like the front sides and provide no further information. SEM performed on polished cross-sections of the back sides of PEO coatings with different electrode distances are shown in Fig. 6.5. The coating thickness is thinner compared to the front side. It is evident that the coating thickness on the front side decreases as the electrode distance increases, but except for the coatings up to 20 mm distance, the coating thickness on the back side shows little difference. To summaries, PEO can produce thicker coatings at closer distances, uniform coatings in the middle range of electrode distances, but thinner and non-uniform coatings at further distances. So adjusting the electrode distance may offer an easy way to improve coating morphology and structure and produce adequately smooth coatings.

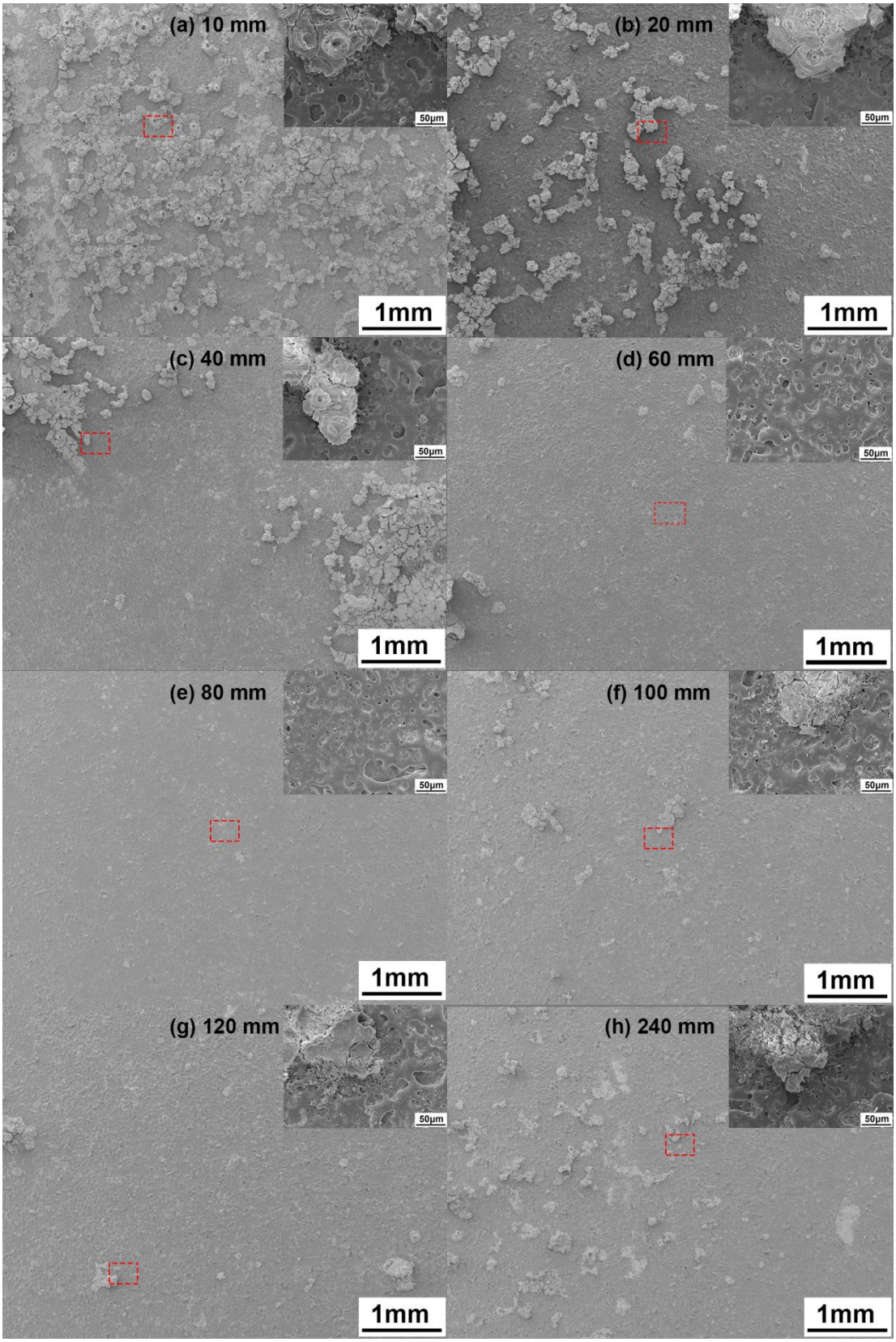

Fig. 6.3 SEM morphologies of free surfaces of the front surfaces of PEO coatings produced with different electrode distances. The red rectangles indicate where the high magnification images are taken.

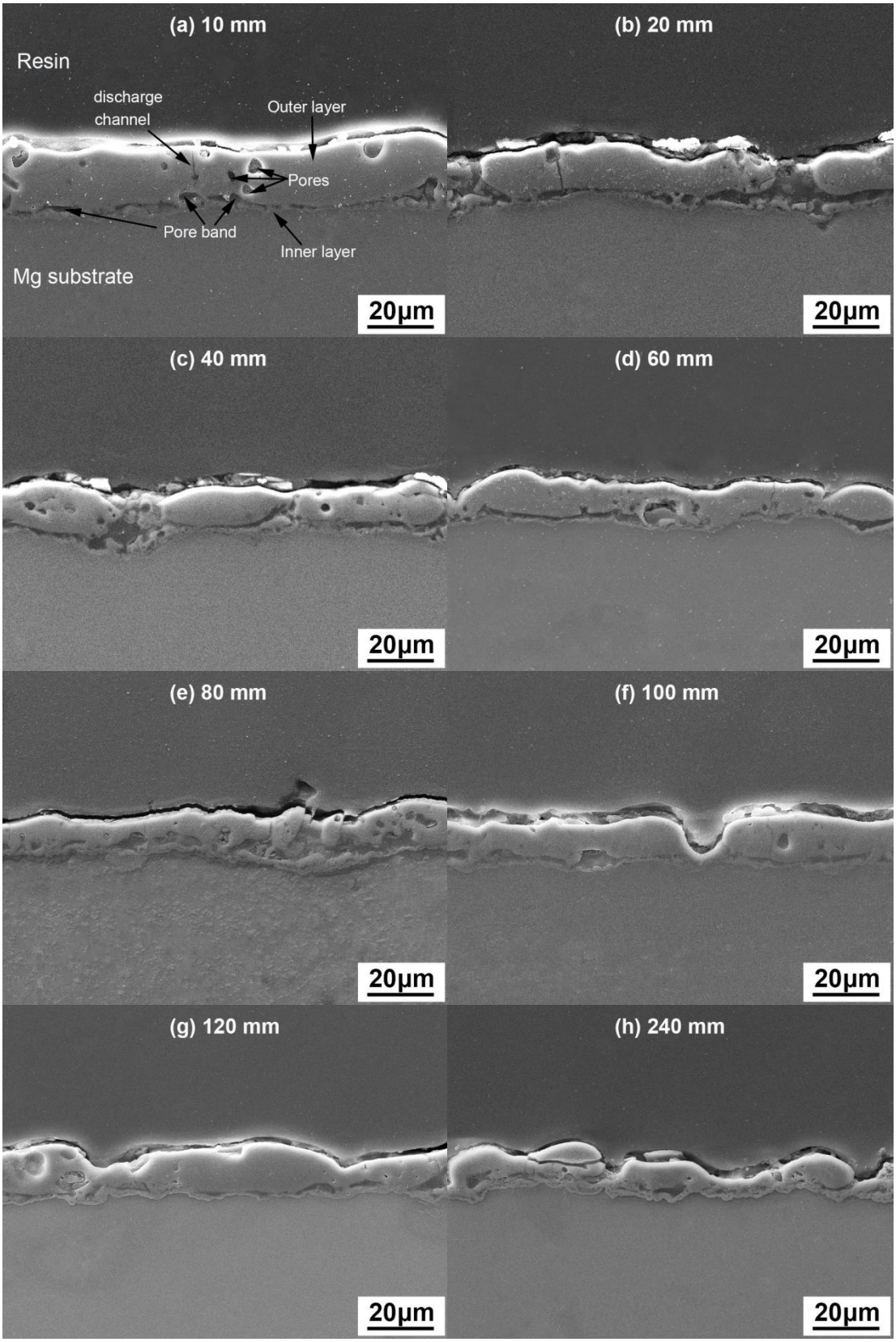

Fig. 6.4 SEM morphologies of the polished cross-sections on the front sides of PEO coatings prepared with different electrode distances

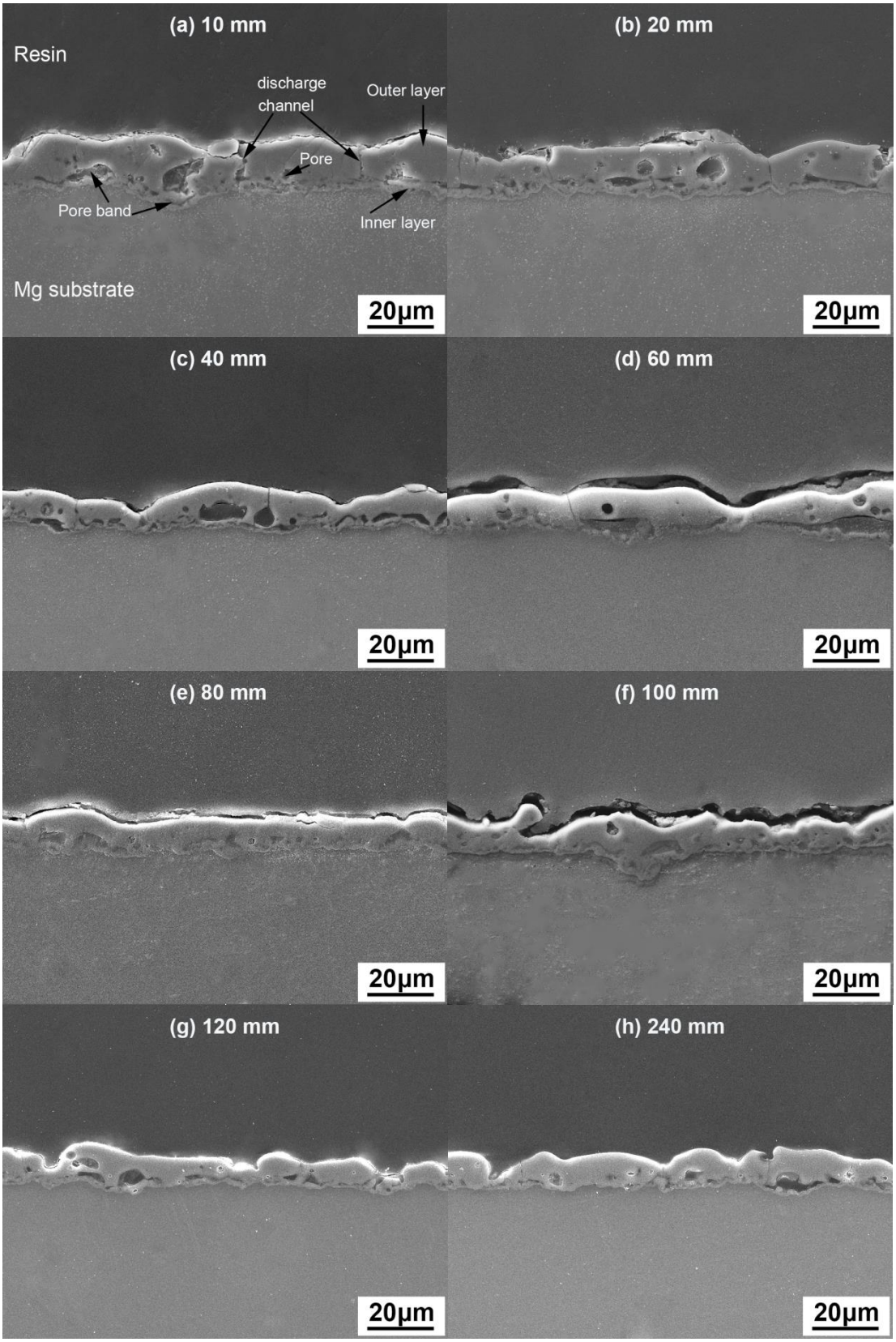

Fig. 6.5 SEM images of the polished cross-sections on the back sides of PEO coatings prepared with different electrode distances

6.1.4 Coating thickness

The evolution of the average coating thickness as a function of electrode distance for the front and back sides of PEO coatings is shown in Fig.6.6. It is observed that the coating thickness on the front side is higher for each electrode distance compared to the corresponding coating on the back side. Both front and back coating thickness values decrease nonlinearly with increasing electrode distance. The coating with 10 mm distance has the highest thickness values on both front and back sides which are 23 ± 3 μm and 15 ± 2 μm respectively. The coating with 240 mm distance has the lowest thickness values on both front and back sides which are 13 ± 2 μm and 12 ± 2 μm respectively. With increasing electrode distance, the front thickness decreases significantly, while the back thickness shows much less difference.

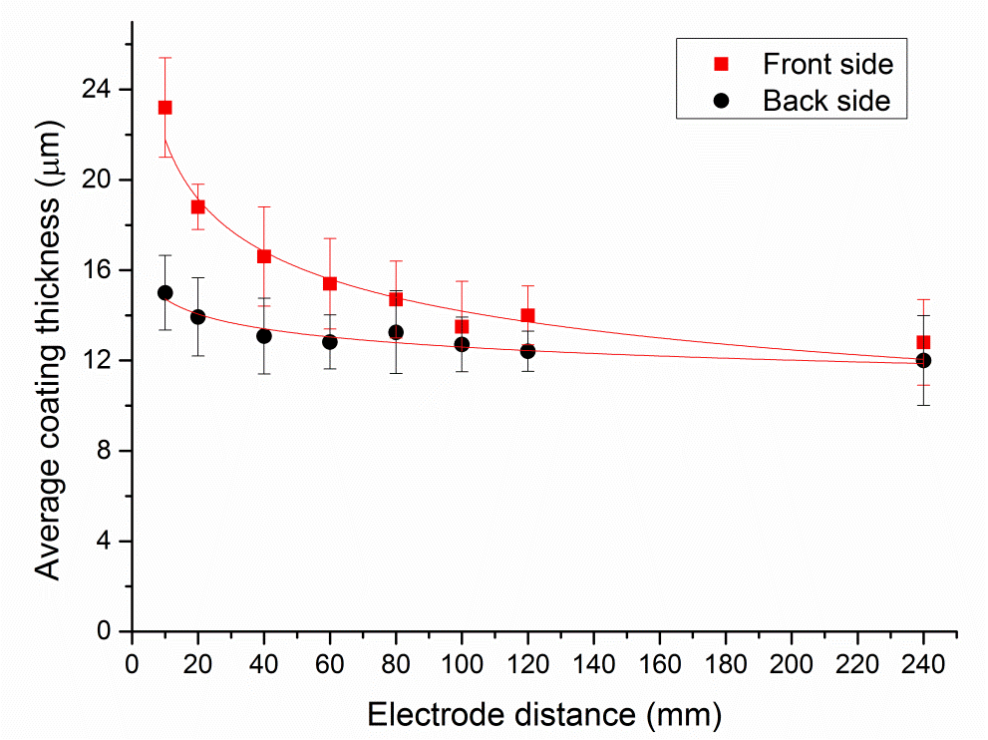

Fig.6.6 Dependence of the average coating thickness on electrode distance for both the front and back sides of the PEO coatings on AM50

6.1.5 Coating properties

In Fig.6.7, the dependence of the average coating roughness on electrode distance from 10 mm to 240 mm for both the front and back sides of the PEO coatings on AM50 alloys is shown. The values of the surface roughness on the front sides of the PEO coatings are higher than that on their corresponding back sides. It is believed that the surface roughness is dependent on the coating thickness. Under the same treatment condition, the thicker the coating is, the rougher

the surface is. The result of coating thickness shows that for each coating, the thickness on the front side is higher than that on the back side, which is in good agreement with roughness result. For different samples, the values of roughness on both sides decrease with the electrode distance firstly from 10 mm to 80 mm and reach the minimum when the electrode distance is 80 mm, then increase again with the electrode distance from 80 mm to 240 mm. The changes of surface roughness are in accordance with the changes of surface morphologies of the PEO coatings.

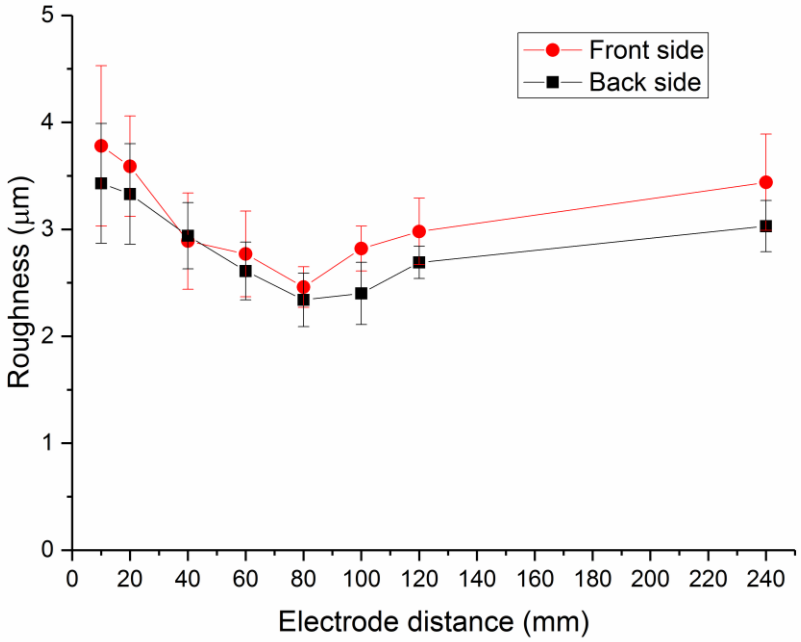

Fig. 6.7 The average coating roughness vs. electrode distance for both the front and back sides of the PEO coatings on AM50 alloy.

To get information on the resistance of the formed layers, EIS spectra were recorded during immersion in the same electrolyte that is used for the PEO process at the temperature of 10 °C for 30 min. Fig. 6.8 shows the Bode plots of the bare magnesium alloy after immersion in the same electrolyte as prepared for forming the coating at 10 °C for 5 min. The values of impedance modulus are around 4×10^4 Ω·cm^2 at 0.1 Hz and 54 Ω·cm^2 at 10^5 Hz. The electrochemical impedance spectra of the coated samples are depicted in Fig.6.9. The symbols are the experimental data and the solid lines are fitting data. The impedance modulus show relatively high values for the whole frequency range in this case, indicating that the coatings formed on magnesium alloy have a good corrosion resistance in the electrolyte solution. It can be seen that there is one time constant when the electrode distances is 10 mm, and when the

electrode distance ranges from 20 mm to 120 mm there are two time constants observed from the Bode plots, and three time constants appear when the electrode distance is 240 mm. Therefore, three different equivalent circuit models shown in Fig. 6.10 are used to fit the EIS of the PEO coated samples. In the circuits, R_s is the solution resistance, R_n and CPE_n represent the resistance and capacitance of the different layers, in which n represents the number of the layers in the coating. When the electrode distance is 10 mm, the outer layer of the coating is thick enough to prevent the electrolyte from penetration into the inner layer during the short measurement time, so it is the outer layer which provides the resistance and capacitance to corrosion. When the electrode distance ranges from 20 mm to 120 mm, coating thickness decreases and the electrolyte can reach out to the inner layer of the PEO coating. The inner layer is denser and more compact than the outer layer and hence provides resistance to corrosion. When the electrode distance is 240 mm, the coating has loose structure with the lowest thickness. The electrolyte solution can likely not only penetrate both outer layer and inner layer of the PEO coating, but also react with the metal substrate. This results in three time constants in its Bode plot. The coated substrates prepared by different electrode distances show diverse impedance values, especially at the low frequency range. The impedance at the lowest frequency (0.1 Hz) is one of the parameters that can be easily used to assess the corrosion performance of different systems [108]. The values of coating thickness and film resistance of PEO coated samples formed with different electrode distances are presented in Table 6.2.

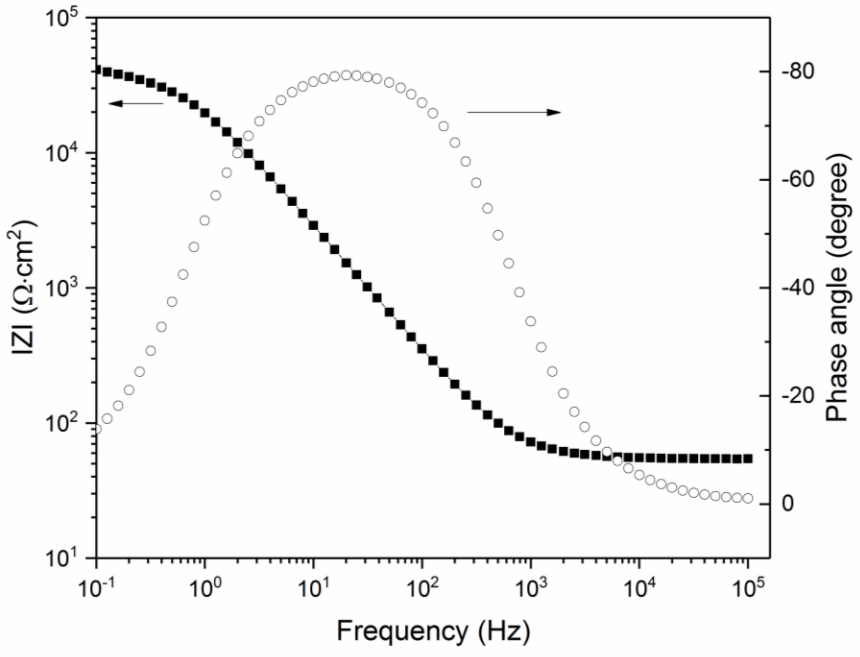

Fig.6.8 Bode plots of the bare AM50 alloy after immersion into the electrolyte for 5 min.

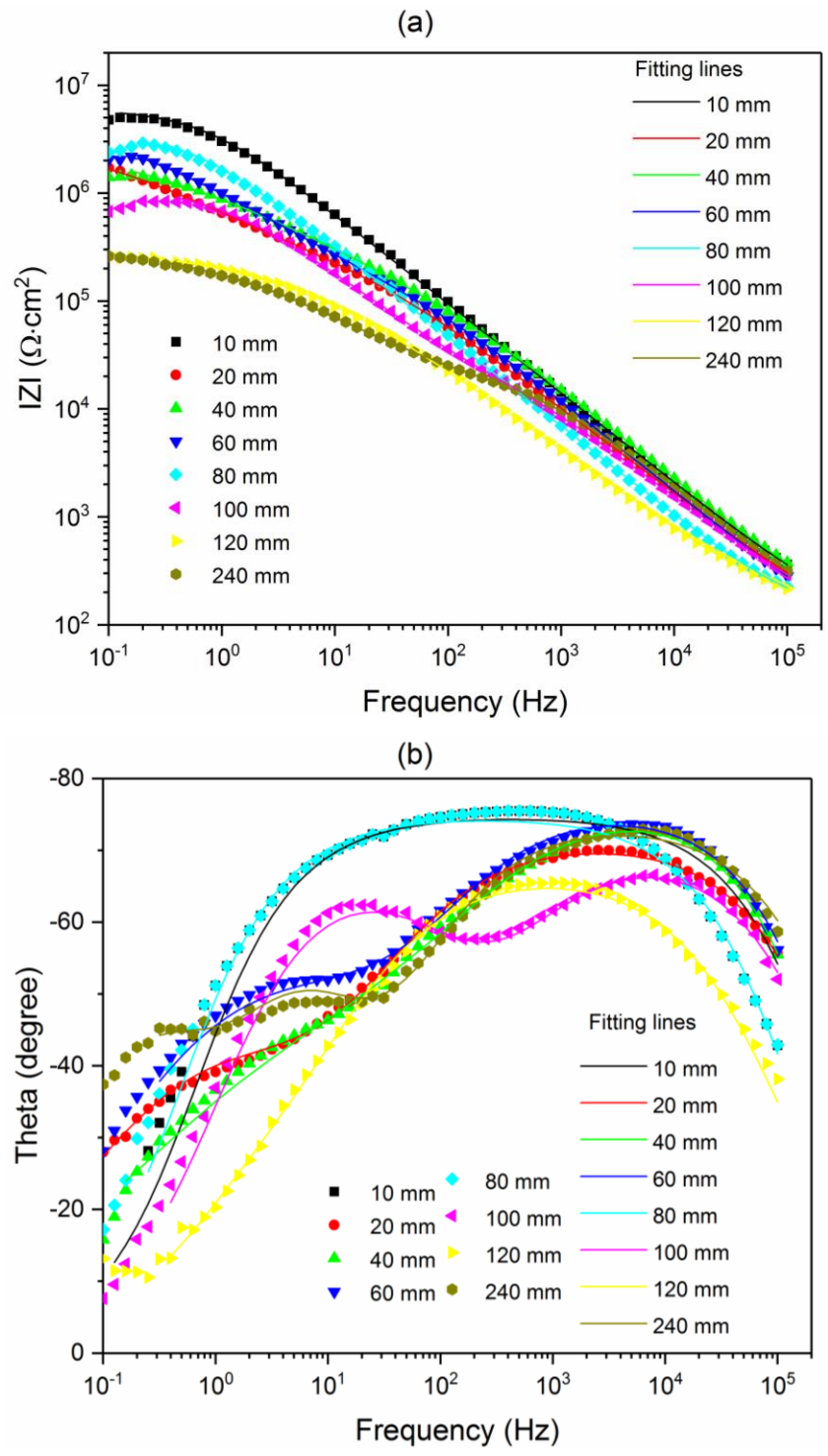

Fig. 6.9 The electrochemical impedance spectra of the coated substrates immersed into the electrolyte.

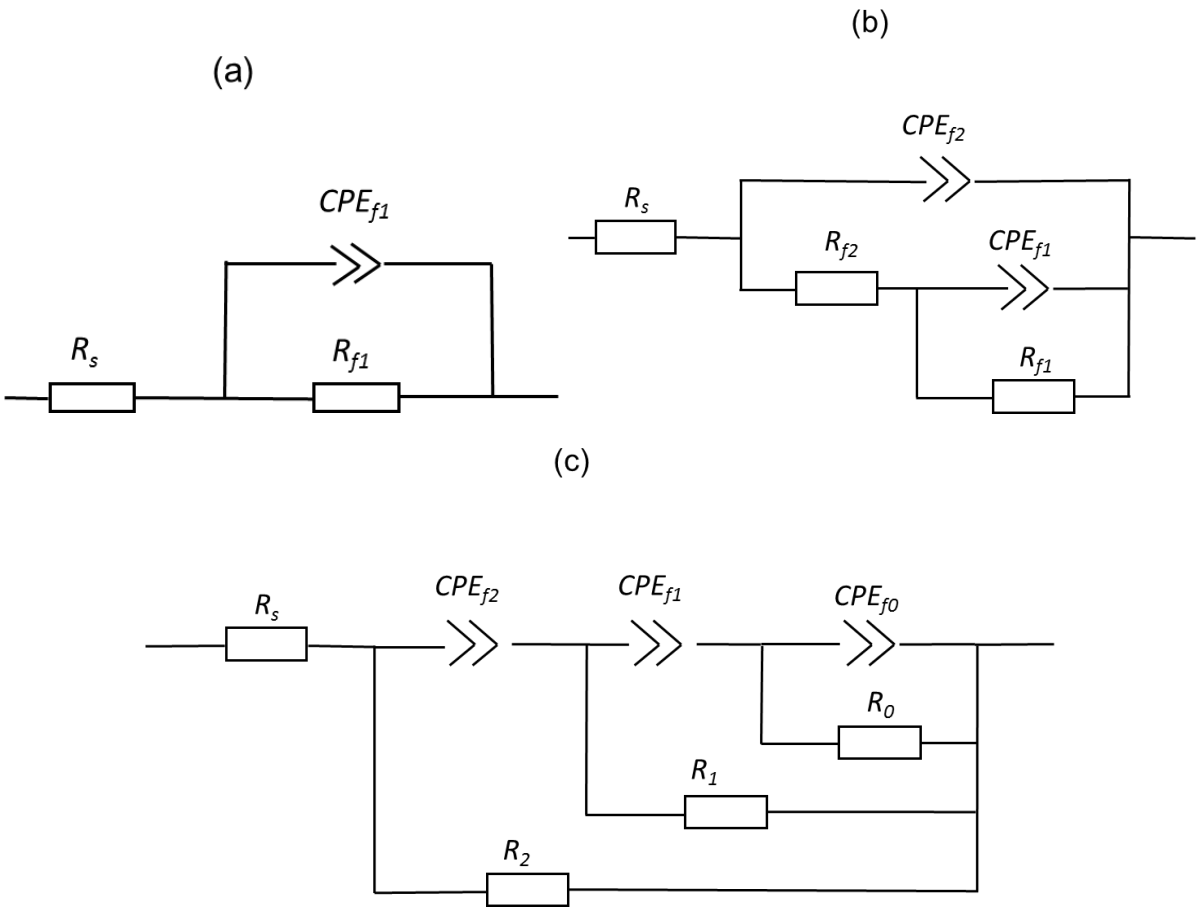

Fig. 6.10 Equivalent circuit models used for numerical fitting of PEO coatings produced with electrode distance: (a) 10 mm; (b) form 20 mm to 120 mm; (c) 240 mm.

Table 6.2 Thickness and impedance of PEO coatings produced with different electrode distances.

Electrode distance	Front coating thickness (μm)	Impedance ($\Omega \cdot cm^2$)
10 mm	23.2	4.5e6
20 mm	18.8	1.9e6
40 mm	16.6	1.4e6
60 mm	15.4	2.0e6
80 mm	15.1	2.3e6
100 mm	13.8	6.7e5
120 mm	14	2.7e5
240 mm	12.8	2.6e5

From Table 6.2, it can be seen that the impedance values firstly decrease with the electrode distance from 10 mm to 60 mm and increase a little bit at 80 mm, then decrease again with the increasing electrode distance from 100 mm to 240 mm. Combined with the surface and cross section morphologies, it can be explained that the resistivity is influenced by porosity and thickness of the PEO coatings. From 10 mm to 60 mm, the smaller the electrode distance is, the larger the pores and the thickness values of the PEO coatings are. The large pores enable the penetration of solution into the coating, which accelerate the corrosion process of the coating. From 100 mm to 240 mm, the pores are small and the coating is thin. For the coating produced with 80 mm of electrode distance, its thickness is higher compared to coatings produced with electrode distance more than 100 mm and its pores and roughness are smaller compared to coatings produced with electrode distance less than 60 mm. Based on the results of electrochemical and roughness test, an optimum electrode distance of 80 mm was identified for paralleled plate-like electrodes under the chosen experimental conditions.

6.2 Modelling and simulation of electrode distance impact

In order to approach the PEO process realistically, a transient model extension including surface reactions and layer growth would be required. Therefore, the time dependent model established in Chapter 5.2 is used here for the eight groups of coated samples to study the effect of electrode distance on PEO coating and predict the coating thickness. For each electrode distance from 10 mm to 240 mm, the procedure and parameters of the modeling is exactly the

same as the one in Chapter 5.2 except that the values of A, B and K are different. For each electrode distance, the values of A, B and K are extracted from the current density evolution and the modeling will be simulated separately.

Table 6.3 The best values of *A*, *B* and K as a function of electrode distance

Electrode distance	*A*(Acm^{-2})	*B*	*K*
10 mm	8.7e-4	355	5.02e4
20 mm	1.98e-4	1.6e3	5.87e4
40 mm	4.06e-3	98	8.46e4
60 mm	4.4e-3	108	9.52e4
80 mm	2.3e-3	138	7.42e4
100 mm	-7.8e-3	-10.6	4.14e4
120 mm	-4.3e-3	-23.3	4.98e4
240 mm	-7.1e-3	-14.1	4.73e4

6.3 Simulation results and discussion

After modifying the PEO growth model to different electrode distances, information of the distribution of the electric field at the processing time of 1 s in the simplified 2-D model when the electrode distance changes from 10 mm to 240 mm are presented in Fig. 6.11. From the distribution of the electrolyte potential and the current density, the non-uniformity of the electric field in the electrolyte can be seen clearly. With increase of the electrode distance, the current density decreases and the electrolyte potential increases due to the increasing resistance of the electrolyte between the anode and the cathode.

The evolution of current density on both front and back sides of the coated samples with the electrode distance from 10 mm to 240 mm are presented in Fig.6.12. Under the constant voltage mode, the current density is influenced clearly by the distance between anode and cathode. The current density decreases with time rapidly at the initial stage and then slowly till the end of the processing time, similar with the experimentally measured current evolution. The current density on the front side is higher than that on the back side of each coated sample at any time during the PEO process. With the increasing electrode distance, the values of current density decrease gradually. The phenomenon is particularly obvious for the initial values of current density. Because with longer electrode distance, the resistance of the electrolyte becomes

higher and more potential is consumed by the electrolyte, so the current density will decrease with the electrode distance. The difference of the values of current density between the front side and the back side is the largest when the electrode distance is 10 mm, and then with the increase of the electrode distance, the difference between them decreases gradually.

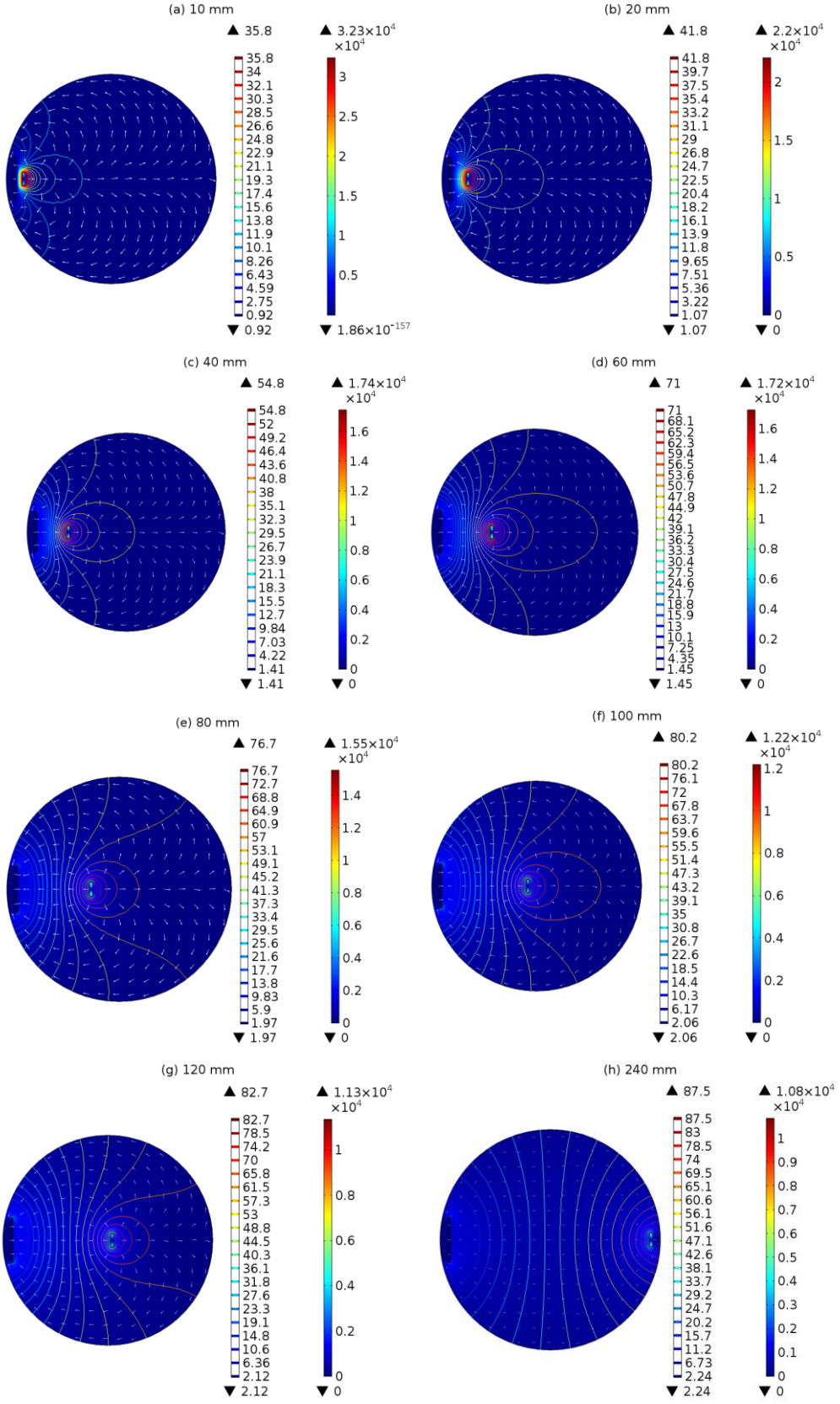

Fig. 6.11 Distribution of electric field when the electrode distance ranges from 10 mm to 240 mm at t = 1 s: the contour line represents the electrolyte potential (V); the arrows represent the current density (A/m^2) in the electrolyte.

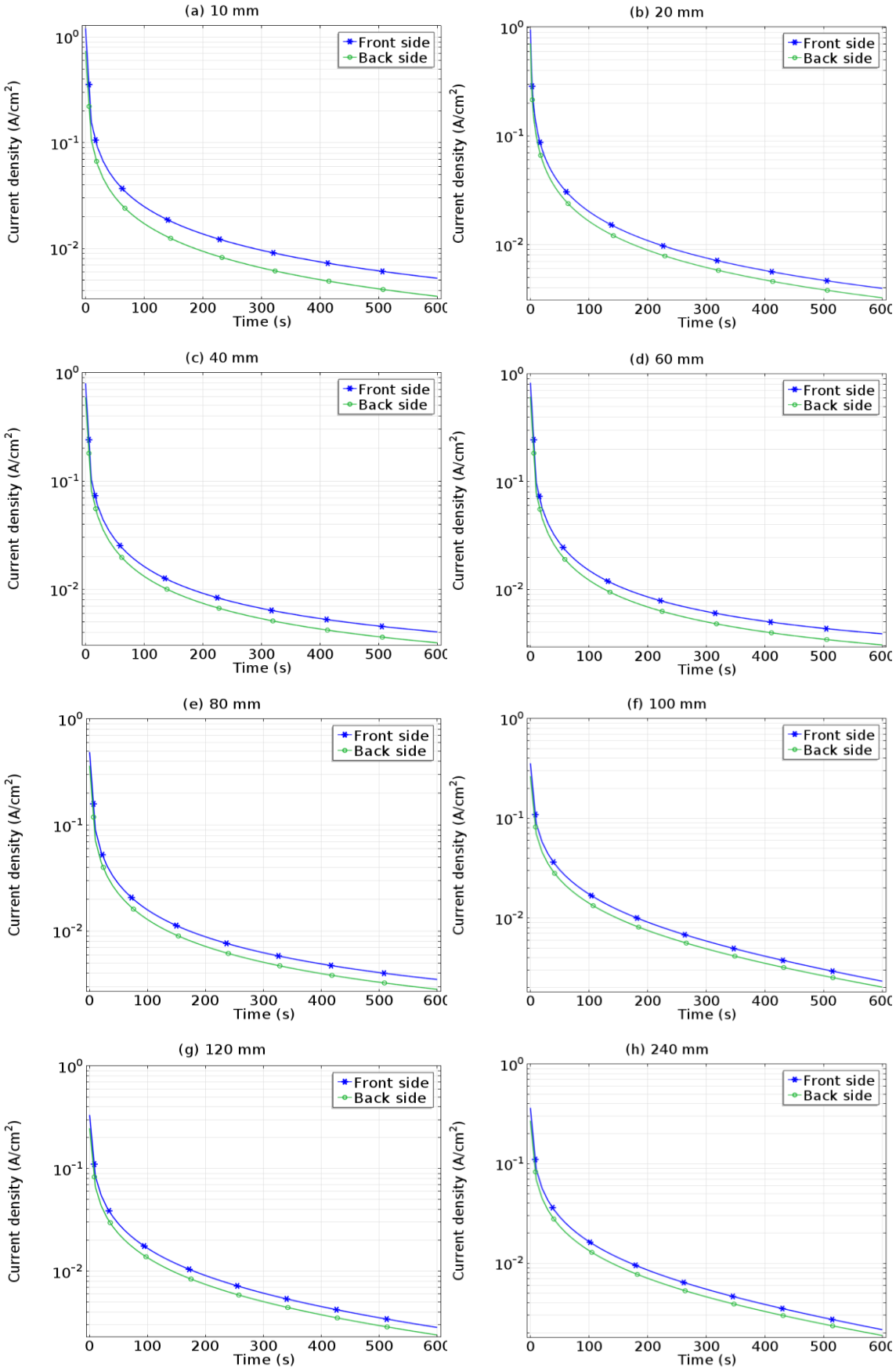

Fig.6.12 The simulation results of evolution of average current density on both front and back sides of coated samples with the electrode distance from 10 mm to 240 mm.

The dependence of current density distribution on the front and back surfaces of the anode on the electrode distance at different times can be extracted from the modelling and presented in Fig. 6.13. For each specimen, a higher current density is predicted on the front compared to the back surface because of a shelter effect [126], and the difference of current density between the front side and the back side becomes smaller with increasing treatment time. The current density distributes non-uniformly decreasing from outside to the center of the substrate surface. This is due to the edge effect. The cathode surface area is larger than the anode normal projection, so the extra cathode exchange current flow into the volume of electrolyte available beyond the anode edge and has to concentrate on the edges again [131]. This produces the edge effect and results in a higher current density at the outsides compared to the center of the anode surface. On the other hand, both front and back current density decrease with an increasing electrode distance. The difference between them becomes smaller with the electrode distance as well, which indicates that the current density distributes more and more uniformly. Experimental results in Ref. [126] proved that the current flowing through the front surface is higher than that flowing through the back surface and the average current decreases with larger electrode distances, which corresponds to the simulation results of the model obtained here.

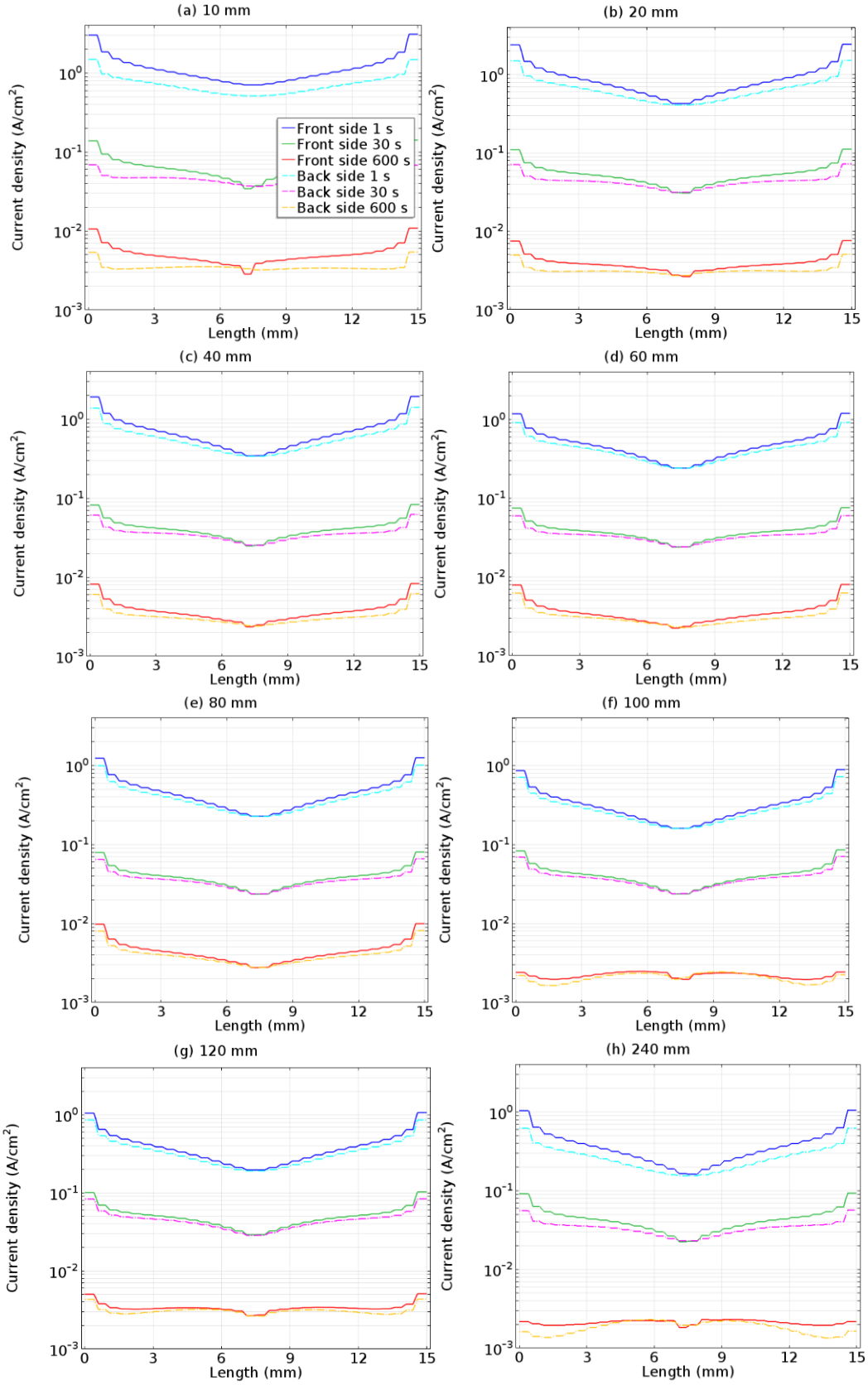

Fig. 6.13 Simulated current density distribution on the surfaces of the front sides and back sides of the anodes (length 15 mm) for different electrode distances between 10 mm and 240 mm.

The whole electric charges passing through the front side and the back side are calculated after 10 min and shown in Fig. 6.14 as a function of electrode distance from 10 mm to 240 mm. Both the front and back decrease with larger electrode distances nonlinearly, but the evolution on the front surface is much more evident compared to the back side, especially within short distances up to 80 mm. After 100 mm, the decrease rate of the electric charges on both front and back surfaces becomes lower and the discrepancy of the charges between front and back surfaces gets smaller. When the distance is close, the electric field strength between anode and cathode can be deemed as uniform, so the front anode current decays reciprocally with the electrode distance. When the electrode distance becomes larger, the electric field between anode and cathode becomes non-uniform and thus has a weaker influence on anode current. As for the back side of the anode, the electric field is always non-uniform, and due to the shelter effect [126] of the front side, the anode current of the back side is lower than that on the front side. This results in the different values of electric charges on the front and back sides of the samples with different electrode distance.

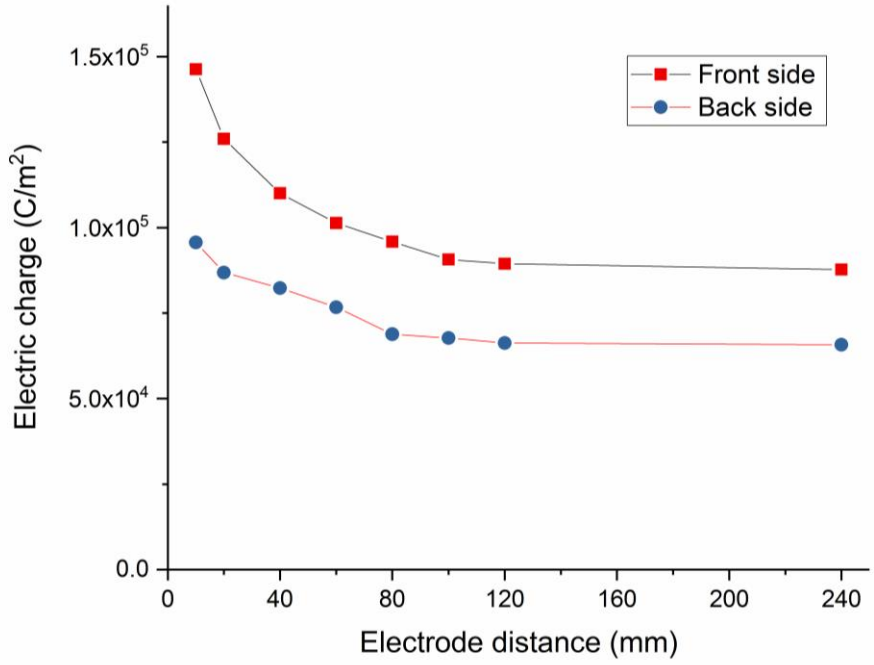

Fig. 6.14 The simulation results of the whole electric charge passing through both front and back sides of the coated samples as a function of the electrode distance from 10 mm to 240 mm.

Fig. 6.15 shows the evolution of average coating thickness on both front and back sides of the coated samples with the electrode distance from 10 mm to 240 mm. The average coating thickness increases with time on both the front and back sides. Because the coating thickness is dependent on the current according to Faraday's law, the values of the coating thickness increase with decreasing growth rate due to the decreasing current density over time. The coating thickness is thicker on the front side than that on the back side and the larger the electrode distance is the thinner the coating thickness gets, which is consistent with the simulation results of the current density and the experimental observations.

The experimental and simulation values of coating thickness on both the front and the back sides of each sample after PEO processing for 10 min are shown in Fig. 6.16 and compared with each other. The final coating thickness after 10 min on both sides decreases with increasing electrode distance. However, the changes of coating thickness on the front sides are more rapidly than that on the back sides, especially at the smaller range of the electrode distance. The dependence of the final coating thickness on the electrode distance is similar with the evolution of electric charges vs. electrode distance in Fig. 6.14, suggesting the linear relationship between the whole electric charge and the coating thickness of Faraday's law. When the electrode distance is 10 mm, the difference of the average coating thickness between the front side and the back side is the largest, and the values of the average coating thickness are 25.6 μm and 16.7 μm on the front side and the back side respectively. When the the electrode distance is 240 mm, the difference of the average coating thickness between the front side and the back side is the smallest, and the values of the average coating thickness are 15 μm and 12.5 μm on the front side and the back side respectively. Compared with the experiments, the simulation results of coating thickness are in good agreement with the experimental results of coating thickness, proving the usefulness of the model in predicting the coating thickness.

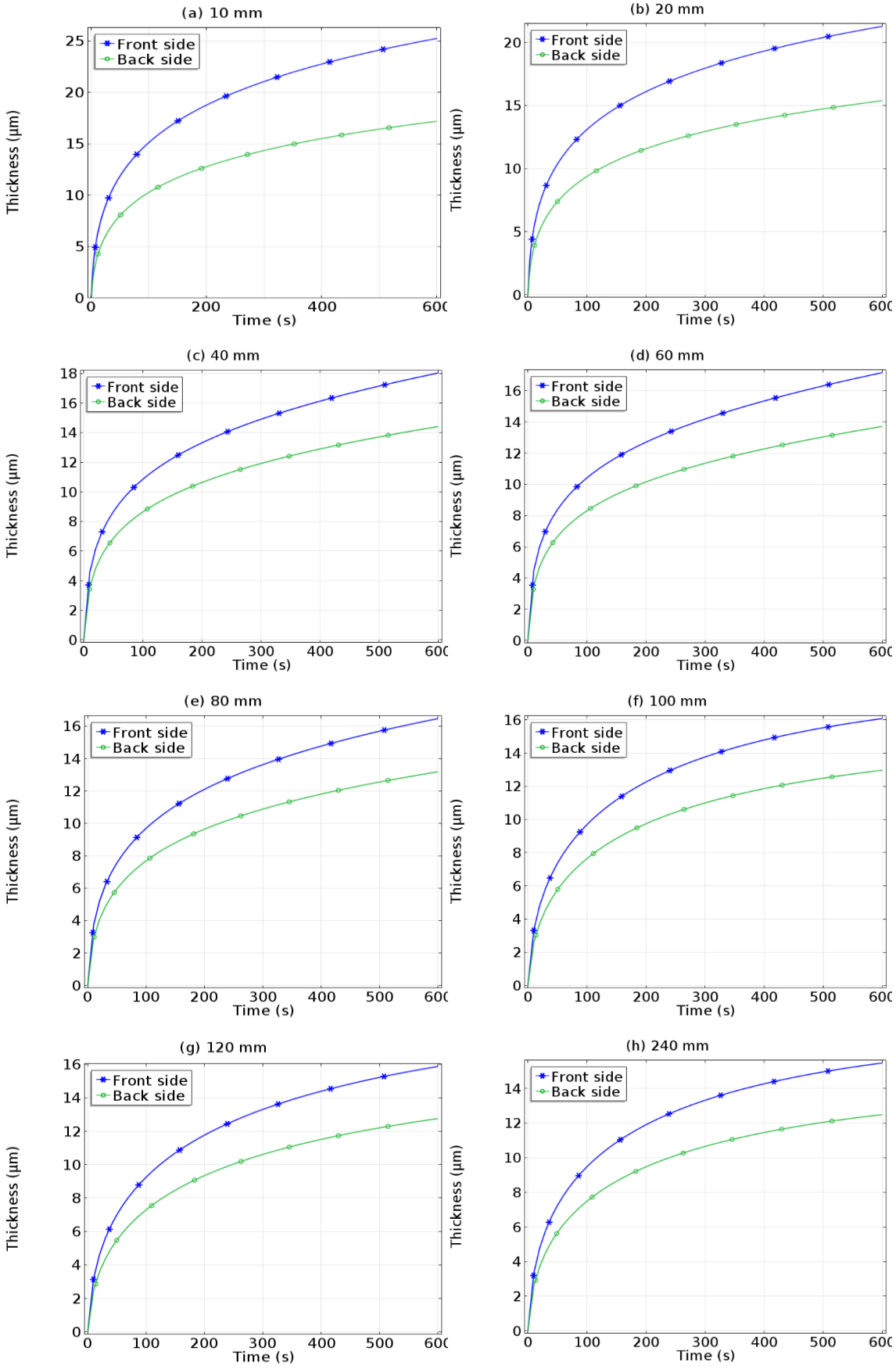

Fig.6.15 The simulation results of evolution of average coating thickness on both front and back sides of the coated samples with the electrode distance from 10 mm to 240 mm

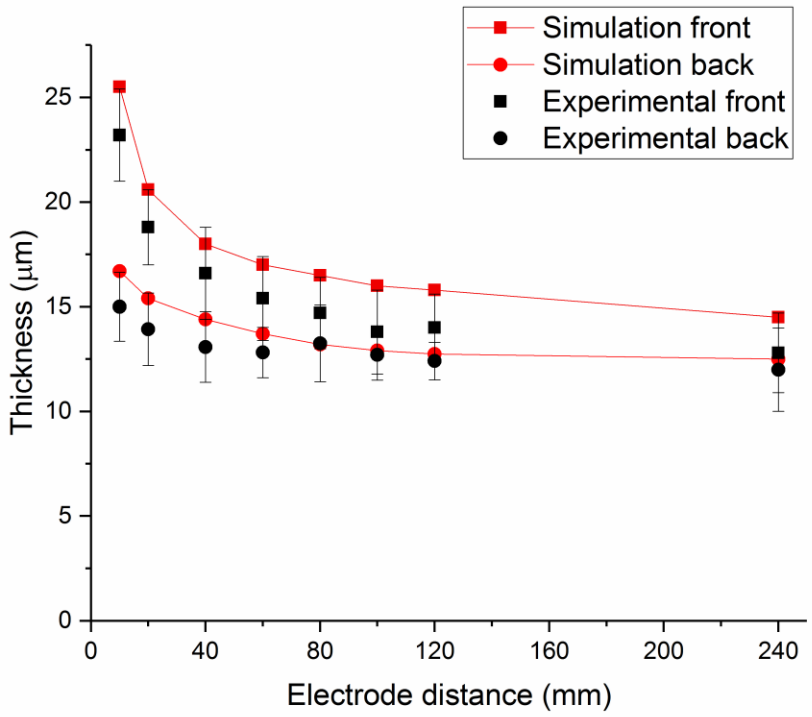

Fig. 6.16 The experimental and simulation results of the final average coating thickness on both front and back sides of the coated samples vs. electrode distance from 10 mm to 240 mm.

It is well-known that anode current distribution on the whole surface of the specimen has a critical effect on the uniformity of the surface properties and coating thickness [29]. According to one PEO coating formation mechanism proposed [132], three main steps lead to PEO coating formation. In the first step, Mg and alloying elements are melted out of the substrate owing to the high temperature generated by electron avalanches, then enter the discharge channel due to the strong electric field, and get oxidized. Second, these oxidized Mg is ejected from the channel into the coating surface in contact with the electrolyte, thereby increasing the coating thickness in that location. In the last step, the discharge channel gets cooled and the reaction products are deposited onto its walls. The above process repeats itself at a number of discrete locations over the entire coating surface, leading to an overall increase in the coating thickness. In accordance with Faraday's laws of electrolysis, coating thickness is proportional to the quantity of electricity transferred at the anode. Even though the efficiency of PEO coating formation for magnesium is low due to oxygen generation, dissolution of species in the electrolyte and loss of coating material [133], it is still a common sense that coating thickness grows linearly with the PEO processing time in constant current mode, which could be

explained by this formation mechanism [44]. In constant voltage mode, the simulation results of front and back current density show the same tendency of evolution. The electrode distance can change the values of the current density because of the different electrolyte resistance between the anode and cathode. Therefore the the electricity resulted from electrode distance in the same period of PEO treatment time shows different quantity. The charges passing through the front side and back sides of the anodes as a function of electrode distance show the similar tendency as the coating thickness of front and back sides respectively, indicating that the coating thickness depends mainly on the current. Closer distance can reduce the current loss, providing higher current density and result in a thicker coating.

The results of time dependent models reproduce the evolution of current density and coating thickness on the front and back side of the anodes with different electrode distance close to the experimental values. It also reveals that electrode distance is an important factor which can affect coating thickness through changing the current density. This is in good agreement with experimental findings provided by Wei et al. [126].

6.4 Summary

The influence of electrode distance between anode and cathode during plasma electrolytic oxidation process on the coating formation has been investigated by combining experiments and simulation. The stationary model and time-dependent model are both applied. The stationary model simulates the initial stage of PEO process and the distribution of electrical field in the electrolyte. The time-dependent model based on the PEO coating growth model simulates the evolution of coating growth at each condition separately. Complementary, PEO coatings were fabricated on AM50 magnesium alloy in an alkaline electrolyte with different electrode distances applying constant voltage. Phase composition, coating morphology and thickness were studied for both the front and back sides of the PEO coating depending on the electrode distance. Via correlation of simulation and experimental results, the influence of electrode distance on coating formation is explored. The conclusions are as follow:

1. The simulation results of the stationary model reveal, on one hand, that current distributes non-uniformly along the substrate surfaces and decreases from the edges to the center. With increasing distance, the current gradients from edges to the center get smaller, which means that the current distribution becomes more and more uniform. On the other hand, increasing electrode distances result in a nonlinear decline of the

average current density at the front and back surfaces of anodes. This also lowers current density differences between them.

2. By applying the PEO coating growth model to each condition of electrode distance, the effect of electrode distance on PEO coatings can be studied time-dependently. The simulation results of the time dependent model show the evolution of current density and coating thickness clearly on both the front and back sides of the samples with the selected electrode distances. It comes to the same conclusion with the stationary model that the electrode distance can affect the current density on the coated samples and therefore change the coating thickness on both the front and back sides.
3. The experimental results show that elemental composition, surface morphology, thickness, roughness and resistance of PEO coatings are influenced by the electrode distance, although there is no influence on the phase composition. The coating on the front side of the sample is thicker than that on the back side of the same sample. The experimentally determined thickness evolution with increasing electrode distances show the same tendency as the modeled and experimentally measured current density, and are in good agreement with the simulated coating thickness from the time dependent model. The results above indicate that the electrode distance can indeed affect the coating characteristics through changing the current distribution and evolution on the front and back surfaces of the sample. For paralleled plate-like electrodes, based on coating uniformity, the results of electrochemical and roughness test, an optimum electrode distance of 80 mm was identified under the chosen experimental conditions.

Therefore, it can be concluded that the electrode distance is not negligible. In contrast, it is an important factor that can influence PEO coating properties through altering the current distribution in the bath and current evolution on the surface of treated materials under constant voltage mode.

7. Investigation of substrate geometry impact on PEO coating formation assisted by simulation

Compared with other surface treatment technologies, PEO treatment of light metals is attractive for industrial application because of several benefits as mentioned in Chapter 1. One of the most important features is that PEO process is capable of non-line-of-sight treatment. The ability of non-line-of-sight treatment is of particular importance for industry, which means one can form coatings on multiple sides of samples or even on substrates with complex geometry [11]. In all the literature studying PEO process, most of them utilize samples with simplified geometries such as rectangular samples and cylinders. Only a few studies were preparing PEO coatings on substrates with complex geometry because non-uniform coating thickness and surface properties may be an issue at different locations on substrates with complex shapes. However, electrode geometry is also one of the main factors that influence the formation of the continuous plasma envelope [29]. On the other hand, there are studies proving that even for a simplified plate sample, the anodic currents flowing through the front and the back surfaces are different, and therefore lead to different oxidation dynamics at different locations on the samples resulting in a non-uniform coating thickness and surface properties [126,134]. Then it is reasonable to speculate that the situation on substrates with complex geometry may be even more complicated. Since uniformity is one of the main factors that influence properties of PEO coatings, the PEO coatings formed on complex geometries are worthy of study for industrial application.

Due to above reasons, it is important to discuss the impact of substrate geometry on PEO coatings. In this study, the substrate geometry refers to the rectangular sample of magnesium alloy AM50 with a hole of predefined diameter in the center. Coatings are formed on those samples under the same voltage mode of PEO process. Thus, the impact of different shapes of substrates on morphologies, compositions and thicknesses of PEO coatings at different locations will be discussed. The volumes inside of the holes are so small that it is difficult to observe the phenomena happening during the PEO process. Besides, the distribution of anode current on the whole surface of the specimen has a decisive effect on the uniformity of the coating thickness and surface properties but fails to be measured through experiments. Fortunately, modeling and simulation describing the PEO process can accomplish those tasks numerically and help to achieve better insights into the influence of substrate geometry. Based on the coating growth model studied before, a 3D model is built to simulate and to predict the

effect of substrate geometry on the anodic current distribution and coating formation using finite element analyses. Via correlation of simulation and experimental results, the influence of substrate geometry on coating formation will be explored, and the application of the PEO-coating growth model will be verified.

7.1 Experimental results

7.1.1 Voltage and current density evolution

Fig. 7.1 shows the voltage and current density transients measured from samples with different diameters with holes ranging from 0.5 mm to 6 mm at an anodically applied potential of 350 V in 10 min. The observation of discharges begins when the applied potential exceeds approx. 240 V, so it is assumed in this work that the breakdown potential for the PEO coatings is 240 V. In Fig. 7.1(a), the voltage values for the six samples increase rapidly with time and reach to 350 V after 3 or 4 seconds, then they remain constant until the end of the PEO process. During the ramp period of the voltage, there are slight difference between the six samples. Thus, the voltage values at 1 s are different. Samples with big diameters of holes have higher voltage values than those with small diameters. Furthermore, samples with larger diameters of holes reach breakdown voltage and final voltage 350 V earlier than those with small diameters. In Fig. 7.1(b), there are slight differences between current density during the first 30 s, but then the current transients are getting closer and closer together and at the end of PEO process time it is hard to distinguish the differences between the six samples.

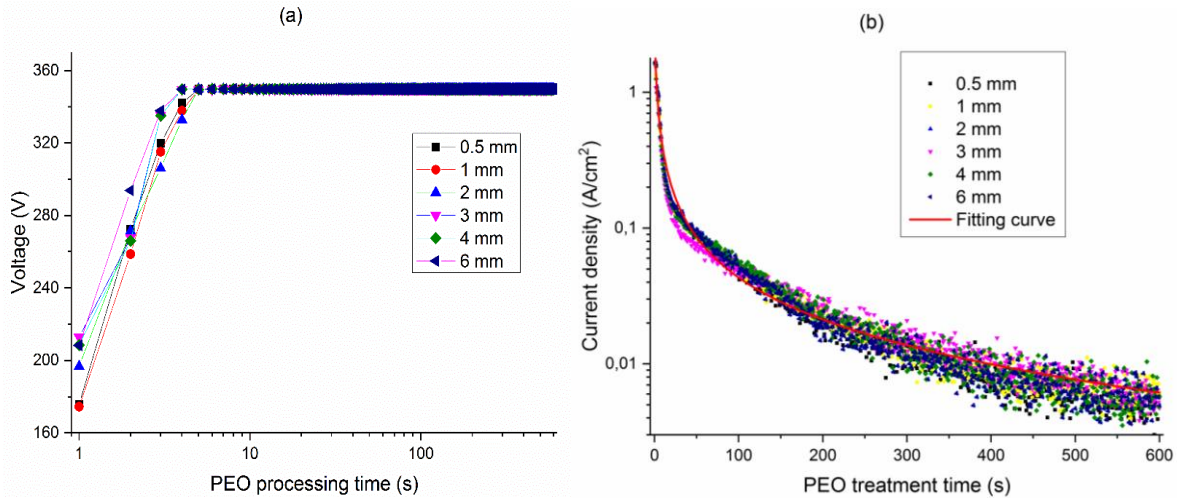

Fig. 7.1 Voltage (a) and current density (b) transients measured from samples with different diameters of holes ranging from 0.5 mm to 6 mm at an anodic applied potential of 350V in 10 min and the corresponding fitting curve for current density.

It is clear that the different sizes of holes have little influence on the voltage and anodic current density evolutions. The evolution of current density for the six samples can be fitted by the same equation (7.1) given below and the fitted curve is in good agreement with experimental values.

$$j(t) = 3.448 - \frac{3.446 \times t^{0.98}}{1.2 + t^{0.98}} \qquad (7.1)$$

The relationship between current density and treatment time can be used as modeling input data.

7.1.2 Characterization of PEO coating on flat surface

The characterizations of PEO coatings at two different locations, namely the flat coatings and the round coatings, are discussed separately to determine the influence of substrate geometry on PEO coating formation. Fig. 7.2 depicts SEM morphologies of PEO coatings chosen from the flat surfaces of AM50 substrates with different diameters of holes in a random way. All the coatings show the same typical structure with micropores and projections [74]. No obvious differences are observed between those flat surfaces.

Fig. 7.3 shows the elemental compositions detected by EDS on the flat surfaces of PEO coated samples with different diameters of holes. All the flat coatings are composed mainly by Mg, O, P and a small amount of Na, K and Al. Mg and Al are derived from the alloy. P, Na, and K are

captured from the electrolyte. O comes from both the electrolyte and oxygen in the air. The contents of these elements in different coatings have little variation and the contents for O, Mg and P are around 46 at.% (atomic percentage), 30 at.% and 20 at.% respectively. Because of the similar morphologies and elemental contents, it is believed that the main phases in the flat coatings will be the same. According to our prior experimental results [134], the major phases in the coatings are MgO and $Mg_3(PO_4)_2$.

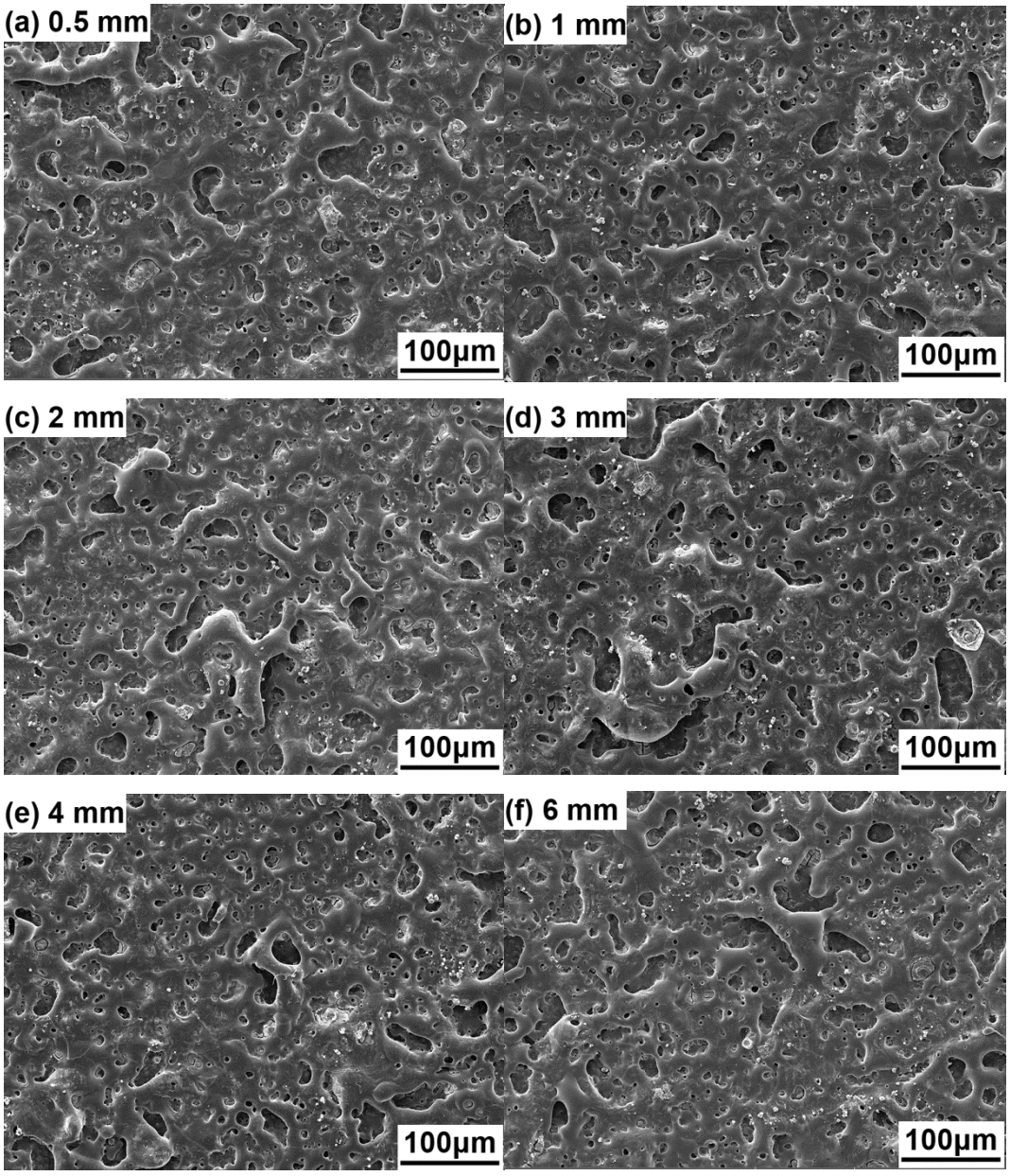

Fig. 7.2 SEM morphologies of PEO coatings on the flat surfaces of AM50 substrates with different diameters of holes.

Fig. 7.4 shows the average thickness of the flat PEO coating as a function of hole diameter with

the error bar showing standard deviations. The coatings on the flat surfaces have almost the same thicknesses around 17 μm. Therefore, the change of hole diameter has little influence on the morphology, composition and thickness of the flat coating.

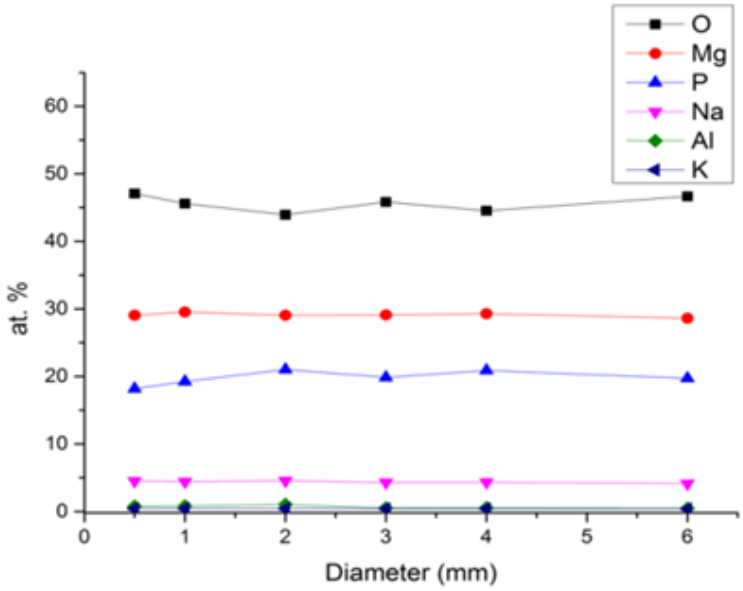

Fig. 7.3 Elemental composition detected by EDS on the flat surfaces of PEO coated samples with different diameters of holes.

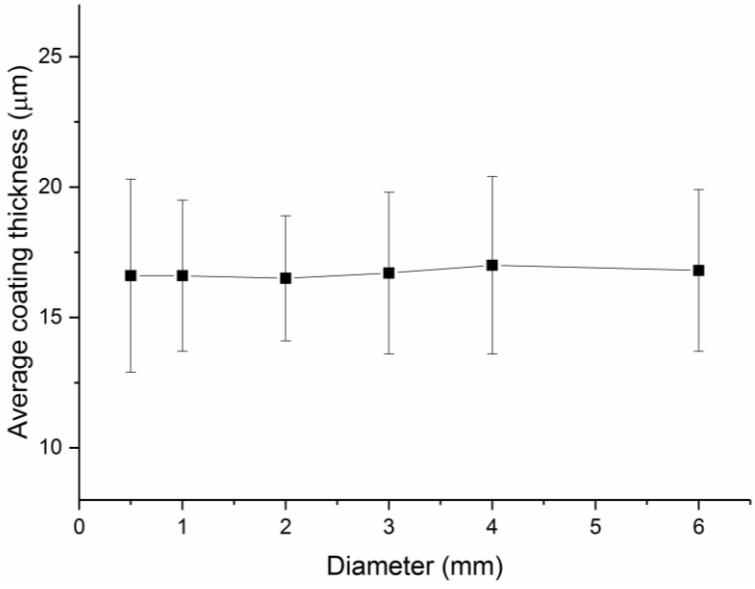

Fig. 7.4 Average thickness of PEO coating on flat surface with the error bar showing standard deviations as a function of hole diameter.

7.1.3 Characterization of PEO coating on round surface

Fig. 7.5 shows the morphologies of PEO coatings in the middle of the round surfaces of AM50 substrates with different diameters of holes. When the diameter is 0.5 mm, the image shows that there is no typical PEO coating on the round surface. Instead, the substrate is covered by loose and cracked conversion products which are similar with those formed during PEO process before reaching the breakdown potential [135]. It is possible that there are few discharges in the hole during PEO processing. The formation of discharges is influenced by the current density, the defects of local uneven electrical conductivity, the impurity level, the resistance of the coating, and the ionization coefficient of the metal oxide coating [136]. However, it is difficult to monitor the discharge behavior inside the holes by experiment. When the diameter increases to 1 mm, the round surface is covered by conversion products, rod-like particles and typical PEO structure with tiny pores and small-size projections. This morphology is similar to the flat coating treated by PEO process after reaching the breakdown potential for a short time [135]. As the diameter increases to 2 mm, no conversion products or rod-like particles can be seen in Fig. 7.5(c), and the typical PEO coating morphology is visible covering the round surface. The micropores and projections are still small, indicating the PEO coating is thin. After the diameter reaches to 3 mm, the surfaces of the round coatings show identical morphologies of typical PEO coatings. Compared with the morphologies of the flat surfaces in Fig. 7.2, Fig. 7.5 (d) – (f) have smaller sized projections, indicating the coating thickness on the round surfaces are thinner than that on the flat coatings.

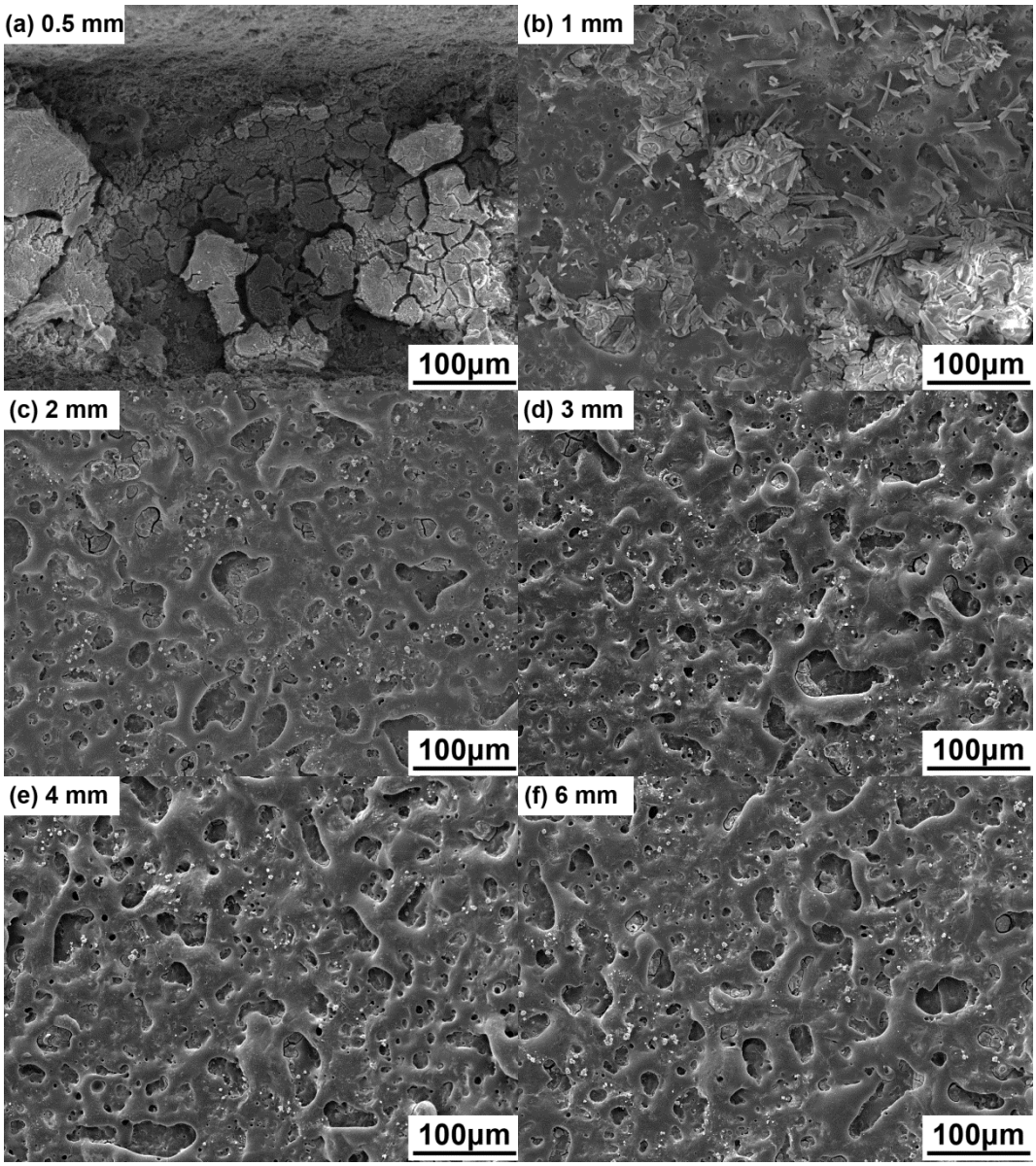

Fig. 7.5 SEM morphologies of PEO coatings on the round surfaces of AM50 substrates with different diameters of holes.

Element composition along the length of the hole detected from the round surfaces of PEO coatings by EDS for different diameters of holes are presented in Fig. 7.6. For each sample, ten regions with the same areas from 1 to 10 are arranged equidistantly from the front side to the back side along the hole length. Fig. 7.6 (a) – (f) show how the elements on the round coatings distribute from the front side to the back side directly. It is evident that the elemental contents are much more uniformly distributed after 2 mm than that of samples with diameters of 0.5 mm and 1 mm. When the diameters are 0.5 and 1 mm, the contents of the main elements O, Mg and P fluctuate along with the hole length. The contents of Mg in both coatings are much lower compared to the flat coating. Compared with the flat surface composition in Fig. 7.3, the

elemental composition of 0.5 mm hole in region 1 is the same, but from region 2 to region 10, the amounts of O are much higher and the amounts of Mg and P elements are lower. The content of P in 1 mm hole is higher than that in 0.5 mm hole. When the diameter is 2 mm, the content of Mg in the middle part is around 28%. From 3 mm to 6 mm, the contents of Mg in the coatings remain around 30%, similar with that in the flat coatings. Mg element in the coating is derived from the substrate alloy by electrochemical reaction. The contents of Mg in the middle parts of the holes are lower than that around the edges when the hole diameters are less than 2 mm, which may indicate that the current distribution in the holes is strongly affected when the diameters are small. After the hole diameters reach to 2 mm, the contents of O in the round coatings are around 41%, which is smaller than that in the flat coatings. O comes from both electrolyte and oxygen in the air, so the decrease of O content in holes may result from the lack of air or electrolyte in the holes. The distribution of elements is useful for predicting the uniformity and thickness of the coating. Therefore, it can be concluded that the coatings are uneven and thin in the middle when the diameters are less than 2 mm, and after 2 mm, the coatings are thicker and more uniform.

In order to describe the distribution of coatings along the hole length, SEM morphologies of the polished cross-sections from the front edges, the middle parts and the back edges of the round PEO coatings from 0.5 mm to 6 mm are shown in Fig. 7.7, Fig. 7.8 and Fig. 7.9 respectively. In Fig. 7.7, when the diameter is 0.5 mm, there are thicker and thinner regions coexisting in the front edge of the hole. The thickest part is approaching 35 μm, while the thinnest part is merely 10 μm. In addition, there exists an evident crack between the coating and the substrate in Fig. 7.7(a), indicating the weak bonding strength between them. When the diameter is 1 mm, the coating at the front edge is still thick and the thickness is around 29 μm. From 2 mm to 6 mm, the coatings are getting thinner but more uniform, and their thicknesses are around 25 μm.

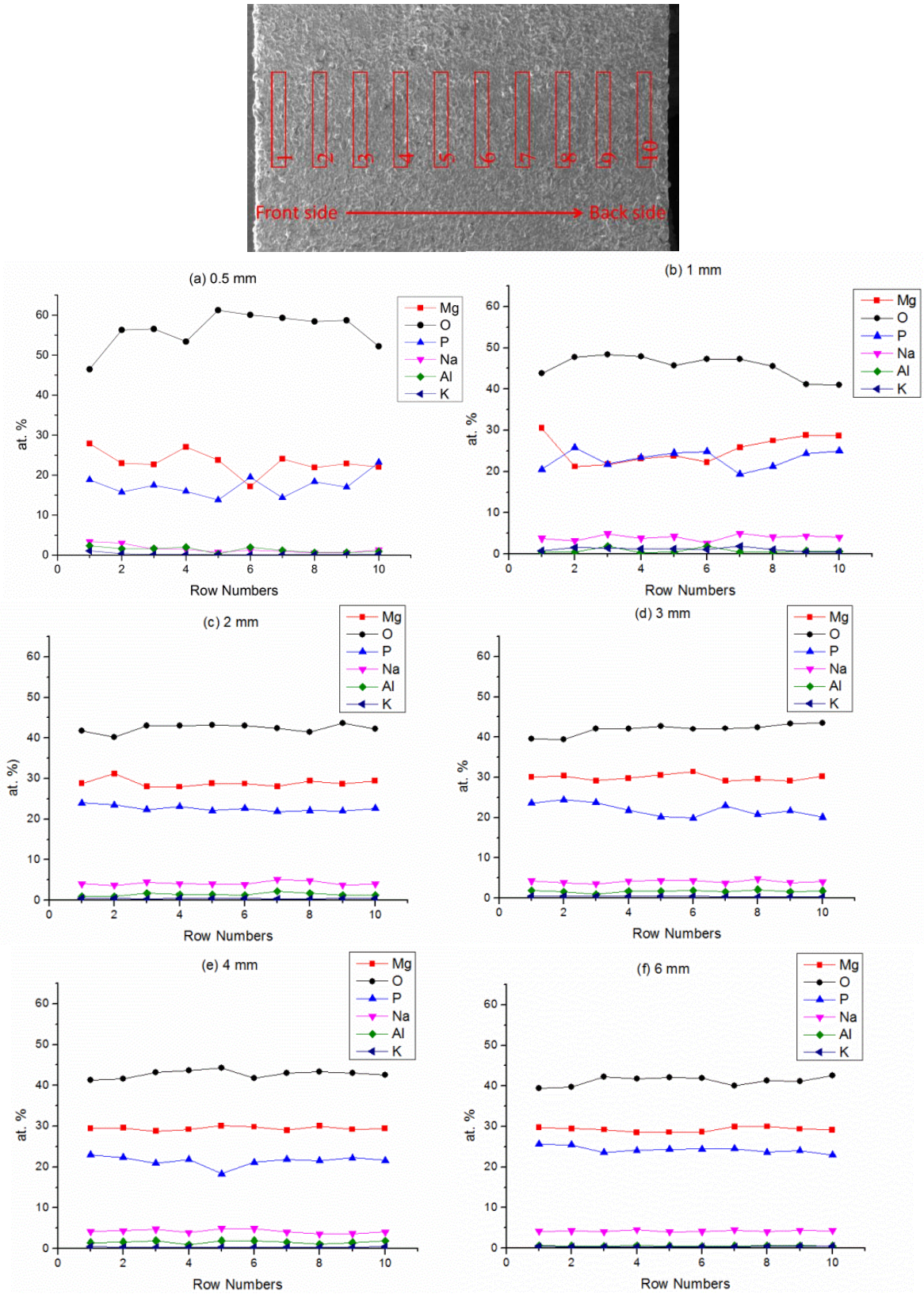

Fig. 7.6 Elements composition along the hole length detected from the round surfaces of PEO coatings by EDS for different diameters of holes.

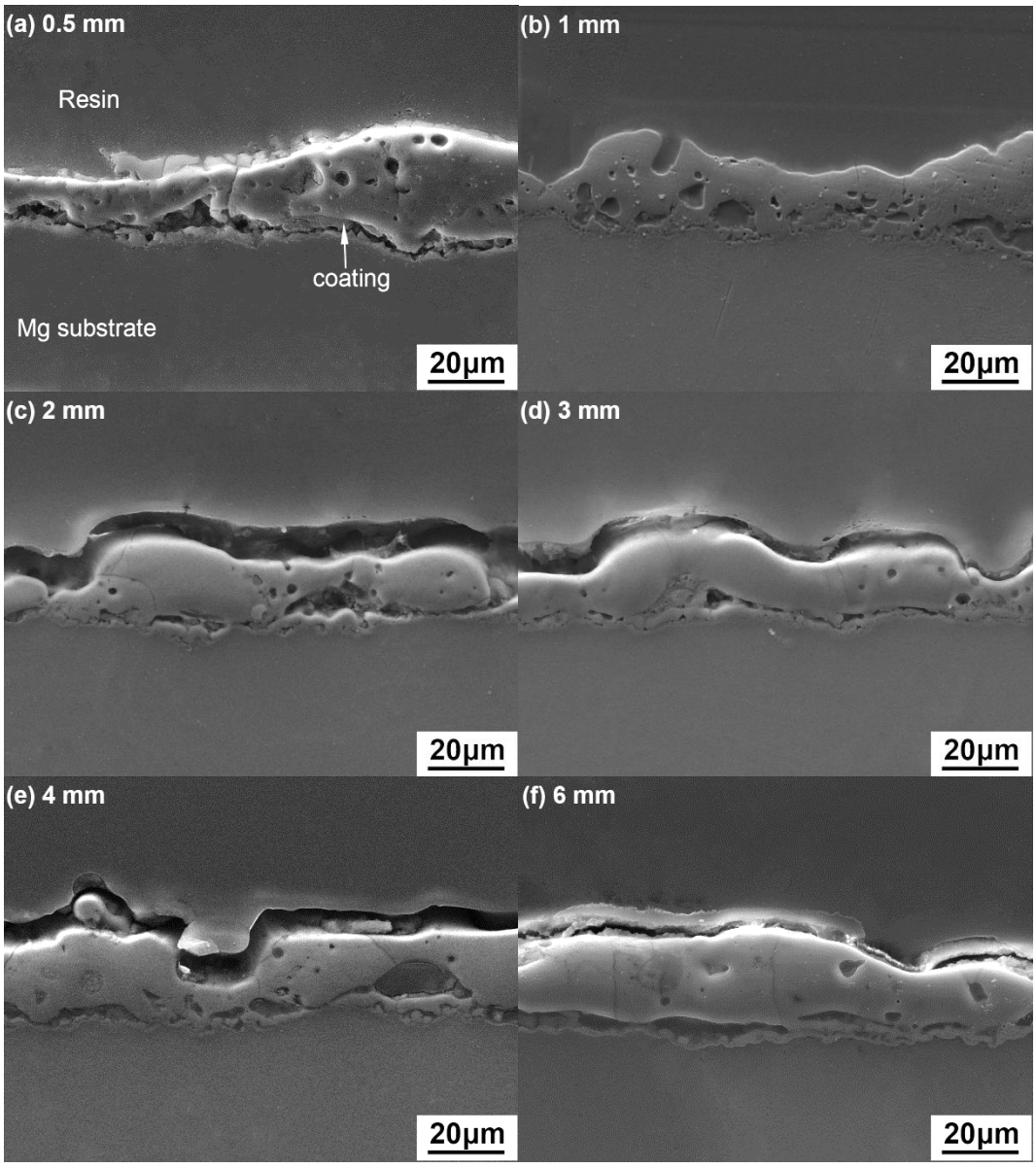

Fig. 7.7 SEM morphologies of the cross-sections from the edge part of the round PEO coatings.

In Fig. 7.8, the middle part of the coating in 0.5 mm hole is very thin, and the thickness is around 7 μm. When the diameter is 1 mm, the inner coating is porous but thicker than that in the 0.5 mm hole. From 2 mm to 6 mm, the coatings have typical PEO coating structure including the inner layer, pore band and outer porous layer, and are getting much thicker and more uniform. From 2 mm to 6 mm, the average thicknesses of the inner coatings in the middle parts are around 14 μm.

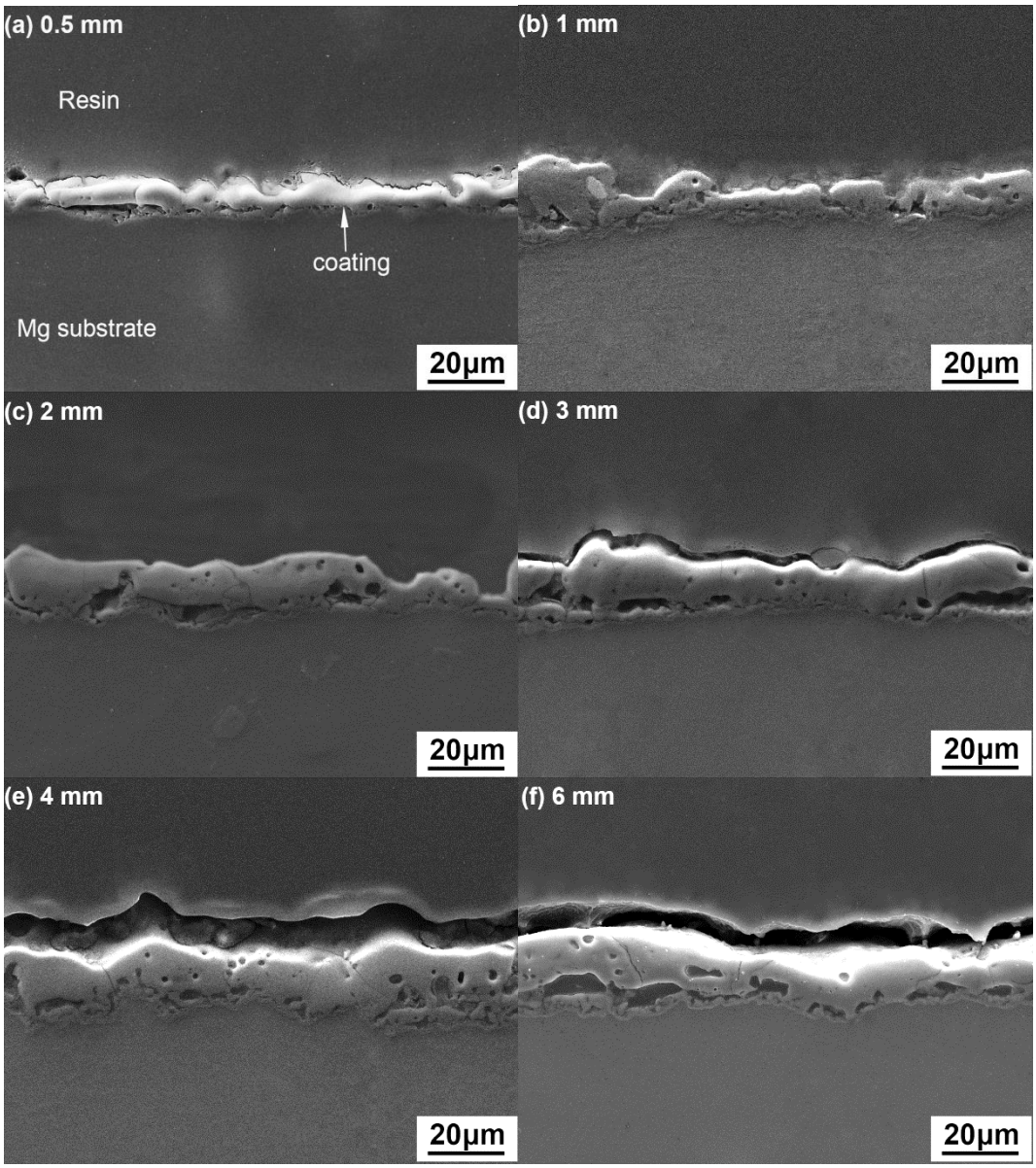

Fig. 7.8 SEM morphologies of the cross-sections from the middle parts of the round PEO coatings.

In Fig. 7.9, the coating on the back edge of the 0.5 mm hole is not compact because of the missing of the discharges, but its thickness is around 19 μm, higher than the other coatings with holes from 1 mm to 6 mm. But all the thicknesses of the coatings in the middle parts are smaller than that of the coatings on the edges, and the thickest coatings can be found at the front edges of the holes.

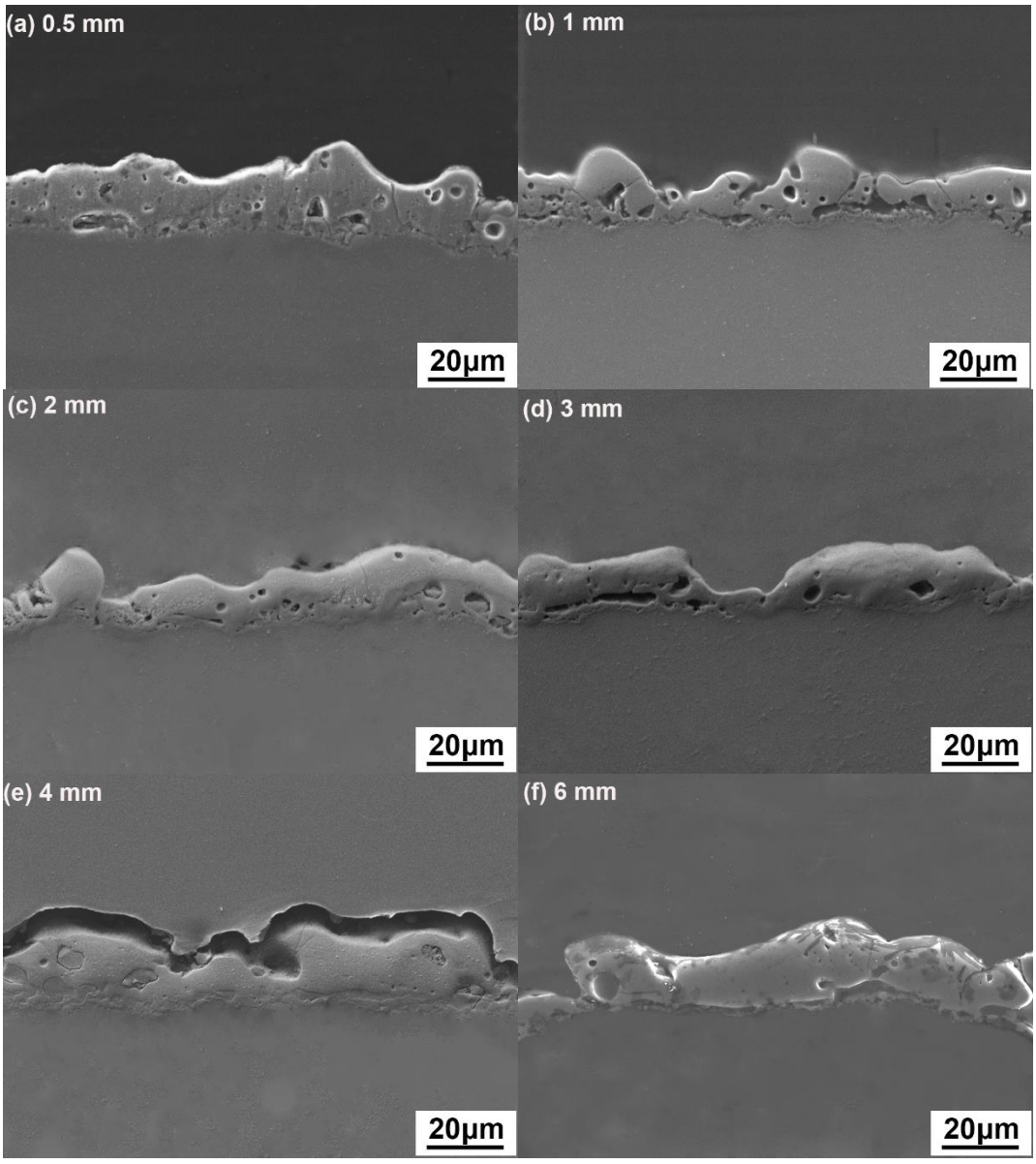

Fig. 7.9 SEM morphologies of the cross-sections from the back edges of the round PEO coatings.

To sum up, the experimental results demonstrate that the diameters of the holes in the substrates have little effect on the growth of the flat coatings or the round coatings when the holes are big, but they can change the morphologies, compositions, thicknesses and the distribution of the inner round coatings significantly when the diameters of the holes are smaller than 2 mm.

7.2 Modelling and simulation of substrate geometry impact

In order to study the PEO process at different locations of the anode, a 3D model in Fig. 7.10 is built based on the schematic representation of the experimental set-up for simulation in the present work. There are four domains in the model geometry. Domain 1 is the bulk electrolyte in the electrolyzer. Domain 2 is the cathode made of stainless steel. Domain 3 is the anode of

AM50 sample with predefined diameter of hole in the center. Domain 4 is the electrolyte inside the hole. The flat surface on anode reacts with the bulk electrolyte in domain 1 and the round surface inside the hole reacts with the electrolyte in domain 4. The details about modeling assumption and explanation of coating formation mechanics are the same as in chapter 4.6. However, in this study, it is possible that $Mg(OH)_2$ is formed instead of MgO inside the holes when the diameters of holes are less than 2 mm.

$$Mg^{2+} + 2OH^- \rightarrow Mg(OH)_2 + H_2O \qquad (7.2)$$

Two additional assumptions for this model are listed below:

1. Only crystalline phases of MgO and $Mg_3(PO_4)_2$ are considered as the composition of the PEO coating when the diameters of holes are bigger than 2 mm. Only crystalline phases of $Mg(OH)_2$ and $Mg_3(PO_4)_2$ are considered as the composition of the PEO coating inside the holes when the diameters of holes are less than 2 mm.
2. The transition time for formation of different phases in the coating is determined by the value of the potential drop across the coating which has to reach breakdown potential of 240 V. When the value of the potential drop across the coating is higher than 240 V, the phase formed in the coating is $Mg_3(PO_4)_2$. When it is less than 240 V, the phase is mainly MgO when the diameters of holes are bigger than 2 mm and the phase inside the holes are mainly $Mg(OH)_2$ when the diameters of holes are less than 2 mm.

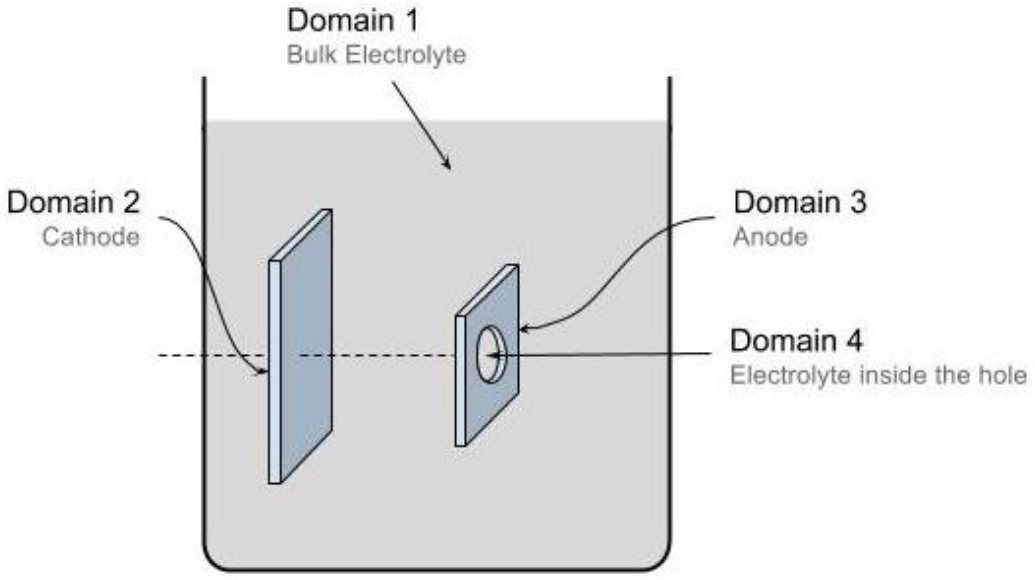

Fig. 7.10 Schematic diagram of the model geometry and the definition of the four domains.

This 3D model is an extension of the 2D model of coating growth in Chapter 5.2. The basic process and physical description of the modelling is the same compared to the 2D model except several equations. The different equations are listed below.

For each species *i* in the electrolyte of domain 1 and domain 4, the net ionic charge transport can be described below to replace Eq. (5.18) for this modelling:

$$N_i = \mathbf{u}c_i - z_i u_i F c_i \nabla \varphi_i - D_i \nabla \mathrm{c}_i \tag{7.3}$$

In domain 1, due to the electroneutrality condition, the assumption for the fluid flow vector of the bulk electrolyte is:

$$\mathbf{u} = \mathbf{0} \tag{7.4}$$

In domain 4, the flow in the holes is laminar. Therefore, the fluid flow vector of the electrolyte can be expressed by the Navier-Stokes equations:

$$\begin{gathered} \rho \cdot \frac{\delta \mathbf{u}}{\delta t} + \rho \mathbf{u} \cdot \nabla \mathbf{u} = \nabla \cdot \left[-p\mathbf{I} + \eta(\nabla \mathbf{u} + (\nabla \mathbf{u})^T) - \left(\frac{2\eta}{3}\right)(\nabla \cdot \mathbf{u})\mathbf{I} \right] \\ \frac{\delta \rho}{\delta t} + \nabla \cdot (\rho \mathbf{u}) = 0 \end{gathered} \tag{7.5}$$

where ρ denotes density (kg/m^3), $\mathbf{u}$ represents the velocity vector (m/s), η denotes viscosity (kg/(m·s)), $\mathbf{I}$ is the identity matrix, and p equals the pressure in the holes (Pa).

The boundary conditions for the holes are

$$\begin{aligned} \mathbf{u} \cdot \mathbf{n} &= v_o && \text{inlet} \\ \mathbf{u} &= 0 && \text{walls} \\ p &= p_{ref} && \text{outlet} \end{aligned} \tag{7.6}$$

$$\boldsymbol{v_0} = w \cdot d \tag{7.7}$$

where *d* is the diameter of the hole, *w* is a constant.

The calculated flow field serves as input to describe the convective mass transport in the holes.

Some additional equations are also listed as follow.

The concentration of the electrolyte at the flat surface of anode boundary is equal to the bulk concentration:

$$c_i = c_{b,i} \tag{7.8}$$

The potential drop over the coating film E_f including overpotential can be calculated by:

$$E_f = U - E_l - E_a \tag{7.9}$$

where U is the applied potential, E_l is the potential drop over electrolyte, E_a is the equilibrium potential.

However, the volume of the electrolyte inside the hole is limited, especially when the size of the hole is small. The changes of the ions in the electrolyte in domain 4 may result in different growth rate. Therefore, the solubility products and ion products of $Mg(OH)_2$ and $Mg_3(PO_4)_2$ have to be considered.

$$Q_{\mathrm{MgP}} = {c_{\mathrm{Mg2+}}}^3 \cdot {c_{\mathrm{PO3-}}}^2 \tag{7.10}$$

$$Q_{\mathrm{Mg(OH)2}} = c_{\mathrm{Mg2+}} \cdot {c_{\mathrm{OH-}}}^2 \tag{7.11}$$

c_{Mg2+}, c_{PO3-} and c_{OH-} are the concentrations of Mg^{2+}, PO_4^{3-}, and OH^- respectively. When the ion products of $Q_{\mathrm{Mg(OH)2}}$ and Q_{MgP} are lower than their solubility product $K_{sp(\mathrm{Mg(OH)2})}$ and $K_{sp(\mathrm{MgP})}$, magnesium oxide, magnesium hydroxide and magnesium phosphate are not able to form. The growth rate of each phase is determined as following:

$$v_{\mathrm{Mgo}} = \begin{cases} 0 \left(Q_{\mathrm{Mg(OH)2}} < K_{sp(\mathrm{Mg(OH)2})}\right) \\ r_{\mathrm{MgO}} \left(Q_{\mathrm{Mg(OH)2}} \geq K_{sp(\mathrm{Mg(OH)2})}\right) \end{cases} \tag{7.12}$$

$$v_{Mg(OH)2} = \begin{cases} 0 \left(Q_{\mathrm{Mg(OH)2}} < K_{sp(\mathrm{Mg(OH)2})}\right) \\ r_{Mg(OH)2} \left(Q_{\mathrm{Mg(OH)2}} \geq K_{sp(\mathrm{Mg(OH)2})}\right) \end{cases} \tag{7.13}$$

$$v_{\mathrm{Mgp}} = \begin{cases} 0 \left(Q_{\mathrm{MgP}} < K_{sp(\mathrm{MgP})}\right) \\ r_{Mgpo} \left(Q_{\mathrm{MgP}} \geq K_{sp(\mathrm{MgP})}\right) \end{cases} \tag{7.14}$$

where $K_{sp(Mg(OH)2)}$ and $K_{sp(MgP)}$ are the solubility products of $Mg(OH)_2$ and $Mg_3(PO_4)_2$ respectively.

When the diameters of holes are less than 2 mm, the total coating thickness L inside the holes can be calculated by:

$$L = L_0 + \int_0^{t0} v_{\mathrm{mg(oH)2}}\,\mathrm{d}t + \int_{t0}^{t} v_{\mathrm{mgp}}\,\mathrm{d}t \tag{7.15}$$

where t_0 is the time when the potential reaches to the breakdown voltage. When the diameters of holes are larger than 2 mm, the total coating thickness L can be calculated by:

$$L = L_0 + \int_0^{t0} v_{\mathrm{MgO}}\,\mathrm{d}t + \int_{t0}^{t} v_{\mathrm{Mgp}}\,\mathrm{d}t \tag{7.16}$$

The most important parameters being used for the computation are almost the same with that in Table 5.4 and Table 5.5 except that some parameters are different in Table 7.1. Combining all the parameters in Table 5.4, Table 5.5 and the values in Table 7.1, with the respective boundary conditions, the model is solved numerically via finite element method for time-dependent study in 10 min with a time stepping of 1 s using the commercial software COMSOL Multiphysics (version 4.4).

Table 7.1. Physical input parameters used in the numerical simulation

Physical parameter	Value	Unit
A	1.6e-2	A/cm^2
B	120	-
K	7.5e4	1/m
w	4π	rad
E_a	1.5	V
$M_{Mg(OH)2}$	58.3	g/mol
$\rho_{Mg(OH)2}$	2.34	g/cm^3
ρ	1.0	g/cm^3
η	1e-3	Pa·s
$Ksp_{(Mg(OH)2)}$	5.61e-12	M^3
$Ksp_{(MgP)}$	6.31e-25	M^5

7.3 Simulation results

The evolution of the average current density with time on the flat surfaces (a) and the round surfaces (b) are presented in Fig. 7.11. In Fig. 7.11(a), the simulated values of average current density on flat surfaces of different geometries show the identical evolution with time. They decrease with time in a similar way with the evolution of the total current density in Fig. 7.1(b) and the sizes of the holes do not have much influence on them. In Fig. 7.11(b), on the round surfaces, the evolutions of the average current density with diameters ranging from 2 mm to 6 mm are the same and their values are lower than that on the flat surfaces. But the average current density on the round surfaces in the holes with diameters of 0.5 mm and 1 mm change with time differently. Before they begin to decrease similarly with others, there is a time interval approx. 100 s and 11 s for holes with diameters of 0.5 mm and 1 mm separately that they decrease gradually with time in a linear way.

The dependence of the average potential drop including overpotential over both the flat surfaces (a) and the round surfaces (b) on the PEO processing time for samples with the diameters of holes ranging from 0.5 mm to 6 mm are presented in Fig. 7.12. The potential drop over the coating is calculated according to Eq. (7.9). On the flat surfaces, it increases over time rapidly from 250 V at 1 s and reaches approx. 350 V at the later stage of the processing time. The evolution is identical for each sample with different hole size, indicating the same growth rate of coatings. On the round surfaces, the potential drop also increases with time, but the increasing rate for each sample is different. The smaller the diameter is, the slower the increasing rate is. The potential drop through the coating is related to the discharges. When the potential difference is higher than the breakdown voltage 240, the discharges are possible to emerge. Therefore, for the coatings inside the holes, it takes at least 100 seconds for 0.5 mm sample, and 11 seconds for 1 mm sample and less than 4 seconds for samples from 2 mm to 6 mm to generate the plasma discharges. But for coatings on the flat surfaces, after 1 s, plasma discharges begin to show, which is in accordance with the experimental observation.

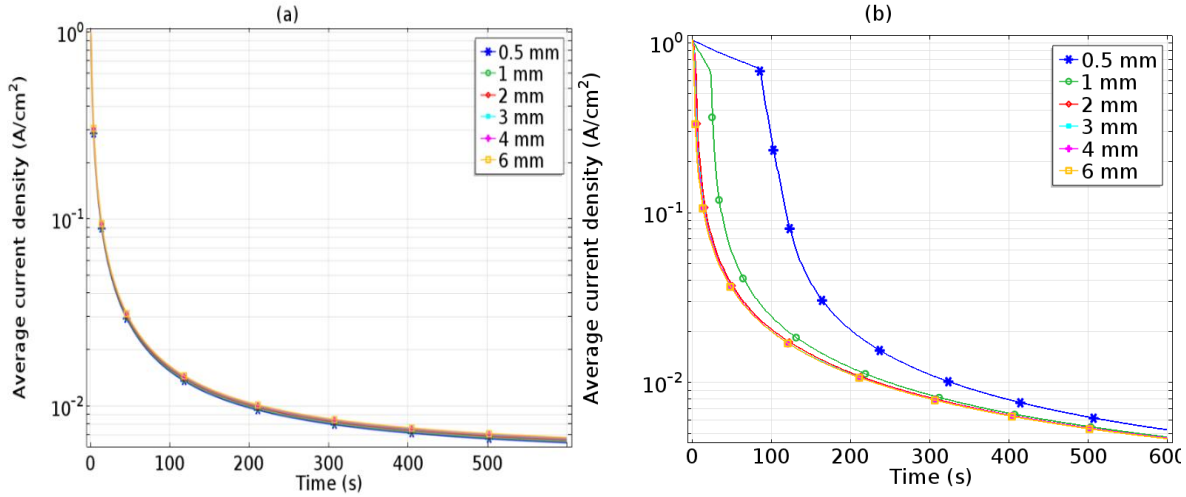

Fig. 7.11 The evolution of average current density on the round surfaces and flat surfaces of anode samples vs. time calculated from the modelling in 10 min.

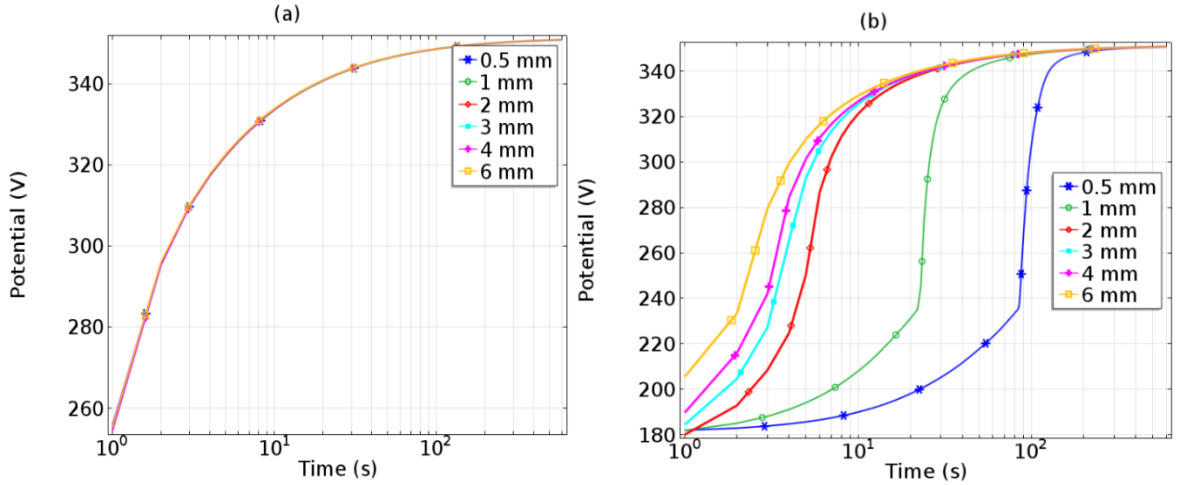

Fig. 7.12 The dependence of potential drop including overpotential over both flat surfaces (a) and round surfaces (b) on the PEO processing time for samples with diameters of holes from 0.5 mm to 6 mm.

Fig. 7.13 shows the simulated changes of average concentrations of OH^- and PO_4^{3-} both in the bulk electrolyte (a and b) and the electrolyte inside the holes (c and d) over time. The decrease of PO_4^{3-} concentration is a result of the formation of $Mg_3(PO_4)_2$ phase in the coating. OH^- is consumed by both oxygen release and the formation of MgO or $Mg(OH)_2$ in the coating. It is clear that the changing hole size in the range of 0.5 mm to 6 mm does not affect the concentrations of PO_4^{3-} and OH^- in the bulk electrolyte, and after 10 min PEO processing, the changes of PO_4^{3-} and OH^- in the bulk electrolyte are inconspicuous. However, in the holes, the concentrations of OH^- and PO_4^{3-} show quite different evolution compared to the bulk electrolyte. The initial concentration of OH^- is 29.2 mol/m^3 for all the conditions. Then in the

first second, the concentration of OH^- decreases rapidly. For the holes with sizes of 0.5 mm, 1 mm, and 2 mm, the concentration of OH^- decreases almost to 0, which means the electrolyte is limited. Then with increasing time, the concentration of OH^- increases gradually due to the supplement of electrolyte from the container. It takes much longer time to recover the concentration of OH^- when the hole size is smaller. For the smallest hole with 0.5 mm diameter, it takes almost 100 s, but for the 6 mm hole, it takes less than 1 s. The final concentration values of OH^- in the holes are lower than that in the bulk electrolyte and the smaller the hole is the lower the concentration is. Fig.7.13(d) shows the evolution of the concentration of PO_4^{3-} in the holes. The initial concentration of PO_4^{3-} is 61 mol/m^3. Different from the evolution of OH^-, the concentration of PO_4^{3-} keeps constant for a while before it begins to decrease because the PO_4^{3-} is consumed by formation of $Mg_3(PO_4)_2$ at the later stage. The time interval is determined by the potential drop reaching breakdown potential and it decreases with increasing hole size. After that the concentration decrease rapidly due to the high reaction rate of $Mg_3(PO_4)_2$ and then increase because of the decreasing reaction rate and the supplement from the bulk electrolyte. The concentrations of PO_4^{3-} in the hole with diameter of 0.5 mm decreases to approx. 0 and remain for several seconds, indicating the shortage of ions in the electrolyte may restrict the coating formation reaction.

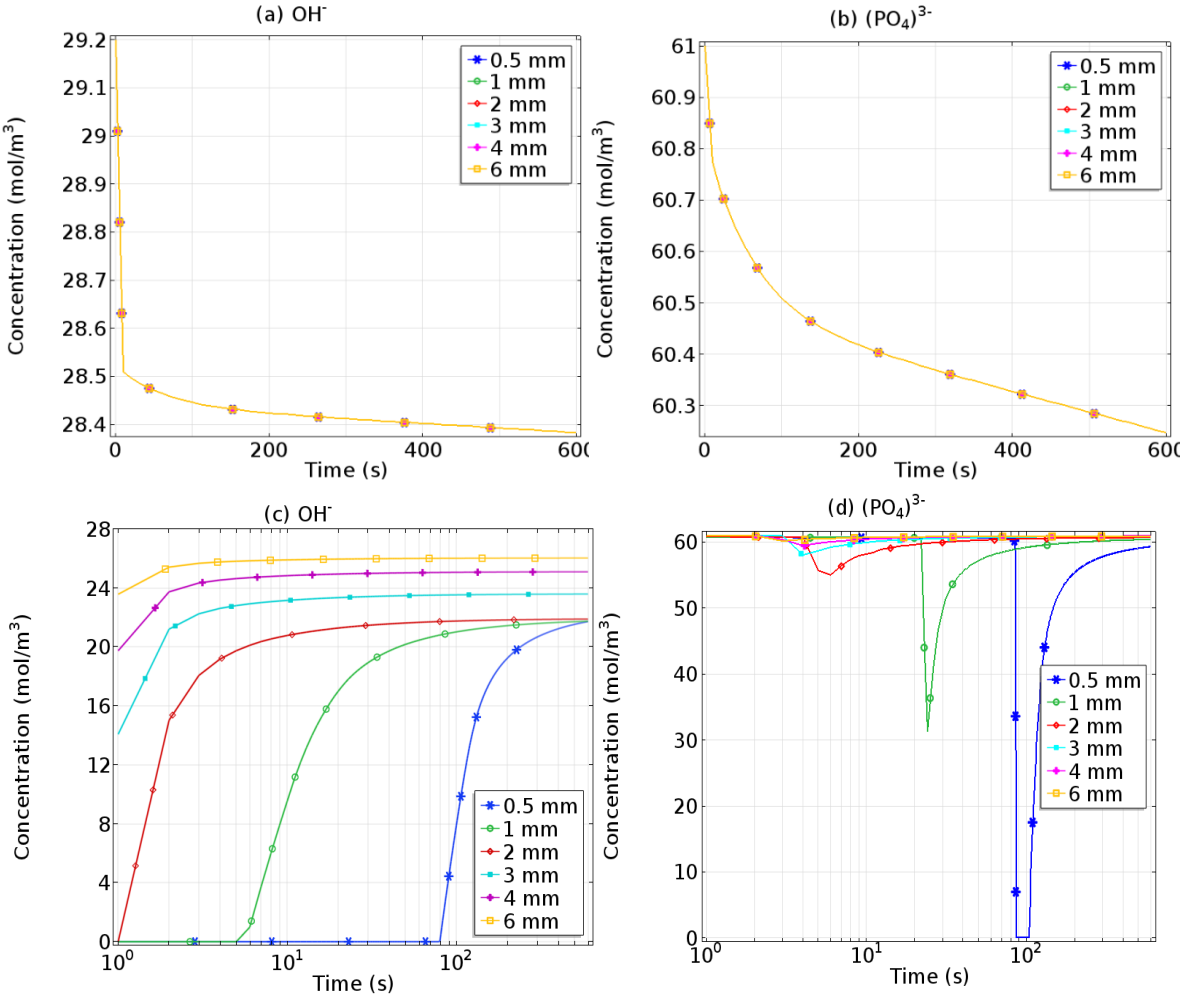

Fig. 7.13 Simulation results of average concentrations of OH^- and PO_4^{3-} both in the bulk electrolyte (a and b) and the electrolyte inside the holes (c and d) over time.

Fig. 7.14 displays the evolution of average coating thickness with time on the flat surfaces (a) and round surfaces (b) of samples with diameters of holes ranging from 0.5 mm to 6 mm. As expected, the coatings show the same evolution of thickness on the flat surfaces. The average coating thickness increases gradually with time and the final thickness is around 16.5 µm for each sample, which is in agreement with the experimental values. On the round surfaces, the evolution of the coating thickness for samples with holes larger than 2 mm are similar with that on flat surfaces, and their final coating thickness are around 14.5 µm. When the holes are smaller than 1 mm, the evolution of average coating thickness is significantly different. The thickness increases linearly with time by a low growth rate in the first period of time that lasts for approx. 100 s and 10 s for 0.5 mm and 1 mm samples respectively, and then it increases gradually in the same manner of the outer coating thickness till the end of the processing time. The final coating thicknesses of 0.5 mm and 1 mm samples are 12.7 µm and 13.4 µm respectively.

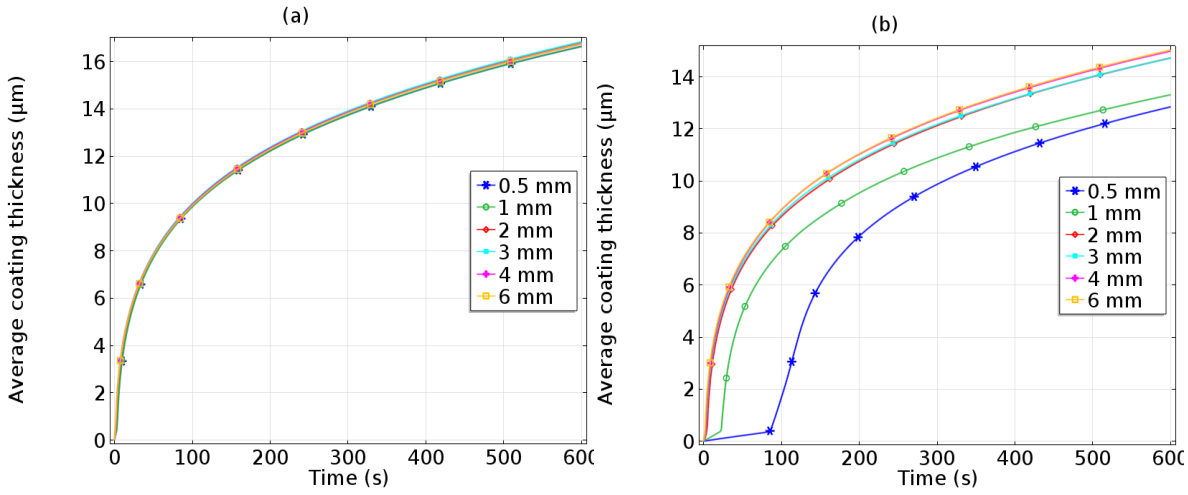

Fig. 7.14 Evolution of average coating thickness on flat surfaces (a) and round surfaces (b) of the samples with diameters of the holes ranging from 0.5 mm to 6 mm.

Fig. 7.15 illustrates how the geometry affect the pore coverage ratio at the flat surfaces (a) and the round surfaces (b). The simulation results show that the pore coverage ratio on flat surfaces is a little bit higher as compared to the round surfaces. The changing geometry does not alter the evolution of the pores on flat surfaces and round surfaces with holes larger than 2 mm. The pore coverage ratio drops down rapidly at the early stage of the PEO processing and then increases slowly till the end. When the diameters of holes are 0.5 mm and 1 mm, there are no discharges generated at the initial stage because breakdown voltage is not reached. After 200 s and 50 s for samples with 0.5 mm and 1 mm holes respectively, the pore coverage ratio increases gradually with time. Nevertheless, the values are less than 0.3 %, so the plasma discharges in both holes are very rare.

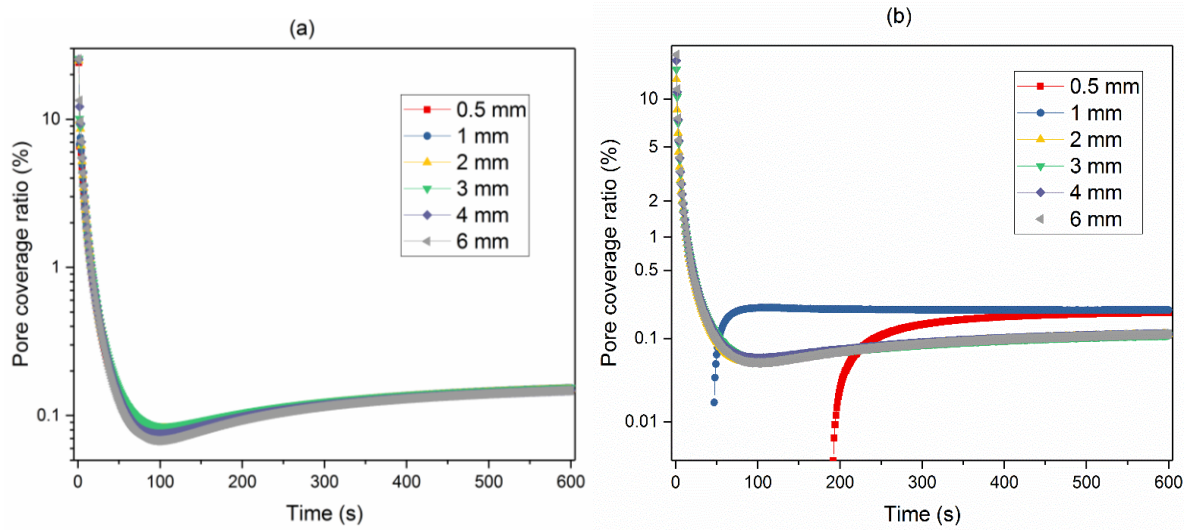

Fig. 7.15 Evolution of pore coverage ratio with time on flat surfaces (a) and round surfaces (b) of samples with diameters of holes ranging from 0.5 mm to 6 mm.

Fig. 7.16 presents the simulation results of concentration distribution of OH^- along the length of the different holes at different times. The concentration of OH^- in the middle parts of the holes are lower compared to the edge parts which can be attributed to the diffusion, convection and migration of ions in the bulk electrolyte from both edges to the center of the holes. At each second, the concentration in the smallest hole is the lowest, and with the increase of hole size, the concentration gets higher and higher, especially for the first second. At the first second, the lowest concentration reaches to approx. 0 mol/m^3 inside 0.5 mm hole, and it takes more than 90 s to recover back. In 1 mm hole it takes 10 s, and in 2 mm and 3 mm hole, it takes less than 2 s to recover back to more than 0 mol/m^3. For 4 mm and 6 mm holes, the concentration stays more than 8 mol/m^3. The values of ion concentrations in the small holes indicate that the electrochemical reactions happening on the round surfaces do not comply with that on the flat surfaces for the samples with diameters of holes below 2 mm because of shortage of the electrolyte.

The simulation results of concentration distribution of PO_4^{3-} along the hole length are almost the same with the distribution of OH^- except that the values are more positive, so it is not necessary to show the results for concentration distribution of PO_4^{3-} in this study.

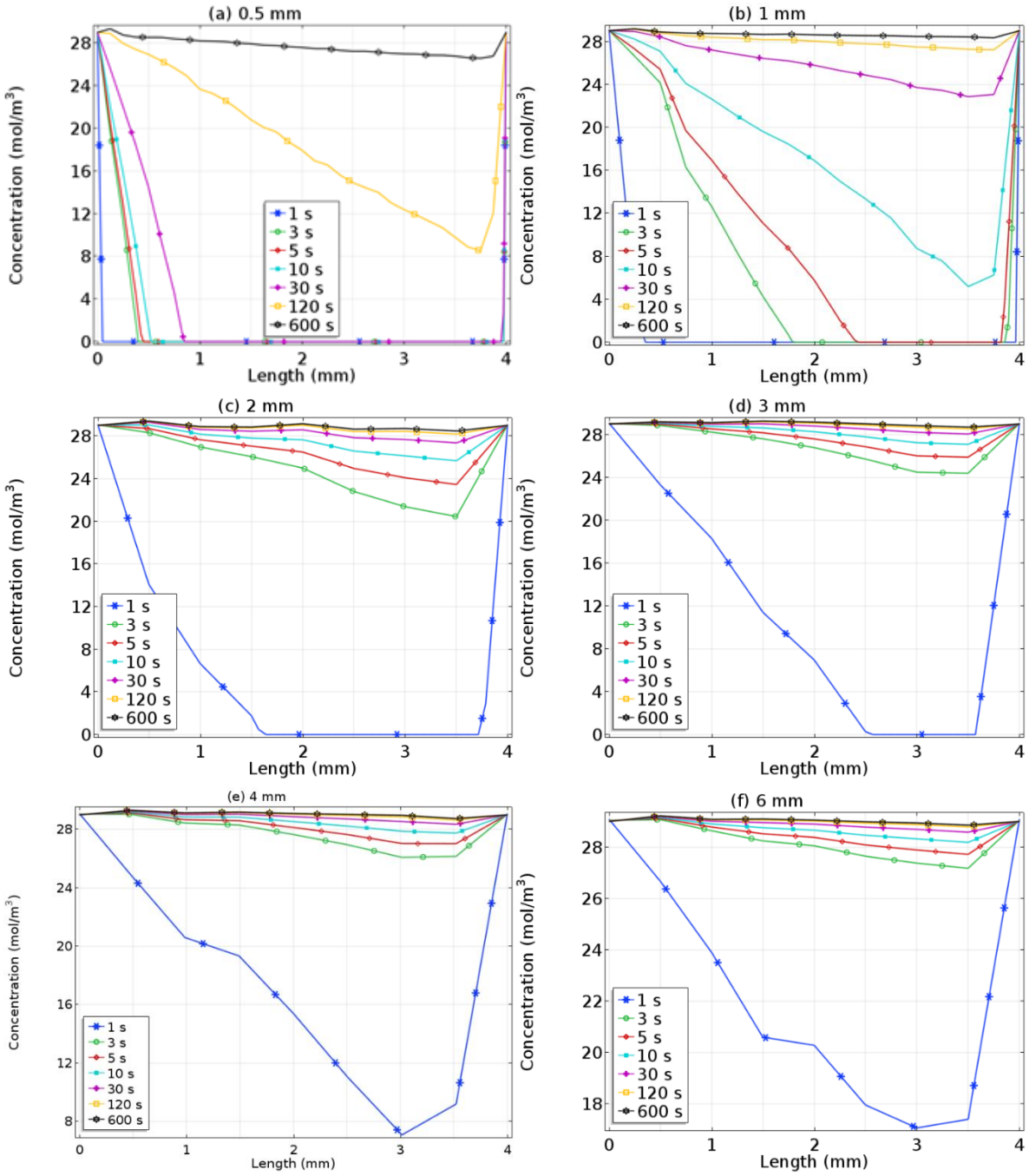

Fig. 7.16 Time dependence of OH^- concentration distribution along the length of round surfaces inside the holes with diameters ranging from 0.5 mm to 6 mm.

In order to discover how the current distributes along the length of the round surface, the same position of the line shown in blue in Fig. 3.3 at the top of the hole is selected from the front side to the back side. The simulation results of current distribution for different holes at different times are shown in Fig. 7.17. For each sample, the current density decreases along the length from the front side to the back side at any moment. When the diameter is 0.5 mm, the current density decreases rapidly near both edges but keeps stable in the middle part. As the

diameter reaches to 1 mm, the decrease of current density at both edges becomes less steeper. From 2 mm to 6 mm, the current density decreases gradually over the length and the distribution of current density shows no significant difference between those samples. Moreover, the highest value of current density is found for the front side of 0.5 mm hole.

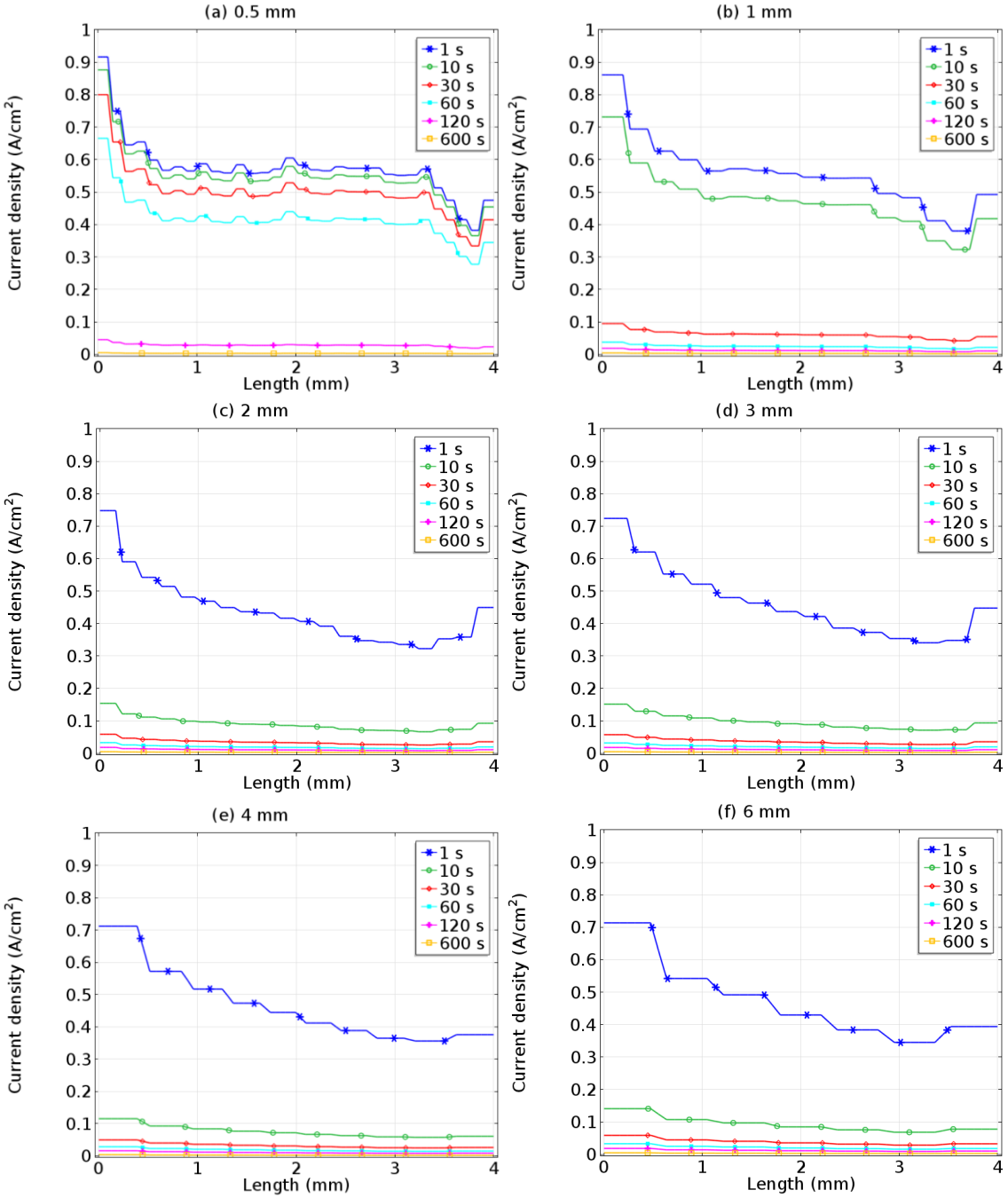

Fig. 7.17 The simulated distribution of current density along the length of the hole from the front side to the back side for each sample with hole diameter from 0.5 mm to 6 mm.

Since it is difficult to measure the average coating thickness inside the holes statistically by experiment, the line near the place where we show the cross-sections in Fig.7.7, Fig.7.8 and

Fig.7.9 is selected to show the distribution of coating thickness along the length of the hole from the front side to the back side for each sample. The simulation results at different times are shown in Fig.7.18. For the round coating inside the hole with 0.5 mm diameter, there is a time interval around 100 s during which the coating formation is slowed down, leading to a thinner coating in most of the hole. The same situation happens to the hole with 1 mm diameter, and the time interval is at least 10 s. But both coatings grow quickly after 120 s and 30 s respectively. At the end of processing time, the distribution of thickness for 0.5 mm is obviously different from the others with rapid decrease of coating thickness at both edges and the quite thin and uniform thickness in the middle of the coating, and the highest value at the front side is approx. 32 μm and the lowest value is approx. 8 μm in the middle part. The final coating thickness at each point of the round surface for 1 mm sample also decreases from the front side to the back side, and coating thickness in the middle is around 12 μm, thicker than that of the 0.5 mm hole.

For the other holes with diameters from 2 mm to 6 mm, the time intervals are 2 to 4 s. The thickness at each point increases with time but the growth rate decreases from the front side to the back side gradually for each sample, and after 10 min, the distributions of coating thickness between those samples do not have much difference, with around 22 μm at the front side and around 14 μm in the middle part. At the front edge of each hole, the current density is the highest, and the supplement of the electrolyte is faster than the middle part, so the coating at the edge is much thicker than that in the middle part. The simulation results show that the current density at the front edge of 0.5 mm hole is the highest, hence the coating at this part is correspondingly the thickest. In comparison, the simulation results are in good agreement with the experimental results of coating thickness distribution in Fig.7.7, Fig.7.8 and Fig.7.9. From the distribution of current density and ion concentration, it is concluded that when the electrolyte is sufficient, current density is the main factor that influence the coating growth, and when the electrolyte is deficient, the concentration of ions controls the growth of PEO coating.

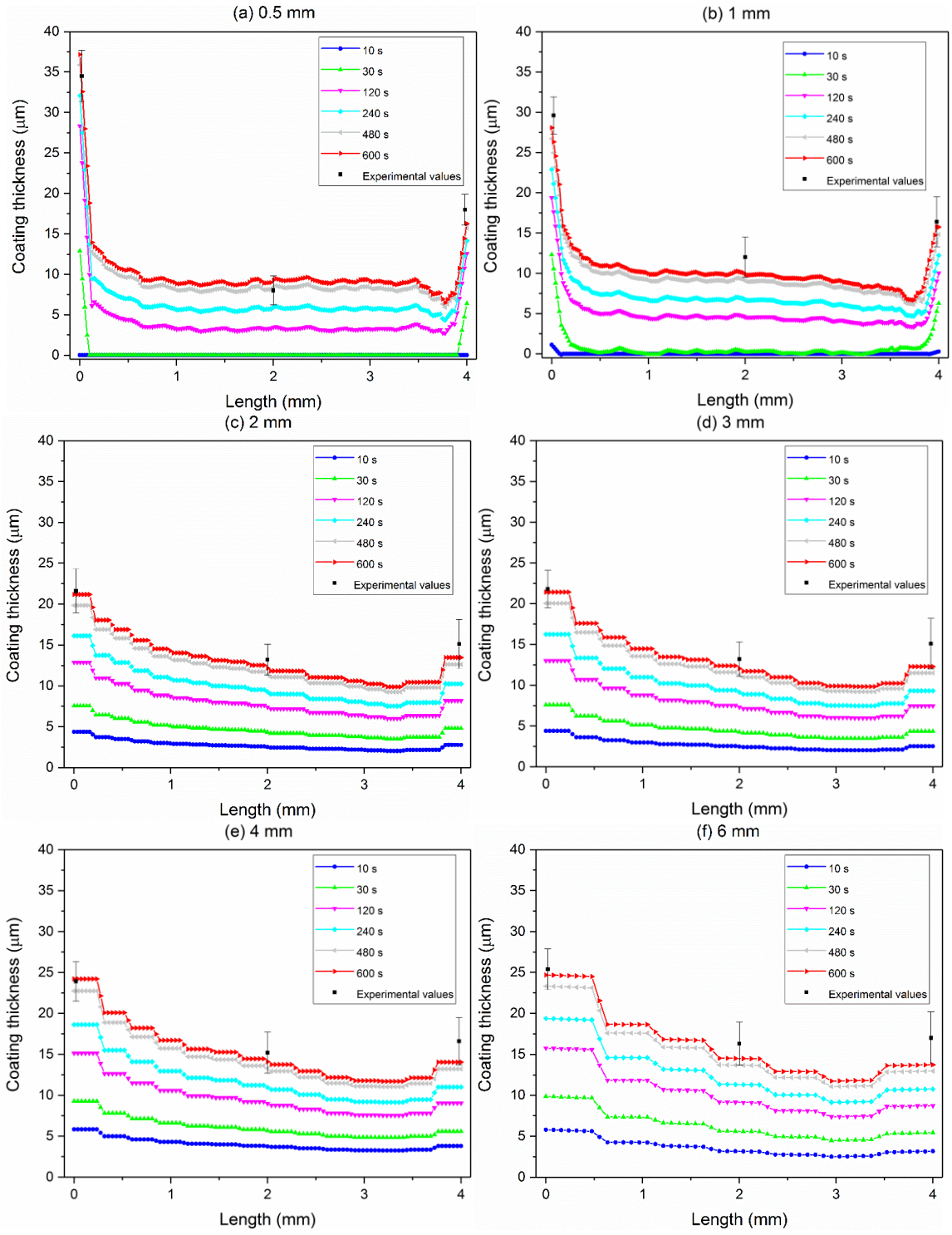

Fig.7.18 The simulated distribution of coating thickness along the length of the hole from the front side to the back side for each sample with hole diameter from 0.5 mm to 6 mm, and the experimental thickness at three locations of each coating after 10 min PEO processing.

7.4 Discussion

In the present study, the geometry of the substrate is separated mainly into two parts, the flat surface and the round surface. The coating growth on both the flat and round surfaces result from the reactions of the substrate with the electrolyte in domain 1 and domain 4 respectively under constant voltage mode. The experimentally measured conductivity in bulk electrolyte after the 10 min PEO processing is almost the same as the one measured before, and the pH values decrease only by 0.05 after 10 min. Therefore, in the modelling, we assume that the magnesium ions generated on the flat surface will react completely with the bulk electrolyte. Over the total PEO processing time, the simulated concentrations of both OH^- and PO_4^{3-} ions in bulk electrolyte show little changes after 10 min. The changing sizes of the holes have barely influence on the simulation results of the average current density and the potential drop over the coating on the flat surfaces, which generates the same growth rate of the PEO coatings. Therefore, the assumptions of the mechanism on the flat surface hold true for the calculation of current distribution and coating thickness, and the coating characterization and the measured coating thickness from the experiment on flat surfaces are identical after the same PEO processing even though the sizes of the holes change from 0.5 mm to 6 mm.

However, the coatings inside the holes are affected by the changing size of the holes. The main factors that influence the quality of the formed PEO coating are the processing parameters, such as the applied potential, the applied current density, the treatment time, the substrate properties, electrode geometry, nature and additives of the electrolyte, and flow dynamics [137]. In this study, the changing geometry leads to different volumes of electrolyte inside the holes. When the diameters range from 0.5 mm and 1 mm, due to their small amount of electrolyte inside the holes, the evolutions of the concentration of ions inside the holes, the average current density, the potential drop, the coating thickness and the pore coverage ratio differ greatly from those with hole diameters more than 2 mm. At the initial stage, the formation of the oxide products demands a large amount of OH^- in the electrolyte. The simulation results show that the amount of OH^- in the middle parts of the small holes decreases rapidly to 0 especially when the size of the holes are small, indicating that the electrolyte inside the holes is not enough for the coating growth on the round surfaces. The deficiency of electrolyte restrains the growth of coatings and thus slows down the decrease of current density and the increase of voltage drop across the coatings. Before the voltage drop reaches 240 V, no plasma is formed and the process is similar to conventional anodization. The duration of conventional anodization for coatings

inside the 0.5 mm and 1 mm holes are about 90 s and 11 s respectively, which are much longer than those inside the holes with diameters more than 2 mm. The properties of the electrolyte in holes may change sharply, pH for example. The consumption of OH^- may lead to acidification of the electrolyte, then in such a condition, magnesium hydroxide and magnesium phosphate can not form, and most of the substrate may dissolve in the electrolyte in the form of Mg^{2+} instead. Therefore, the Mg contents of the ceramic coating in the middle parts of the small holes with diameters of 0.5 mm and 1 mm are lower than that of the other coatings, and the formation mechanism for the coatings is different from what we have observed from experiments on flat surfaces. Then after the potential drop reaches 240 V, plasma discharges associated oxidation enables the fast growth of PEO coatings and leads to a rapid decrease of current density and increase of potential drop. Even though there are plasma discharges generated at the later stage of the PEO processing inside the smallest hole, the shorter duration and low ratio of the discharges can barely condense the coating, leading to loose conversion products on the surfaces of the holes. The plasma discharge in the hole with 1 mm diameter lasts longer and its ratio is higher as compared to the smallest hole. Thus, it is possible to condense some conversion products. The coating is a mixture of some typical PEO structures and conversion products. The final coating thickness is determined by both the concentration of the ions and the current distribution inside the holes. The current density and the concentration of ions at the edges are higher compared to the middle, resulting in thick coatings at both edges and thin coating in the middle of the holes.

For samples with diameters ranging from 2 mm to 6 mm, their relatively large volumes of electrolyte inside the holes guarantee a fast supply of the ions for the chemical reactions. Even though the concentrations of OH^- in the middle of the holes with diameters of 2 mm and 3 mm decrease to approx. 0 in the first second, they recover in less than 2 s. Therefore, the PEO coatings still grow fast from the initial stage, and the values of current density decreases and the values of voltage drop over the PEO film increases rapidly from the beginning of PEO treatment, which complies with the typical features of current and voltage evolution under constant voltage mode. The distribution of their final coating thicknesses is determined mainly by the distribution of the current density. Also, the coating thickness on round surface within 2 mm and 3 mm holes are thinner than that with larger holes due to the postponement of coating growth in the first seconds by the shortage of electrolyte.

From the results above, it is concluded that when the electrolyte is sufficient, current density is the main factor that influence the coating growth, but when the electrolyte is deficient, the concentration of ions controls the growth of PEO coating.

7.5 Summary

In this study, the substrate geometry refers to a rectangular sample of magnesium alloy AM50 with a hole of defined diameter in the center. The impact of substrate geometry on PEO coatings at different locations are studied by both experiments and simulation. The following conclusions can be drown:

1. The experimental results demonstrate that the size of the holes barely has influence on the flat coatings, but it does have a significant influence on the inner round coatings when the diameters of the holes are small.

2. When the diameters of the holes are larger than 2 mm, the morphology, composition and thickness of the inner coatings are similar to that formed on the flat coatings. But when the diameters of the holes are less than 2 mm, the morphology, composition and thickness of the inner coatings differ from their corresponding flat coatings greatly. The morphologies of the coatings are loose and have only few typical PEO coating features, and most of the coatings are composed of conversion products. The contents of Mg element in those coatings are lower compared to coatings with larger diameters of holes. The distribution of the elements along the length of the holes are fluctuant and thus the distribution of the coating thicknesses are not uniform. The coatings at the edges are very thick while the coatings in the middle of the hole length are very thin.

3. Different mechanism of coating formation at flat coatings and round coatings have to be considered when applying the PEO coating growth model to study the geometry impact on the PEO coating. Modeling and simulation reproduce the PEO process on both outer flat surface and inner round surface of magnesium AM50 alloy reasonably well. The simulation results show that the size of holes has little influence on the flat coatings which is in accordance with the experimental results, but inside the holes, the coating thickness of the round surfaces are strongly affected especially when the diameters of the holes are smaller than 2 mm. In addition, the simulation results reveal that the shortage of electrolyte is the main reason that affects the growth of the coating

and thus the composition and morphology of the coating inside the holes, and the final simulation results of the coating thickness are in good agreement with experimental values.

Therefore, it is concluded that substrate geometry indeed has impact on PEO coating growth under constant voltage mode because of the different current distribution and evolution and the constraint of the electrolyte at different locations. Meanwhile, modeling and simulation have proved to be a useful tool to help understand and predict the PEO process reasonably.

8. Conclusions and outlook

8.1 Conclusions

The present work has studied the growth of PEO coatings with time and then developed a time-dependent model to simulate the PEO process numerically based on the current understanding of the PEO process by finite element method in COMSOL. The model has been verified by comparing the experimental results with the simulation results. Moreover, a numerical model has been applied to study the effects of the substrate geometry and the electrode distance on the formation of the PEO coatings under constant voltage mode. The overall conclusions are listed as follow:

1. According to the PEO growth model, the average coating thickness is a function of coating formation current density, phase composition and coating porosity. The outcome of the simulation is finally quite close to what we see in the experiment. The simulation result of the average coating thickness evolution over time is in good agreement with experimental values. The simulated number of discharges decreases rapidly with time, which is consistent with the experimental observation. Even though the pores generated by the discharges are lower than the experimental result, the same evolution tendency may indicate the correctness of the model concept.
2. Effect of substrate geometry on PEO coating formation

   The substrate geometries refer to the rectangular samples with holes of different diameters in the centers. The experimental study proves that the changing sizes of holes affect the morphologies, phase composition and thickness of coatings in the holes greatly. The modeling and simulation demonstrates that the constraint of the electrolyte in the holes and the different current distribution and evolution at different substrate locations are the main reasons for the impact of substrate geometry on PEO coating growth under constant voltage mode. The simulated coating thickness is consistent with the experimental results.

3. Effect of electrode distance on PEO coating formation

   The experimental results show that electrode distance between the anode and the cathode has impact on the PEO coating morphologies and thicknesses. With increasing electrode distance, the coating thickness decreases gradually and the coating roughness and resistance change fluctuant. An optimized electrode distance of 80 mm is identified

under the current experimental condition. By the complementary modeling and simulation, the electrode distance is also proved to be an important factor that can alter the current distribution and evolution on the surface of the alloys under constant voltage mode thus influencing PEO coating growth such as morphology and thickness.

4. The application of the modeling of the PEO process

   The effects of treatment time, substrate geometry and electrode distance on the PEO coating formation has been studied experimentally and numerically. By comparing the experimental results and the simulation results, the model has been proved useful and is capable of explaining the effects of different parameters on the coating formation and predicting the coating thickness. Therefore, this model of the PEO process provides a methodology to study the coating formation under constant voltage mode and can be used for industrial application even when the geometry of the sample or the cell is complicated.

   According to the experience from above studies, when the model is adapted to another experimental condition, the most important steps the performers need to do include:

   1. changing the values of the parameter or/and redefining the geometry for a certain condition;

   2. performing the PEO process and recording the evolution of the current and voltage;

   3. fitting the current and employing the fitted equation for the kinetics of the PEO process;

   4. re-computing the model to get the results.

8.2 Outlook

The simulation of the PEO process under constant voltage mode has been proved feasible in the respect of predicting coating thickness. It is useful and time-saving to study the PEO process when some parameters such as the voltage, the concentration of the electrolyte, the electrode distance and the substrate geometry are changed seperately or simultaneously. The next step of this work is to associate the coating features such as the pores, the thickness with the coating properties and specifically the corrosion resistance. Therefore, the experimental

parameters can be related to the properties of the coating. At this stage, this simulation can be a tool for better experimental design.

The limitations of the model have to be mentioned in more details. First, this model takes the growth mechanism of coating into account without thermal diffusion, so it is feasible for short treatment of PEO. However, with longer treatment time, oxygen diffusion has to be considered because it is the main process that controls the coating growth [138-140]. Second, the complexity of PEO mainly lies in the mechanism of the discharges phenomena occurring during the process. It is difficult to study the microdischarges unless different research methods are applied conjointly. In this study, the simplication of the discharge mechanism is one of the main reasons which result in the inaccurate results of pores and pH values. From the results of this work, effects of predicting the current distribution and coating thickness events of PEO process have become clear. However, to completely understand the characteristics of the PEO process, the investigation needs to continue with more details of simulation and different experimental designs involving other research methods and instruments such as high speed video imaging and the small area current monitoring technique [141-143].

9. Reference

[1] K. Funatani, Emerging technology in surface modification of light metals. Surf. Coat. Technol., 133 (2000), pp. 264-272.

[2] H. Somekawa, A. Kinoshita, K. Washio, A. Kato, Enhancement of room temperature stretch formability via grain boundary sliding in magnesium alloy. Mater. Sci. Eng. A, 676 (2016), pp. 427-433.

[3] Y. Liu, X. Yin, J. Zhang, S. Yu, Z. Han, L. Ren, A electro-deposition process for fabrication of biomimetic super-hydrophobic surface and its corrosion resistance on magnesium alloy. Electrochimica Acta, 125 (2014), pp. 395-403.

[4] H.Y. Wang, W. Wang, M. Zha, N. Zheng, Z.H. Gu, D. Li, Influence of the amount of KBF4 on the morphology of Mg2Si in Mg-5Si alloys. Mater. Chem. Phys., 108 (2008), pp. 353-358.

[5] J. E. Gray, B. Luan, Protective coatings on magnesium and its alloys—a critical review. J. Alloys. Compd., 336 (2002), pp. 88-113.

[6] A. Kuhn, Plasma anodizing of magnesium alloys. Metal Finishing, 101 (2003), pp. 44-50.

[7] G. Zhao, J. Zhao, Surface modification of die casting mold steel by a composite technique of hot-dipping and plasma electrolytic oxidation. Rare Metals, 31 (2012), pp. 362-367.

[8] F. Xu, Y. Xia, G. Li, The mechanism of PEO process on Al–Si alloys with the bulk primary silicon. Appl. Surf. Sci., 255 (2009), pp. 9531-9538.

[9] S. Montisci, Surface technologies show the way for magnesium, Mater. World, 24 (2016) pp. 27-29.

[10] E. Cakmak, K. C. Tekin, U. Malayoglu, S. Shrestha, The effect of substrate composition on the electrochemical and mechanical properties of PEO coatings on Mg alloys. Surf. Coat. Technol., 204 (2010), pp. 1305-1313.

[11] R.O. Hussein, D.O. Northwood, X. Nie, The effect of processing parameters and substrate composition on the corrosion resistance of plasma electrolytic oxidation (PEO) coated magnesium alloys. Surf. Coat. Technol., 237 (2013), pp. 357-368.

[12] C. Liang, In-situ Impedance Spectroscopy Studies of the Plasma Electrolytic Oxidation Coating Process. Diss. University of Sheffield, 2013.

[13] L. O. Snizhko, A. L. Yerokhin, A. Pilkington, N. L. Gurevina, D. O. Misnyankin, A. Leyland, Anodic processes in plasma electrolytic oxidation of aluminium in alkaline solutions. Electrochim. Acta, 49 (2004), pp. 2085-2095.

[14] R.O. Hussein, X. Nie, D.O. Northwood, A. Yerokhin, A. Matthews, Spectroscopic study of electrolytic plasma and discharging behaviour during the plasma electrolytic oxidation (PEO) process. J. Phys. D. Appl. Phys., 43 (2010), pp. 105-203.

[15] A. Günterschultze, H. Betz, Electrolytkondensatoren, Krayn, Berlin H. Cram, (1937).

[16] W. McNiell, G. Nordbloom, US Patent 2 854 390, September 30, 1958.

[17] W. McNiell, L. Gruss, Anodic spark reaction processes and articles, US Patent 3 293 158, 1966

[18] G. Markov, G.V. Markova, USSR Patent 526 961, Bul. Inv. 32 (1976).

[19] K. Dittrich, W. Krysmann, P. Kurze, H.G. Schneider, Structure and properties of ANOF Layers, Cryst. Res. Technol., 19 (1984), pp. 93-99

[20] W. Krysmann, P. Kurze, K.H. Dittrich, H.G. Schneider, Process characteristics and parameters of Anodic Oxidation by spark discharge (ANOF), Cryst. Res. Technol., 19 (1984), pp. 973-979

[21] V. A. Fyedorov, A. G. Kan, R. P. Maksutov, Surface Strengthening of Oil & Gas Trade Facilities by Micro Arc Oxidation, VNIIOENG, Moscow (1989) in Russian
[22] G.A. Markov, B.S. Gizatullin, I.B. Rychazhkova, USSR Patent 926 083, Bul. Inv. 17, 1982.
[23] R. Gradkovsky, S. Bayles, US Patent 3 956 080, 1974.
[24] S. Brown, K. Kuna, T.Van, Anodic Spark Deposition from Aqueous Solutions of NaAlO2 and Na2SiO3, J. Am. Ceram. Soc., 54 (1971) pp. 384-390.
[25] W. Xue, Z. Deng, Y. Lai, R. Chen, Analysis of phase distribution for ceramic coatings formed by microarc oxidation on aluminum alloy, J. Am. Ceram. Soc., 81 (1998) pp. 1365-1368.
[26] G. Wirtz, S. Brown, W. Kriven, Ceramic Coatings by Anodic Spark Deposition, Mater. Manuf. Process.,6 (1991) pp. 87-115.
[27] A. L. Yerokhin, X. Nie, A. Leyland, A. Matthews, S. J. Dowey, Plasma electrolysis for surface engineering. Surf. Coat. Technol., 122 (1999), pp. 73-93.
[28] F. C. Walsh, C. T. J. Low, R. J. K. Wood, K. T. Stevens, J. Archer, A. R., Poeton, et al. Plasma electrolytic oxidation (PEO) for production of anodised coatings on lightweight metal (Al, Mg, Ti) alloys. Trans. IMF, 87 (2009), pp. 122-135.
[29] P. Gupta, G. Tenhundfeld, E. Daigle, D. Ryabkov, Electrolytic plasma technology: science and engineering—an overview. Surf. Coat. Technol., 201 (2007), pp. 8746-8760.
[30] R. Arrabal, E. Matykina, T. Hashimoto, P. Skeldon, G. E. Thompson, Characterization of AC PEO coatings on magnesium alloys. Surf. Coat. Technol., 203 (2009), pp. 2207-2220.
[31] M. Mohedano, C. Blawert, M. Zheludkevich, Silicate-based Plasma Electrolytic Oxidation (PEO) coatings with incorporated CeO_2 particles on AM50 magnesium alloy. Mater. Design, 86 (2015), pp. 735-744.
[32] G. Lv, H. Chen, X. Wang, H. Pang, G. Zhang, B. Zou, et al., Effect of additives on structure and corrosion resistance of plasma electrolytic oxidation coatings on AZ91D magnesium alloy in phosphate based electrolyte. Surf. Coat. Technol., 205 (2010), pp. S36-S40.
[33] V. Bakovets, O. Polyakov, I. Dolgovesova. Plasma electrolytic anode treatment of metals. Nauka, Novosibirsk, 168 (1991).
[34] S. K. Sengupta, O. P. Singh, Contact glow discharge electrolysis: a study of its chemical yields in aqueous inert-type electrolytes. J. Electroanal. Chem., 369 (1994), pp. 113-120.
[35] G. B. Darband, M. Aliofkhazraei, P. Hamghalam, N. Valizade, Plasma electrolytic oxidation of magnesium and its alloys: Mechanism, properties and applications. J. Magnes. Alloys, 5 (2017), pp. 74-132.
[36] V. Dehnavi, B. Luan, X. Liu, D. Shoesmith, S. Rohani, Correlation between plasma electrolytic oxidation treatment stages and coating microstructure on aluminum under unipolar pulsed DC mode. Surf. Coat. Technol., 269 (2015), pp. 91-99.
[37] F. Jaspard-Mecuson, T. Czerwiec, G. Henrion, T. Belmonte, L. Dujardin, A. Viola, Tailored aluminium oxide layers by bipolar current adjustment in the Plasma Electrolytic Oxidation (PEO) process. Surf. Coat. Technol., 201 (2007), pp. 8677-8682.
[38] Y. Cheng, M. Mao, J. Cao, Z. Peng, Plasma electrolytic oxidation of an Al-Cu-Li alloy in alkaline aluminate electrolytes: A competition between growth and dissolution for the initial ultra-thin films. Electrochim. Acta, 138 (2014), pp. 417-429.
[39] V. Dehnavi, B. Luan, D. Shoesmith, X. Liu, S. Rohani, Effect of duty cycle and applied current frequency on plasma electrolytic oxidation (PEO) coating growth behavior. Surf. Coat. Technol., 226 (2013), pp. 100–107.

[40] M. Boinet, S. Verdier, S. Maximovitch, F. Dalard, Plasma electrolytic oxidation of AM60 magnesium alloy: Monitoring by acoustic emission technique. Electrochemical properties of coatings. Surf. Coat. Technol., 199 (2005), pp. 141-149.
[41] J. Garbarz-Olivier, C. Guilpin, The origin of the electrode effect in various electrolytes, J. Electroanal. Chem., 91 (1978), pp. 79-91.
[42] M. Boinet, S. Verdier, S. Maximovitch, F. Dalard, Plasma electrolytic oxidation of AM60 magnesium alloy: Monitoring by acoustic emission technique. Electrochemical properties of coatings, Surf. Coat. Tech, 199 (2005), pp. 141-149.
[43] C. S. Dunleavy, J. A. Curran, T. W. Clyne, Self-similar scaling of discharge events through PEO coatings on aluminium. Surf. Coat. Technol., 206 (2011), pp. 1051-1061.
[44] R. O. Hussein, X. Nie, D. O. Northwood, An investigation of ceramic coating growth mechanisms in plasma electrolytic oxidation (PEO) processing. Electrochim. Acta, 112 (2013), pp. 111-119.
[45] R. O. Hussein, D. O. Northwood, X. Nie, Processing-microstructure relationships in the plasma electrolytic oxidation (PEO) coating of a magnesium alloy. Mater. Sci. Appl., 5 (2014), pp. 124-139.
[46] R. O. Hussein, Plasma Process Control for Improved PEO Coatings on Magnesium Alloys. (2015).
[47] X. Lu, S. P. Sah, N. Scharnagl, M. Störmer, M. Starykevich, M. Mohedano, et al. Degradation behavior of PEO coating on AM50 magnesium alloy produced from electrolytes with clay particle addition. Surf. Coat. Technol., 269 (2015). pp. 155-169.
[48] D. Quintero, O. Galvis, J. A. Calderón, J. G. Castaño, F. Echeverría, Effect of electrochemical parameters on the formation of anodic films on commercially pure titanium by plasma electrolytic oxidation. Surf. Coat. Technol., 258, (2014), pp. 1223-1231.
[49] L. Chang, Growth regularity of ceramic coating on magnesium alloy by plasma electrolytic oxidation. J. Alloys. Compd., 468 (2009), pp. 462-465.
[50] P. Wang, Research Description of MAO treatment on Al/Mg alloys, Special Casting and Nonferrous alloys, (2003), pp. 23-26.
[51] X. Ma, S. Zhu, L. Wang, C. Ji, C. Ren, S. Guan, Synthesis and properties of a bio-composite coating formed on magnesium alloy by one-step method of micro-arc oxidation. J. Alloys. Compd., 590 (2014) , pp. 247-253.
[52] H. F. Guo, M.Z. An, Growth of ceramic coatings on AZ91D magnesium alloys by micro-arc oxidation in aluminate–fluoride solutions and evaluation of corrosion resistance. Appl. Surf. Sci. 246 (2005) pp. 229–238.
[53] X. P. Zhang, G. Chen, Corrosion protection of AZ91D Mg alloy coating with micro-arc oxidation film evaluated by immersion and electrochemical tests. Surf. Rev. Lett. 12 (2005) 279–287.
[54] G. H. Lv, H. Chen, X.Q. Wang, H. Pang, G.L. Zhang, B. Zou, et al., Surf. Coat. Tech. 205 (2010) S36–S40.
[55] F. H. Cao, L.Y. Lin, Z. Zhang, J.Q. Zhang, C.N. Cao, Trans. Nonferrous Met. Soc. China 18 (2008) 240–247.
[56] H. Hornberger, S. Virtanen, A. R. Boccaccini, Biomedical coatings on magnesium alloys–a review. Acta Biomater., 8 (2012), pp. 2442-2455.
[57] J. A. Curran, T. W. Clyne, The thermal conductivity of plasma electrolytic oxide coatings on aluminium and magnesium. Surf. Coat. Technol., 199 (2005), pp. 177-183.
[58] X. Zhang, Z. Zhao, F. Wu, Y. Wang, J. Wu, Corrosion and wear resistance of AZ91D magnesium alloy with and without microarc oxidation coating in Hank's solution. J. Mater. Sci., 42 (2007) 8523–8528.

[59] G. B. Darband, M. Aliofkhazraei, P. Hamghalam, N. Valizade, Plasma electrolytic oxidation of magnesium and its alloys: Mechanism, properties and applications. J. Magnes. Alloys, 5 (2017), pp.74-132.
[60] H. N. Vatan, R. Ebrahimi-kahrizsangi, M. Kasiri-asgarani, Structural, tribological and electrochemical behavior of SiC nanocomposite oxide coatings fabricated by plasma electrolytic oxidation (PEO) on AZ31 magnesium alloy. J. Alloys. Compd., 683 (2016), pp. 241-255.
[61] A. H. Musfirah, A. G. Jaharah, Magnesium and aluminum alloys in automotive industry. J. Appl. Sci. Res., 8 (2012), pp. 4865-4875.
[62] C. Ma, A. Nagai, Y. Yamazaki, T. Toyama, Y. Tsutsumi, T. Hanawa, W. Wang, K. Yamashita, Acta Biomater., 8 (2012), pp. 860-865.
[63] Blawert, W. Dietzel, E. Ghali , G. Song, Anodizing treatments for magnesium alloys and their effect on corrosion resistance in various environments. Adv. Eng. Mater., 8 (2006), pp. 511-533.
[64] X. N. Gu, N. Li, W. R. Zhou, Y. F. Zheng, X. Zhao, Q. Z. Cai, L. Ruan, Corrosion resistance and surface biocompatibility of a microarc oxidation coating on a Mg–Ca alloy. Acta Biomater., 7 (2011), pp. 1880-1889.
[65] Y. Wang, H. Yu, C. Chen, Z. Zhao, Review of the biocompatibility of micro-arc oxidation coated titanium alloys. Mater. Des., 85 (2015), pp. 640-652.
[66] F. Witte, Reprint of: The history of biodegradable magnesium implants: A review. Acta Biomater., 23 (2015), pp. S28-S40.
[67] G. Wu, J. M. Ibrahim, P. K. Chu, Surface design of biodegradable magnesium alloys—a review. Surf. Coat. Technol., 233(2013), pp. 2-12.
[68] M. Z. Ibrahim, A. A. Sarhan, F. Yusuf, M. Hamdi, Biomedical materials and techniques to improve the tribological, mechanical and biomedical properties of orthopedic implants–A review article. J. Alloys Comp., 714 (2017), pp. 636-667.
[69] X. Yu, L. Chen, Y. He, Z. Yan, In-situ fabrication of catalytic metal oxide films in microchannel by plasma electrolytic oxidation. Surf. Coat. Technol., 269 (2015). pp. 30-35.
[70] S.F. Tikhov, G.V. Chernykh, V.A. Sadykov, A.N. Salanov, G.M. Alikina, S.V. Tsybulya, V.F. Lysov, Catal. Today 53 (1999) 639–646.
[71] V.S. Rudnev, L.M. Tyrina, I.V. Lukiyanchuk, T.P. Yarovaya, I.V. Malyshev, A.Y. Ustinov, P.M. Nedozorov, T.A. Kaidalova, Surf. Coat. Technol. 206 (2011) 417–424.
[72] I. V. Lukiyanchuk, V. S. Rudnev, L. M. Tyrina, Plasma electrolytic oxide layers as promising systems for catalysis. Surf. Coat. Technol., 307, (2016), pp. 1183-1193.
[73] E. V. Parfenov, A. Yerokhin, R. R. Nevyantseva, M. V. Gorbatkov, C. J. Liang, A. Matthews, Towards smart electrolytic plasma technologies: An overview of methodological approaches to process modelling. Surf. Coat. Technol., 269 (2015), pp. 2-22.
[74] Y. Cheng, Z. Peng, X. Wu, J. Cao, P. Skeldon, G. E. Thompson, A comparison of plasma electrolytic oxidation of Ti-6Al-4V and Zircaloy-2 alloys in a silicate-hexameta phosphate electrolyte. Electrochim. Acta, 165 (2015), pp. 301-313.
[75] V. V. Bakovets, O. V. Polyakov, I. P. Dolgovesova. Plasma electrolytic anode treatment of metals. Nauka, Novosibirsk, 168 (1991).
[76] A.G. Rakoch, V.V. Khokhlov, V.A. Bautin, N.A. Lebedeva, Y.V. Magurova, I.V. Bardin, Model Concepts on the Mechanism of Microarc Oxidation of Metal Materials and the Control over This Process. Prot. Met., 42 (2006) pp. 158–169.
[77] A. I. Mamaev, Y.Y. Chekanova, Z.M. Ramazanova, Parameters of Pulsating Microplasma Processes on Aluminum and Its Alloys. Prot. Met., 36 (2000) pp. 605–608.

[78] E. V. Parfenov, A.L. Yerokhin, A. Matthews, Frequency response studies for the plasma electrolytic oxidation process. Surf. Coat. Technol. 201 (2007) pp. 8661–8670.
[79] A. L. Erokhin, V.V. Lubimov, R.V. Ashitkov, Fiz. Khim. Obrab. Model of oxide coatings formation during plasma-electrolytic oxidizing of aluminum in silicate solutions. Mater. (1996) 39–44.
[80] S. V. Gnedenkov, S. L. Sinebryukhov, V. I. Sergienko, Electrochemical impedance simulation of a metal oxide heterostructure/electrolyte interface: A review. Russ. J. Electrochem., 42 (2006), pp. 197-211.
[81] P. S. Gordienko, E. S. Panin, A. V. Dostovalov, V. K. Usol'tsev, Voltammetric Characteristics of the Metal–Oxide–Electrolyte System at Electrode Polarization with Pulse Voltage. Prot. Met. Phys. Chem. Surf. 45 (2009), pp. 487–493.
[82] S. Ikonopisov, Theory of electrical breakdown during formation of barrier anodic films. Electrochim. Acta, 22 (1977), pp. 1077-1082.
[83] J. M. Albella, I. Montero, J. M. Martínez-Duart, Electron injection and avalanche during the anodic oxidation of tantalum. J. Electrochem. Soc., 131 (1984), pp. 1101-1104.
[84] A. I. Mamaev, V. A. Mamaeva, E. Y. Beletskaya, A. K. Chubenko, T. A. Konstantinova, A Theory of a Collective Microplasma Process for Formation of Nanostructural Inorganic Nonmetallic Coatings through Localization of High-Energy Flows in the Nanolayers of the Metalelectrolyte Interface. Mathematical Modeling. Part 1. Russ. Phys. J., 56 (2013), pp. 959-969.
[85] J. P. Caire, F. Dalard, W. S. Minko, Modeling the plasma electrolytic oxidation of aluminium and magnesium alloys. ECS Trans., 2(2007), pp. 1-21.
[86] L. R. Krishna, G. Sundararajan, Aqueous corrosion behavior of micro arc oxidation (MAO)-coated magnesium alloys: a critical review. JOM, 66 (2014), pp. 1045-1060.
[87] J. M. Albella, I. Montero, J. M. Martínez-Duart, Electron injection and avalanche during the anodic oxidation of tantalum. J. Electrochem. Soc., 131 (1984). 1101-1104.
[88] Z. Qiu, R. Wang, Y. Zhang, Y. Qu, X. Wu, Study of Coating Growth Behavior During the Plasma Electrolytic Oxidation of Magnesium Alloy ZK60. J. Mater. Eng. Perform., 24 (2015), pp. 1483-1491.
[89] S. Ikonopisov, Theory of electrical breakdown during formation of barrier anodic films. Electrochim. Acta, 22 (1977), pp. 1077-1082.
[90] V. V. Bakovets, O. V. Polyakov, I. P. Dolgovesova. Plasma electrolytic anode treatment of metals. Nauka, Novosibirsk, 168 (1991).
[91] L. R. Krishna, K. R. C. Somaraju, G. Sundararajan, The tribological performance of ultra-hard ceramic composite coatings obtained through microarc oxidation. Surf. Coat. Technol., 163 (2003), pp. 484-490.
[92] D. L. Wilson, Use of modeling and simulation to support airport security. A & E Syst. Mag., IEEE, 20 (2005), pp. 3-6.
[93] Lawrence, Mike, and Yunhong Jiang. "Porosity, pore size distribution, micro-structure." *Bio-aggregates Based Building Materials*. Springer, Dordrecht, 2017. pp. 39-71.
[94] Li, Q., Ito, K., Wu, Z., Lowry, C. S., Loheide, I. I., & Steven, P. (2009). COMSOL Multiphysics: A novel approach to ground water modeling. *Groundwater*, *47*(4), 480-487.
[95] W. B. Zimmerman, Multiphysics Modelling with Finite Element Methods, World Scientific Publishing Co Inc. 18 (2006).
[96] D. L. Logan, A first course in the finite element method, Cengage Learning, (2011).

[97] S. I. Pyun, M. H. Hong, A model describing the growth kinetics of passivating oxide film prepared under potentiostatic conditions. Electrochim. Acta, 37 (1992), pp. 327-332.
[98] Y. Mori, A. Koshi, J. Liao, H. Asoh, S. Ono, Characteristics and corrosion resistance of plasma electrolytic oxidation coatings on AZ31B Mg alloy formed in phosphate–silicate mixture electrolytes. Corros. Sci., 88 (2014), pp. 254-262.
[99] X. Lu, C. Blawert, M. L. Zheludkevich, K. U. Kainer, Insights into plasma electrolytic oxidation treatment with particle addition. Corros. Sci., 101 (2015), pp. 201-207.
[100] H. Duan, C. Yan, F. Wang, Effect of electrolyte additives on performance of plasma electrolytic oxidation films formed on magnesium alloy AZ91D. Electrochim. Acta, 52 (2007), pp. 3785-3793.
[101] R. O. Hussein, P. Zhang, X. Nie, Y. Xia, D. O. Northwood, The effect of current mode and discharge type on the corrosion resistance of plasma electrolytic oxidation (PEO) coated magnesium alloy AJ62. Surf. Coat. Technol., 206 (2011), 1990-1997.
[102] A. Kielbus, T. Rzychon, R. Cibis, Microstructure of AM50 die casting magnesium alloy. J. Achiev. Mater. Manuf. Eng., 18 (2006), pp. 135-138.
[103] X. Lu, C. Blawert, Y. Huang, H. Ovri, M. L. Zheludkevich, K. U. Kainer, Plasma electrolytic oxidation coatings on Mg alloy with addition of SiO2 particles. Electrochim. Acta, 187 (2016), pp. 20-33.
[104] H. Duan, C. Yan, F. Wang, Growth process of plasma electrolytic oxidation films formed on magnesium alloy AZ91D in silicate solution. Electrochim. Acta, 52 (2007), pp. 5002-5009.
[105] A. L. Yerokhin, V. V. Lyubimov, R. V. Ashitkov, Phase formation in ceramic coatings during plasma electrolytic oxidation of aluminium alloys. Ceram. Int., 24 (1998), pp. 1-6.
[106] E. V. Parfenov, R. G. Farrakhov, V. R. Mukaeva, A. V. Gusarov, R. R. Nevyantseva, A. Yerokhin, Electric field effect on surface layer removal during electrolytic plasma polishing. Surf. Coat. Technol., 307 (2016) pp. 1329-1340.
[107] R. O. Hussein, X. Nie, D. O. Northwood, A. Yerokhin, A. Matthews, Spectroscopic study of electrolytic plasma and discharging behaviour during the plasma electrolytic oxidation (PEO) process. J. Phys. D: Appl. Phys., 43 (2010), pp. 105203.
[108] C. S. Dunleavy, J. A. Curran, T. W. Clyne, Self-similar scaling of discharge events through PEO coatings on aluminium. Surf. Coat. Technol., 206 (2011), pp. 1051-1061.
[109] D. Höche, Simulation of Corrosion Product Deposit Layer Growth on Bare Magnesium Galvanically Coupled to Aluminum. J. Electrochem. Soc., 162 (2015), pp. 1-11.
[110] M. D. Krom, R. A. Berner, The diffusion coefficients of sulfate, ammonium, and phosphate ions in anoxic marine sediments. Limnol. Oceanogr., 25 (1980), pp. 327-337.
[111] A. M. Friedman, J. W. Kennedy, The Self-diffusion Coefficients of Potassium, Cesium, Iodide and Chloride Ions in Aqueous Solutions1. J. Am. Chem. Soc., 77 (1955), pp. 4499-4501.
[112] L. O. Snizhko, A. L. Yerokhin, A. Pilkington, N. L. Gurevina, D. O. Misnyankin, A. Leyland, A. Matthews, Anodic processes in plasma electrolytic oxidation of aluminium in alkaline solutions. Electrochim. Acta, 49 (2004), pp. 2085-2095.
[113] L. O. Snizhko, A. L. Yerokhin, N. L. Gurevina, V. A. Patalakha, A. Matthews, Excessive oxygen evolution during plasma electrolytic oxidation of aluminium. Thin Solid Films, 516 (2007), pp. 460-464.
[114] Y. Ma, H. Hu, D. Northwood, X. Nie, Optimization of the electrolytic plasma oxidation processes for corrosion protection of magnesium alloy AM50 using the Taguchi method. J. Mater. Process. Tech., 182 (2007), pp. 58-64.

[115] G. Lv, H. Chen, W. Gu, L. Li, E. Niu, X. Zhang, et al., Effects of current frequency on the structural characteristics and corrosion property of ceramic coatings formed on magnesium alloy by PEO technology. J. Mater. Process. Technol., 208 (2008), pp. 9-13.
[116] P. Su, X. Wu, Y. Guo, Z. Jiang, Effects of cathode current density on structure and corrosion resistance of plasma electrolytic oxidation coatings formed on ZK60 Mg alloy. J. Alloys. Compd., 475 (2009), pp. 773-777.
[117] Sreekanth, D., N. Rameshbabu, and K. Venkateswarlu. Effect of various additives on morphology and corrosion behavior of ceramic coatings developed on AZ31 magnesium alloy by plasma electrolytic oxidation. Ceram. Int., 38 (2012), pp. 4607-4615.
[118] Y. Wang, K. Wu, M. Zheng, Effects of reinforcement phases in magnesium matrix composites on microarc discharge behavior and characteristics of microarc oxidation coatings. Surf. Coat. Technol., 201 (2006), pp. 353-360.
[119] J. Liu, W. Zhang, H. Zhang, X. Hu, J. Zhang, Effect of microarc oxidation time on electrochemical behaviors of coated bio-compatible magnesium alloy. Mater. N.A. Proc., 1 (2014), pp.70-81.
[120] G. Lv, H. Chen, X. Wang, H. Pang, G. Zhang, B. Zou, et al., Effect of additives on structure and corrosion resistance of plasma electrolytic oxidation coatings on AZ91D magnesium alloy in phosphate based electrolyte. Surf. Coat. Technol., 205 (2010), pp. S36-S40.
[121] M. V. Sidorova, S.L. Sinebrukhov, O. A. Khrisanfova, S. V. Gnedenkov, Effect of PEO-modes on the electrochemical and mechanical properties of coatings on MA8 magnesium alloy. Phys. Proced., 23 (2012), pp. 90-93.
[122] V. Dehnavi, B. L. Luan, D.W. Shoesmith, X. Liu, S. Rohani, Effect of duty cycle and applied current frequency on plasma electrolytic oxidation (PEO) coating growth behavior. Surf. Coat. Technol., 226 (2013), pp. 100-107.
[123] P. B. Srinivasan, J. Liang, C. Blawert, M. Störmer, W. Dietzel, Effect of current density on the microstructure and corrosion behaviour of plasma electrolytic oxidation treated AM50 magnesium alloy. Appl. Surf. Sci., 255 (2009), pp. 4212-4218.
[124] R. O. Hussein, P. Zhang, X. Nie, Y. Xia, D.O. Northwood, The effect of current mode and discharge type on the corrosion resistance of plasma electrolytic oxidation (PEO) coated magnesium alloy AJ62. Surf. Coat. Technol., 206 (2011), pp. 1990-1997.
[125] A. Melhem, G. Henrion, T. Czerwiec, J.L. Briançon, T. Duchanoy, F. Brochard, et al., Changes induced by process parameters in oxide layers grown by the PEO process on Al alloys. Surf. Coat. Technol., 205 (2011), pp. 133-136.
[126] C. B. Wei, X.B. Tian, S.Q. Yang, X.B. Wang, Ricky K.Y. Fu, Paul K. Chu, Anode current effects in plasma electrolytic oxidation. Surf. Coat. Technol., 201 (2007), pp. 5021-5024.
[127] V. Dehnavi, X. Liu, B. L. Luan, D.W. Shoesmith, S. Rohani, Phase transformation in plasma electrolytic oxidation coatings on 6061 aluminum alloy. Surf. Coat. Technol., 251 (2014), pp. 106-114.
[128] Y. Cheng, F. Wu, E. Matykina, P. Skeldon, G.E. Thompson, The influences of microdischarge types and silicate on the morphologies and phase compositions of plasma electrolytic oxidation coatings on Zircaloy-2. Corros. Sci. 59 (2012), pp. 307-315.
[129] A. G. Rakoch, A. A. Gladkova, Z. Linn, D.M. Strekalina, The evidence of cathodic micro-discharges during plasma electrolytic oxidation of light metallic alloys and micro-discharge intensity depending on pH of the electrolyte. Surf. Coat. Technol., 269 (2015), pp. 138-144.

[130] C. Blawert, S.P. Sah, J. Liang, Y. Huang, D. Höche, Role of sintering and clay particle additions on coating formation during PEO processing of AM50 magnesium alloy. Surf. Coat. Technol., 213 (2012), pp. 48-58.
[131] H. L. de Maubeuge, Influence of geometric variables on the current distribution uniformity at the edge of parallel plate electrodes. Electrochim. Acta, 56 (2011), pp. 10603-10611.
[132] G. Sundararajan, L. Rama Krishna, Mechanisms underlying the formation of thick alumina coatings through the MAO coating technology. Surf. Coat. Technol., 167 (2003), pp. 269-277.
[133] R. Arrabal, E. Matykina, T. Hashimoto, P. Skeldon, G.E. Thompson, Characterization of AC PEO coatings on magnesium alloys. Surf. Coat. Technol., 203 (2009), pp. 2207-2220.
[134] X. Ma, C. Blawert, D. Höche, M. L. Zheludkevich, K. U. Kainer, Investigation of electrode distance impact on PEO coating formation assisted by simulation. Appl. Surf. Sci., 388 (2016), pp. 304-312.
[135] X. Lu, C. Blawert, K. U. Kainer, M. L. Zheludkevich, Investigation of the formation mechanisms of plasma electrolytic oxidation coatings on Mg alloy AM50 using particles. Electrochim. Acta, 196 (2016), pp. 680-691.
[136] T. Mi, B. Jiang, Z. Liu, L. Fan, Plasma formation mechanism of microarc oxidation, Electrochim. Acta, 123 (2014), pp. 369–377.
[137] J. Garbarz-Olivier, C. Guilpin, The origin of the electrode effect in various electrolytes, J. Electroanal. Chem., 91 (1978), pp. 79-91.
[138] R. Hussein, X. Nie, D. Northwood, *Production of high quality coatings on light alloys using Plasma Electrolytic Oxidation (PEO)*. High Performance and Optimum Design of Structures and Materials II, 166 (2016) 439.
[139] C. Liu, D. He, Q. Yan, Z. Huang, P. Liu, D. Li, D. Shen, *An investigation of the coating/substrate interface of plasma electrolytic oxidation coated aluminum*. Surf. Coat. Technol., 280 (2015), pp. 86-91.
[140] Hussein, R. O., Nie, X., & Northwood, D. O. *Plasma Process Control for Improved PEO Coatings on Magnesium Alloys*, (2015) 172.
[141] A. Nomine, S. C. Troughton, A. V. Nomine, G. Henrion, T. W. Clyne, High speed video evidence for localised discharge cascades during plasma electrolytic oxidation. Surf. Coat. Technol., 269 (2015) pp. 125-130.
[142] S. C. Troughton, A. Nominé, J. Dean, T. W. Clyne, Effect of individual discharge cascades on the microstructure of plasma electrolytic oxidation coatings. Appl. Surf. Sci., 389 (2016), pp. 260-269.
[143] Troughton, S. C., Nomine, A., Nomine, A. V., Henrion, G., & Clyne, T. W. (2015). Synchronised electrical monitoring and high speed video of bubble growth associated with individual discharges during plasma electrolytic oxidation. *Applied Surface Science, 359*, 405-411.

Appendix

1. List of symbols and abbreviations

2D	Two dimensional
3D	Three dimensional
AC	Alternating current
Al	Aluminum
AM50	Mg-5Al-0.4Mn (wt.%)
C_o	Initial concentrations
c_i	Concentration
DC	Direct current
D_i	Diffusion coefficient
E_a	Equilibrium potential
E_l	Potential drop over electrolyte
E_{ff}	Efficiency of coating formation
EDS	Energy dispersive X-rays spectroscopy
EIS	Electrochemical impedance spectroscopy
F	Faraday constant
I	The identity matrix
I	Current
I_c	Current contributing to coating formation
I_e	Current generating gases
j	Current density
j_e	Current density contributing to gas formation
j_p	Current density in a discharge channel
j_c	Current density contributing to coating formation
$K_{sp(MgOH)}$	Solubility products of $Mg(OH)_2$
$K_{sp(MgP)}$	Solubility products of $Mg_3(PO_4)_2$
L	Coating thickness
L_0	Initial thickness
MAO	Microarc oxidation
Mg	Magnesium
M_{MgO}	Molar mass of MgO

M_{MgOH}	Molar mass of $Mg(OH)_2$
M_{MgP}	Molar mass of $Mg_3(PO_4)_2$
n_m	Number of electrons
OCP	Open circuit potential
OES	Optical emission spectroscopy
P	Pore coverage ratio
p	Pressure in the holes
PEO	Plasma electrolytic oxidation
Q_{MgP}	Ion products of $Mg_3(PO_4)_2$
Q_{MgOH}	Ion products of $Mg(OH)_2$
Rc	Resistance corresponding to I_c
Rel	Resistance of electrolyte
Rp	Resistance corresponding to I_p
R_{MgO}	Reaction rate of MgO
R_i	Chemical reaction rate
R_{MgP}	Reaction rate of $Mg_3(PO_4)_2$
R_{gas}	Universal gas constant
S	Surface area
S_c	Surface area of defect free coating
S_p	Surface area covered by discharge channels
t	Time
T	Temperature
Ti	Titanium
u	Fluid flow vector
U	Applied voltage
v_i	Stoichiometric coefficient
v_{MgO}	Growth rate of MgO
v_{MgOH}	Growth rate of $Mg(OH)_2$
v_{MgP}	Growth rate of $Mg_3(PO_4)_2$
XRD	X-Ray diffraction
σ	Electrolyte conductivity
σ_{eff}	Effective conductivity
z_i	Charge number

φ_i	Electric potential
μ_i	Diffusivity
η	Viscosity
ρ	Density of electrolyte
ρ_{MgOH}	Density of $Mg(OH)_2$
$\rho_{Mg3(PO4)2}$	Density of $Mg_3(PO_4)_2$
ρ_{MgO}	Density of MgO

2. Publications during candidature

Peer-reviewed papers:

1. X. Ma, C. Blawert, D. Höche, K. U. Kainer, M. L. Zheludkevich, A model describing the growth of a PEO coating on AM50 Mg alloy under constant voltage mode. *Electrochimica Acta,* 251 (2017): 461-474.
2. X. Ma, C. Blawert, D. Höche, K. U. Kainer, M. L. Zheludkevich, Investigation of electrode distance impact on PEO coating formation assisted by simulation. Investigation of electrode distance impact on PEO coating formation assisted by simulation." *Applied Surface Science* 388 (2016): 304-312.
3. Y. Feng, X. Ma, L. Chang, S. Zhu, S. Guan, Characterization and cytocompatibility of polydopamine on MAO-HA coating supported on Mg-Zn-Ca alloy. *Surface and Interface Analysis*, 49 (2017): 1115-1123.
4. X. Ma, C. Blawert, D. Höche, K. U. Kainer, M. L. Zheludkevich, Simulation assisted investigation of substrate geometry impact on PEO coating formation, submitted for publication.

3. Publications included in this thesis

1. X. Ma, C. Blawert, D. Höche, K. U. Kainer, M. L. Zheludkevich, A model describing the growth of a PEO coating on AM50 Mg alloy under constant voltage mode. *Electrochimica Acta,* 251 (2017): 461-474. – incorporated in Chapter 5.

X. Ma conceived and designed the study in discussion with C. Blawet and D. Höche. X. Ma carried out the experimental work and modelling and simulation. C. Blawet, D. Höche, M. L. Zheludkevich and K. U. Kainer gave constructive comments on data analysis. All the authors contributed to the interpretation of the results and to writing of the paper.

2. X. Ma, C. Blawert, D. Höche, K. U. Kainer, M. L. Zheludkevich, Investigation of electrode distance impact on PEO coating formation assisted by simulation. Investigation of electrode distance impact on PEO coating formation assisted by simulation." *Applied Surface Science* 388 (2016): 304-312. - incorporated in Chapter 6.

X. Ma conceived and designed the study in discussion with C. Blawet and D. Höche. X. Ma carried out the experimental work and modelling and simulation. C. Blawet, D. Höche, M. L. Zheludkevich and K. U. Kainer gave constructive comments on data analysis. All the authors contributed to the interpretation of the results and to writing of the paper.

3. X. Ma, C. Blawert, D. Höche, K. U. Kainer, M. L. Zheludkevich, Simulation assisted investigation of substrate geometry impact on PEO coating formation, submitted for publication. - incorporated in Chapter 7.

X. Ma conceived and designed the study in discussion with C. Blawet and D. Höche. X. Ma carried out the experimental work and modelling and simulation. C. Blawet, D. Höche, M. L. Zheludkevich and K. U. Kainer gave constructive comments on data analysis. All the authors contributed to the interpretation of the results and to writing of the paper.

4. Acknowledgement

It is my pleasure to express my sincere appreciation here to those who have contributed either way in this thesis during my PhD study. First and foremost, I would like to express my sincerest gratitude to my supervisors Prof. Dr. Mikhail Zheludkevich and Prof. Dr. Karl Ulrich Kainer who have given me the opportunity to study at MagIC center in Helmholtz Zentrum Geesthacht and the chances to participate in international conferences to exchange with peer scientists. It is their support, guidance and encouragement led me to accomplish my work. I would also like to thank Prof. Dr. rer. nat. Marcus Stiemer, Chair for Theoretical Electrical Engineering and Numeric Field Calculation within the Faculty of Electrical Engineering at Helmut-Schmidt-Universität, for being my second academic supervisor and for his valuable suggestions to improve the dissertation.

I would like to thank deeply to my daily supervisors Dr. Carsten Blawert and Dr. Daniel Höche who are responsible for the experiments and modeling respectively. Their foresight led me into this field and their knowledge taught me how to deal with research in a more scientific way. The responsibility, insistence and optimism I learned from them help me overcome many difficulties in academic or daily life. Thanks for their guidance and assistance, I could achieve better understanding along the research on PEO characterization and simulation.

I am very grateful to Mr. Ulrich Burmester, Mr. Volker Heitmann and Mr. Gert Wiese for their kind cooperation and professional technical assistance through my PhD studies. I send my sincere thanks to Dr. Xiaopeng Lu, who has been teaching and helping me in academic and daily life since the very first day I came here. He is a vice supervisor to me. My deep gratitude goes to my first roommate Dr. Yufen Zhang for sharing happiness and sorrows and taking care of me when I was sick, and to Dr. Yan Chen for sharing so much wonderful time traveling together. My gratitude also goes to Dr. Natalia Konchakova and Mr. Zahid Mohammad for their help in the discussion of modeling and simulation and all the members of WZK group who supported me throughout these years.

I gratefully acknowledge the funding source from China Scholarship Council (CSC) for the financial support for my PhD study in Germany.

Finally, I would like to express my deepest appreciation to my parents Jingmei Li and Wenhui Ma for raising me up, educating me to be the one who I am and respecting every decision I made. Thank mother for taking care of the family all these years and thank father for taking care of my mother. I always feel so sorry and guilty for being so far away from my family and

failing to do my obligation when my mother needs me. Thank my sisters Jing Ma and Li Ma, my brothers in law and my nieces and nephew for sharing your love and taking good care of my parents when I was away. Thank the whole big family and all my best friends behind me for loving and supporting me to spend all those pleasurable and struggling times. It is my pleasure and obligation to take care of all of you from now on. I especially hope that my mother can overcome the disease and keep me accompanied as long as promised. To my boyfriend, Hailin Tseng: thank you for giving me everything I ever wanted, happiness, freedom, respect, support and unconditional love, and thank you for keeping me accompanied everyday even you are millions of miles away and thank you for helping me in my career and daily life. You are and will always be my soulmate and best friend. Hope we could have a wonderful life together.